9-2013

Techniques to Increase Computational Efficiency in Some Deterministic and Random Electromagnetic Propagation Problems

Selman Ozbayat
University of Massachusetts Amherst, sozbayat@engin.umass.edu

TECHNIQUES TO INCREASE COMPUTATIONAL EFFICIENCY IN SOME DETERMINISTIC AND RANDOM ELECTROMAGNETIC PROPAGATION PROBLEMS

A Dissertation Presented

by

SELMAN ÖZBAYAT

Submitted to the Graduate School of the
University of Massachusetts Amherst in partial fulfillment
of the requirements for the degree of

DOCTOR OF PHILOSOPHY

September 2013

Electrical and Computer Engineering

TECHNIQUES TO INCREASE COMPUTATIONAL EFFICIENCY IN SOME DETERMINISTIC AND RANDOM ELECTROMAGNETIC PROPAGATION PROBLEMS

A Dissertation Presented

by

SELMAN ÖZBAYAT

Approved as to style and content by:

Ramakrishna Janaswamy, Chair

Marinos N. Vouvakis, Member

Eric Polizzi, Member

Sanjay R. Arwade, Member

C.V. Hollot, Department Head
Electrical and Computer Engineering

In the name of Allah – the Most Gracious, the Most Merciful,

to my beloved family.

ACKNOWLEDGEMENTS

I here acknowledge those people who had trust in me and provided me support, advice, insight, questions and answers throughout my study.

First of all, I need to sincerely thank my Advisor, Professor Ramakrishna Janaswamy, for giving me this opportunity. His support, kindliness, technical guidance, his inspiring passion for research has made my entire study a time of rewarding experience. I am very fortunate being under his supervision and in his company.

I also want to thank the other Committee members; Professors Sanjay Arwade, Eric Polizzi and Marinos Vouvakis for their valuable time, helpful comments and suggestions.

I need to acknowledge the faculty and graduate students of the Antennas and Propagation Laboratory. Especially my fellows Caglar Emiroglu and Dr. Richard Martelly from the AP Lab and my roommate Cagatay Capar have devoted their time and effort to help me address technical difficulties while having good time together in Amherst. Dr. Georgios Paraschos and Wei Wang must be remembered for their proficiency and helpfulness in computational matters. I believe that we, the graduate students of the ECE Department, are lucky having Mary McCulloch and Barbara Barnett in the department.

Most importantly, this journey would not have happened without my parents' faith in me, love and caring for me.

ABSTRACT

TECHNIQUES TO INCREASE COMPUTATIONAL EFFICIENCY IN SOME DETERMINISTIC AND RANDOM ELECTROMAGNETIC PROPAGATION PROBLEMS

SEPTEMBER 2013

SELMAN ÖZBAYAT

B.Sc., BILKENT UNIVERSITY

Ph.D., UNIVERSITY OF MASSACHUSETTS AMHERST

Directed by: Professor Ramakrishna Janaswamy

Efficient computation in deterministic and uncertain electromagnetic propagation environments, tackled by parabolic equation methods, is the subject of interest of this dissertation. Our work is comprised of two parts. In the first part we determine efficient absorbing boundary conditions for propagation over deterministic terrain and in the second part we study techniques for efficient quantification of random parameters/outputs in volume and surface based electromagnetic problems.

Domain truncation by transparent boundary conditions for open problems where parabolic equation is utilized to govern wave propagation are in general computationally costly. For the deterministic problem, we utilize two approximations to a convolution-in-space type discrete boundary condition to reduce the cost, while maintaining accuracy in far range solutions. Perfectly matched layer adapted to the

Crank-Nicolson finite difference scheme is also verified for a 2-D model problem, where implemented results and stability analyses for different approaches are compared.

For the random problem, efficient moment calculation of electromagnetic propagation/scattering in various propagation environments is demonstrated, where the dimensionality of the random space varies from $N = 2$ to $N = 100$. Sparse grid collocation methods are used to obtain expected values and distributions, as a non-intrusive sampling method. Due to the low convergence rate in the sparse grid methods for moderate dimensionality and above, two different adaptive strategies are utilized in the sparse grid construction. These strategies are implemented in three different problems. Two problems are concerned with uncertainty in propagation domain intrinsic parameters, whereas the other problem has uncertainty in the boundary shape of the terrain, which is realized as the perfectly conducting (PEC) Earth surface.

TABLE OF CONTENTS

Page

ACKNOWLEDGEMENTS . . . . . **v**

ABSTRACT . . . . . **vi**

LIST OF TABLES . . . . . **x**

LIST OF FIGURES . . . . . **xi**

CHAPTER

1. INTRODUCTION **1**

1.1 Background and Motivation 1
1.2 Original Contributions and Outline 8

2. PARABOLIC EQUATION METHODS **10**

2.1 Introduction 10
2.2 Standard PE in Atmosphere 11
2.3 Split-Step Parabolic Equation (SSPE) Formulation 12
2.4 Crank-Nicolson PE Scheme (FDPE) 14

3. DOMAIN TRUNCATION FOR FDPE **19**

3.1 PML Implementation for FDPE in Free-Space 20
3.2 Discrete Transparent Boundary Condition (DTBC) Derivation 23
3.3 Localized DTBC (LDTBC) Approximation 28
3.4 Approximation by Partial Fractions: LDTBC_2 34
3.5 Numerical Results 38
3.6 CPU Time Comparison 46

4. SPARSE GRID COLLOCATION METHODS **48**

4.1 Construction of the Non-Adaptive Sparse Grid 48
4.2 Adaptive Sparse Grid Collocation Method 58

4.3 $h-$Adaptive Generalized Sparse Grid Method 60
4.4 High Dimensional Model Representations 64

4.4.1 HDMR+ASGC 66

4.5 About Quasi Monte Carlo Methods and Convergence Rates 71

5. PROPAGATION PROBLEMS WITH UNCERTAINTY 73

5.1 First Scattering Example: Reflection from multi-layered slabs 74

5.1.1 About Memory and Time Usages 85
5.1.2 Conclusions about the application 88

5.2 A More Complicated Scattering Problem: Low-Grazing Angle Propagation Over a Random Surface 88

5.2.1 Conclusions about the application 98
5.2.2 About the originally proposed rough surface scattering problem 99

5.3 Application in Tropospheric Propagation: Field Estimation in Long-Range Uncertain Ducting Environments 99

5.3.1 Uncertain Refractivity Profile 100
5.3.2 Numerical Results 103

6. SUMMARY AND CONCLUSIONS 111

APPENDICES

A. ANALYTICAL SOLUTION TO PROPAGATION ABOVE FLAT CONDUCTING SURFACE 114
B. BASIS FUNCTION INTEGRATIONS 118

BIBLIOGRAPHY 127

LIST OF TABLES

Table **Page**

4.1 The errors $\eta_{\mathbf{u}}$, for a sample HDMR+ASGC component elimination performed ($N = 5$), where the data corresponds to Figure 5.17a. 70

5.1 Table of examples considered in Section 5.1. 80

5.2 Memory and time usages in Example 4 of Section 5.1. 87

5.3 Table of examples considered in Section 5.2. 94

5.4 Table of examples considered in Section 5.3. Fixed parameters: $x_t = 50$ meters, $\sigma_t = 2$ meters, frequency= 300 MHz, $x_{max} = 375$ meters. 104

B.1 Combination of node sets, bases and distribution types used in the study. 118

LIST OF FIGURES

Figure **Page**

2.1 Propagation factor (dB) along height, at 80 km, for an antenna located at $t = 0, x_t = 30$ m, operating at 3 GHz. The discretization parameters are $\Delta t = 25$ m, $\Delta x = 0.1$m. 15

2.2 Stencil for FDPE discretization. Through the arithmetic averaging invoked at $m + 1/2$, only the indices in the four corners (disks) of this stencil are used in the resultant discrete equation. 16

3.1 Computation domain, top layer being absorbing boundary and bottom layer PEC 22

3.2 Branch cut on z-plane for $|\nu(z)| = 1$, $R = 0.63$. C_z is the inversion circle around origin. 27

3.3 Exact DTBC convolution stencil. The two layers of nodes correspond to the two convolutions in (3.10). This stencil is valid at all elevations greater than $(J - 1)\Delta x$ 27

3.4 $|\nu(z)|$ for the z values on the $|z| = 0.9$ circle, $R = 0.63$. 29

3.5 Pade coefficient magnitudes of different LDTBC approximations, $R = 0.63$. $\underline{d}$and $\underline{e}$are respective vectors of numerator and denominator coefficients of the corresponding approximation in each case. 29

3.6 Reduced geometry to study the approximation stability 33

3.7 Inverse pole locations $\frac{1}{z_l}$ for reduced-domain LDTBC solutions on z-domain, $l = 0, 1, .., P$. Stars are for the unstable case and inverted triangles are for the stable case. 33

3.8 The poles of LDTBC_2 approximate solution lying inside unit circle in the case of $L = 100$, $V = 0$ and $R = 0.63$ 37

3.9 Field magnitudes normalized by the excitation ($|\psi/A|$) for the first problem set (DTBC, LDTBC and PML). The range is $t = 10,000\lambda$, with $\sigma_t = 1\lambda$, $x_t = x_h/2 = 25\lambda$ and $K = 400$ for the excitation. The dashed DTBC solution curve is indistinguishable from the solid analytical solution curve. 40

3.10 Field magnitudes normalized by the excitation ($|\psi/A|$) for the first problem set (LDTBC_2). Simulation parameters are the same as in Figure 3.9. 40

3.11 L_2-norm errors corresponding to the solutions in Figures 3.9 and 3.10. The dashed curves show LDTBC errors for varying P. Straight solid lines with squares, pentagrams and circles denote error levels for PML and LDTBC_2. 41

3.12 Field magnitudes (V/m) for two different problems. The solid curves are solutions at $t = 20km$ range for a $x_h = 50m$ domain and dashed lines at $t = 50km$ range for $x_h = 100m$. The simulation parameters are $\Delta x = 20cm$, $\Delta t = 5m$, $x_t = 10m$, $\sigma_t = 30cm$, $\delta = 3m$, $L = 150$. 45

3.13 L_2-norm errors ϵ^2. All parameters are the same as in Figure 3.12. 46

3.14 CPU time taken by the boundary computation (convolution in DTBC case). 47

4.1 The basis functions used in the construction of the sparse grid at level $d = 3$, according to Equation (4.5) (top) and Equation (4.14) (bottom): (a) local triangular basis functions, (b) Lagrange characteristic polynomial basis functions. 56

4.2 The hierarchical node subsets from sparse grid level $d = 0$ up to level $d = 3$, $N = 2$ and $\Gamma = [0, 1]^2$, for (a) equi-distant nodes, (b) Chebyshev nodes. 57

4.3 Demonstration of (a) SGC and (b) ASGC through the test example in (4.20). 59

4.4 A sample evolution of index sets of $h-$GSG for an $N = 2-$dimensinal case. The top row depicts sets $\mathcal{O}_i$ (textured grey) and $\mathcal{A}_i$ (solid blue), whereas the bottom row depicts nodes (Chebyshev) entailed with $\mathcal{O}_i$. 63

4.5 Index evolution of the non-adaptive SGC formula in (4.5), from level $d = 0$ to $d = 2$, where $N = 2$. The top row corresponds to indices added to sparse grid at level $|\mathbf{i}|_1 = N + d$, and the bottom row depicts the nodes (equi-distant) present after the corresponding sparse grid level. 63

4.6 Demonstration of domains for sample uni-dimensional (left) and 2−dimensional (left and right) HDMR components. 66

4.7 The contribution of each component function at orders $p \leq p_{max} = 4$, for an $N = 20$ dimensional problem with FDFD solver from Section 5.1. 67

5.1 Normal-incidence reflection from multi-layered media. 76

5.2 Analytical reflection coefficient (red circles), numerical reflection coefficient (solid blue), and total field magnitude (dashed green). Parameters: f=300 MHz, $h_1 = 1.07$ m, $h_2 = 0.765$ m, $h_3 = 0.970$ m, $\epsilon_1 = 5.10$, $\epsilon_2 = 6.37$, $\epsilon_3 = 13.19$, $\mu_1 = 9.31$, $\mu_2 = 13.90$, $\mu_3 = 12.4$, $\sigma_1 = \sigma_2 = \sigma_3 = 5$ mS/m. $|R| = 0.1494$ (analytical). 78

5.3 (a) Error convergence for Example 1 of Section 5.1 for non-adaptive (SGC) and adaptive (ASGC) methods for increasing levels d. (b) $|E[R]|$ estimates corresponding to the curves in (a). 80

5.4 (a) Error convergence for Example 2 of Section 5.1 for MC sampling, ASGC method for increasing levels d, and HDMR+ASGC for increasing component orders p. (b) $\eta_{\mathbf{u}}$ corresponding to the components of the HDMR expansion (HMDR+ASGC curve in (a)). 82

5.5 (a) Error convergence for Example 3 ($N = 20$) of Section 5.1 for MC sampling, and QMC methods based on Sobol and Halton sequences. (b) Same comparison as in (a) made for $h-$GSG and HDMR+ASGC methods. 86

5.6 (a) Error convergence for Example 4 ($N = 100$) of Section 5.1 for MC sampling, and QMC methods based on Sobol and Halton sequences. (b) Same comparison as in (a) made for $h-$GSG and HDMR+ASGC methods. 86

5.7 The computation domain for the scattering problem, denoted with the dashed lines. 91

5.8 Four realizations of random profile g(t), $0 < t < t_{obs} = 420$ m, $B = 7$. 92

5.9 A ray incident on a Gaussian hill at its steepest point. 93

5.10 (a) Error convergence for Example 1 ($N = 3$) of Section 5.2 for MC sampling, $h-$GSG and HDMR+ASGC. (b) Comparison of estimates for PF factor (in dB scale) with HDMR+ASGC and MC. 95

5.11 (a) Error convergence for Example 2 ($N = 9$) of Section 5.2 for MC sampling, $h-$GSG and HDMR+ASGC. (b) QMC results with Sobol and Halton sequences superposed. 95

5.12 (a) Error convergence for Example 3 ($N = 21$) of Section 5.2 for MC sampling, $h-$GSG and HDMR+ASGC. (b) QMC results with Sobol and Halton sequences superposed. 96

5.13 Error convergence for Example 3 ($N = 21$) of Section 5.2 for MC sampling, $h-$GSG and HDMR+ASGC as a function of total elapsed time in seconds. 98

5.14 (a) Refractive index profile according to (5.18), where $N_o = 320$ N-units, $G_N = -0.037$ N-units/m, $dN = -10$ N-units, $h_o = 45$ meters and $dh = 35$ meters. (b) Comparison of different range step sizes in computation of PF at 50 km, for the refractivity profile in (a). 101

5.15 2,000 realizations of the refractivity according to the uncertainties given in Section 5.3.1. 102

5.16 PF_{dB} corresponding to the 2,000 relizations of N in Figure 5.15, (a) at $t_{obs} = 50$ km, (b) at $t_{obs} = 100$ km. 102

5.17 (a) Error convergence for Example 1 of Section 5.3. (b) Expected field estimates for Example 1, $E[PF(50\text{km}, x; y)]$, corresponding to the convergence results in (a). 107

5.18 (a) Error convergence for Example 2 of Section 5.3. (b) Expected field estimates Example 2, $|E[\psi(50\text{km}, x; y)]|$, corresponding to the convergence results in (a). 108

5.19 (a) Error convergence for Example 3 of Section 5.3. (b) Expected PF estimates for Example 3, $|E[PF(100\text{km}, x; y)]|$, corresponding to the convergence results in (a). 108

5.20 (a) Error convergence for Example 4 of Section 5.3 (b) Expected field estimates for Example 4, $|E[\psi(100\text{km}, x; y)]|$, corresponding to the convergence results in (a). 109

5.21 QMC performances superposed on sparse grid performances for (a) Example 3 of Section 5.3, (b) Example 4 of Section 5.3. 109

5.22 Error convergence for MC sampling, $h-$GSG and HDMR+ASGC as a function of total elapsed time in seconds, for (a) Example 3 and (b) Example 4 of Section 5.3. 110

A.1 The propagation environment, where x is the elevation axis and t is the range axis. $s(x)$ is the Gaussian source excited at $t = 0$, the right figure is equivalent of the left figure with PEC removed and an image source added in free-space. 117

B.1 The two integration paths connecting $Z = a$ to $Z = b$ used for integration of Lagrangian bases. "Path 1" discretizes $[a, b]$ on real axis, where "Path 2" discretizes the upper semi-circle in complex plane. 121

B.2 The Cauchy-integral path that is bent for Case 4, for Gaussian weight function not to contain real exponent with positive sign. 126

CHAPTER 1

INTRODUCTION

1.1 Background and Motivation

Thanks to the fast speed-up in microprocessor industry, the last several decades witnessed tackling of increasingly complex computational challenges in electromagnetics (EM). Among others, the vast area of computational electromagnetics is concerned with numerous aspects of the last century's some of the biggest developments including radars, antenna arrays, acoustic communications, buried object or mine detection, mobile communication handsets and radio frequency identification. All of such phenomena that are governed by and devised using the electromagnetic waves occur in the unbounded domain of the universe, and the underlying mathematical problems are always numerically solved with methods that exploit limited memory and time. Therefore, efficient usage of resources are the motivating factors for numerical solvers, and allow newer technology to emerge as the efficiency of solvers increase.

One of the main concerns with wave propagation problems, regarding computational resources, is the truncation of the often-unbounded media by finite boundaries. Having constant limited resources to utilize, the truncated domain dimensions need to be kept decreasing as the operating frequency gets higher, since a fixed finite computation domain and fixed boundaries become electrically larger as the frequency gets higher. In this regard absorbing boundary conditions (ABCs) have been formulated for truncation of domains, that enforce numerical absorption of the waves, and produce near zero boundary reflections into the geometry they are defined for [76]. Later, Berenger introduced the Perfectly Matched Layer (PML) for Maxwell's

equations [10]. This method has been adapted for truncation with various solvers used in computational electromagnetics [59], [24], [16].

For low grazing angle propagation problems where the Parabolic Equation (PE) is used, and for the more general case of the Schrödinger's equation, domain truncation was achieved by placing Transparent Boundary Conditions (TBC) [46], where there are two approaches to implementing the TBCs. A TBC, by definition, produces zero boundary reflections into the geometry it is defined for. Several authors [46], [7] introduced the discretized version of a continuous TBC. Reference [19] showed that this approach cannot assure unconditional stability when the FD discretization does not match the discretization of the continuous TBC. It can also be shown that this discretized boundary condition (BC) is not reflection-free. Alternatively, one could start directly from the Crank-Nicolson FD discretization of PE, done by Ehrhardt and Arnold [19], and derive numerically exact Discrete Transparent Boundary Condition (DTBC), that involves all the boundary field values starting from the initial plane. For example, if the field is desired at the 1,000th range step, the exact discrete BC will involve convolution of field values on the boundary layer at all the previous 999 range steps. Although accurate, DTBC will increase the CPU time, particularly for long ranges and there is a need for considering approximate BCs that are local.

Domain truncation for wave propagation that uses PE method constitutes the first motivation of this study. Previously Collino [15] implemented PML for a variational solution to PE, while Levy [47] proposed it as a straightforward truncation for finite-difference (FD) techniques for PE. However, there are no numerical implementation results for PML adapted to FD schemes of PE so far. Our initial goal is to provide some numerical comparison results for PML, when adapted to narrow-angle PE. A question that arises with the use of PML to PE is how effective it is, given that the PE is most accurate in the region of validity where the PML is most reflective, i.e. for zero grazing angle.

Regarding domain truncation for PE, our main motivation is to study approximate BCs that reduce the costs incurred in boundary layer convolution in DTBC. The authors in [2] have suggested a localization approach which is conditionally stable and does not allow one to pre-assess if a given approximation will be stable, unless the actual computation is performed. Therefore we are urged to introduce approximations of DTBC that are stable, or allow assessment of instability easily and allow stabilization schemes. Also, the approximate BCs are also desired to have lower computational cost of the convolutions present in the original DTBC. The comparison of these approximate BCs with the PML in far-range propagation environments is worth studying, since the PML is known not to be well-absorbing for far ranges where the propagation angles are very small [46].

Besides the efficient computation of numerical problems through appropriate domain truncation, another aspect of computational complexity that is of interest to reduce is the problem of uncertainty quantification using minimal resources. Research topics in electromagnetics with such interest include but not limited to propagation in random media [33, 96], [89], statistical variability of components [82, 83, 48], electromagnetic field interaction in biological tissues [23], [53] and random walk models of waves [22, 39, 17]. The cost reduction in propagation problems with uncertainty will constitute the second focus of this study.

The source of uncertainties in electromagnetics may be due to random radiating sources (excitation), random boundaries or random domain parameters. The uncertainties are in the most general sense represented as random processes, in which case pre-processing of the given randomness may be required. For instance one may decompose a given random process to finite number of random variables (RV) through Karhunen-Loève transform [51]. This decomposition is not necessary for problems involving finite number of independent RVs, which will also be the case throughout this study.

The most common sampling method to perform mean value integrations is the Monte-Carlo (MC) sampling. MC sampling has a convergence rate of $1/\sqrt{Q}$ [20], where Q is the sample size (number of realizations). One should keep in mind the nice feature of MC sampling that the convergence rate is independent of dimensionality (N), i.e. one would get the same convergence rate however big N is. This is not the case in other sampling based techniques which can provide faster convergence for low N. However, the dependence on dimensionality is one of the major concerns in sampling functions of high dimensional random spaces. A practical reason to seek alternatives to MC sampling is the sample reduction, i.e. one desires to achieve given accuracy with a smaller sample size Q. The sampling size reduction usually comes along with the convergence rate improvement, thus sample size reducing alternatives to MC sampling offer better convergence rates too.

Several alternatives to MC sampling have been developed by researchers until last decade, and these techniques are often referred to as "variance reduction techniques". These include Importance Sampling [13], Latin Hypercube Sampling (LHS) [58], [81] and Markov Chain Monte Carlo (MCMC) [49]. Another series of techniques based on sampling of low-discrepancy sequences are the Quasi Monte Carlo (QMC) techniques, which include sequences due to Halton [31] and Sobol [80]. Both the variance reduction techniques and the low discrepancy sampling techniques offer size reductions of up to an order, but may become worse than MC sampling for problems with very high dimensionality, often termed as "the curse of dimensionality".

A more recent development was achieved by Xiu [95, 94, 93], where they generalized Wiener's homogeneous chaos of Gaussian processes [92] to arbitrary processes each with a choice of orthogonal basis. This is termed generalized polynomial chaos (gPC) technique. In this technique, the inputs and outputs of the model problem with randomness are projected onto a complete space spanned by the basis of orthogonal polynomials. A Galerkin projection carried out in the spanned space transforms

the stochastic problem into a system of coupled differential equations with deterministic unknowns. Such a weak formulation was termed Stochastic Galerkin (SG), and any finite moment of the originally desired random output (target) can be computed from the coupled system without any sampling, unless the original stochastic system have highly non-linear terms that do not allow closed form expressions of the target function's moments. For scattering applications especially, the dependence on RVs are highly nonlinear, thus sampling based methods are inevitable. In this regard, the sparse grid collocation (SGC) method utilizes fast convergence rate of gPC, but avoids coupled nature of SG. The function of interest is expanded by gPC, where the mean value integration is performed via independent calls of the function on a set of cubature points (grid nodes). The sparse grid formation is independent of the target function, i.e. the function under uncertainty for which we seek the moments in a random domain.

In cases where the target function is highly non-smooth, e.g. when the field is highly sensitive to certain RVs, SGC does not offer superiority over conventional MC methods, and adaptive algorithms for sparse grid construction in SGC become attractive. The fast convergence of SGC in interpolation of the target function depends on the smoothness, and it is not fair to assume that the target function under uncertainty meets the smoothness condition of Smolyak algorithm, derived in [64]. It is thus crucial to refine the sparse grid around regions of non-smooth target function output, and sample less the smooth regions of the random domain. From a mathematical point of view non-smoothness may appear as discontinuities or regions of the random domain where there is rapid fluctuation in the target function output.

In cases of high dimensional problems, ($N \gg 1$), even the adaptive sparse grids suffer the curse of dimensionality. The high dimensional model representations (HDMR) [70], [71] provide an exact representation for high dimensional functions in terms of lower dimensional sub-functions, which we will refer to as "components". Each com-

ponent in the HDMR represents collective contribution of the RVs it includes on the target function interpolation, thus allows measure of to what extent each RV, or combination of RVs, dominate the target function behavior. Use of HDMR for dimensionality reduction has recently attracted attention of various authors [21], [55], [29]. Although the published literature reveals acceptable convergence rates for up to 500 dimensions in some partial differential equations with random input data, it is a question if electromagnetic propagation and scattering will be subject to such an enhancement over existing performance with sparse grids. The authors in [101] have applied this technique for electromagnetic compatibility and interference (EMC/EMI) analysis, and obtained desired characterization at 240 dimensions. Ma and Zabaras [55] have merged their adaptive sparse grid method with HDMR, and given a thorough interface algorithm between HDMR and their method. We introduce some modifications to their interface algorithm, and make use of it in our problems, which will be referred to as HDMR+ASGC. Lately, Jakeman and Roberts introduced another improved scheme, $h-$GSG, which can also be attractive for certain applications [36].

Regarding the use of sparse grids for propagation problems with uncertainty, there are several applications to be addressed, which have conventionally been tackled with MC sampling. However, given the fact that the performance of these methods are limited for non-smooth behavior and for high$-N$, we are interested in tackling problems of where the dimensionality can controllably be increased, and the smoothness of the target function can favor adaptive methods via rendering certain RVs more important than the rest of the RVs. In this respect, we choose to begin with a simple 1-D (in space) scattering application in terms of the numerical solution to it, yet the target function behavior in the random space can become highly non-smooth. Through such an example we intend to compare the state-of-the-art SGC methods in their performance in EM scattering and propagation with uncertainty in intrinsic

domain parameters, where we have the flexibility to assume as high N as desired, and assume each RV having as large support as desired.

The focus of our motivation with SGC methods extend to their applications in long-range propagation phenomena with PE solvers, in accordance with the first half of this work. A forward scattering approach in computing observed field far from the transmitter location, waves propagating over perfectly conducting (PEC) rough surface has conventionally been tackled with MC sampling [61], [45]. The nature of this application requires a large number of RVs ($N \gg 1$), as the rough surface generation follows a spectral approach in which Discrete Fourier Transforms (DFTs) of identically distributed independent RVs are used [38]. A major challenge for the SGC methods with such application is that in this problem the importance of RVs cannot be differentiated in their contribution to the target function (observed field), therefore it is questionable if the randomness will be present in isolated subspaces of the $N-$dimensional random space.

Far-range propagation problems with PE methods may not include uncertainty solely in the terrain shape, but practically in the refractive index of the air for atmospheric communications. Inhomogeneous atmospheric refractive index has been investigated thoroughly for decades, where conventional analytical models exist based on measurements [4, 86, 28, 91]. Although the refractive index in the most general sense varies as a function of all dimensions in real-time due to atmospheric pressure, water-vapor pressure and temperature variations [8], [84], in PE research spatial variation only along the elevation direction out from Earth surface is given a significant role. This variation usually results in ducting layers around certain elevation, and has been given analytical expressions derived from measurements. A review of different ducting formations observed in various coastal middle latitude locations were given in [97]. In this dissertation, we tackle the propagation problem using SGC methods.

1.2 Original Contributions and Outline

There are two separate aspects in this study, while EM propagation utilizing PE methods is common to both parts. Two different techniques to solve PE with different strengths and application areas, are presented in Chapter 2. The first aspect of the study contains the results for efficient absorbing boundary conditions in a deterministic propagation environment [66], [65]. The second aspect of the dissertation is our work in uncertainty quantification for electromagnetic propagation and scattering with uncertainty. In Chapter 4, the SGC methods we use are presented. In Chapter 5, we present three sample applications in EM propagation and scattering [67], [68]. Below we itemize the contributions in the two aspects of this study:

1. Efficient and localized absorbing boundary conditions for the finite difference implementation of the parabolic equation. Two different approximations to the discrete transparent boundary condition (DTBC) are introduced.

    - LDTBC: The first localization to DTBC, originally proposed by [2]. Reduces the spatial-convolution size in DTBC without sacrifying accuracy, however it is conditionally stable. We introduced a stability check scheme for a given approximation. The convolutions involved in LDTBC have an exponential cost dependence with respect to propagation distance (range). Therefore besides being conditionally stable, LDTBC is not practical at far ranges.

    - LDTBC_2: The second localization to DTBC. It reduces the cost of convolutions with respect to range to linear rate through recursion. We proposed and applied a method for assuring stability in the coarse of numerical simulation. The long-range simulations revealed better accuracy than the perfectly matched layer (PML) absorption.

2. Application of sparse grid collocation (SGC) methods to three different problems. Two different recently developed adaptive algorithms that allow self-learning sampling by SGC method in the random space, *viz.*, $h-$GSG and HDMR+ASGC, are utilized. The three applications that are targeted for assessing their effectiveness in electromagnetic field calculations are:

   - The expected reflection coefficient for normal incidence to a series of K lossy dielectric slabs, each with random permittivity and permeability (Section 5.1).

   - The expected propagation factor (PF) of wave propagation in free-space in the presence of randomly shaped conducting ground (Section 5.2).

   - The expected PF and complex field magnitude of wave propagation in lower troposphere, where randomly varying atmospheric ducts are present. The uncertainty model is based on published measurements, and the results with adaptive SGC methods reveal practical alternatives to Monte-Carlo sampling.

CHAPTER 2

PARABOLIC EQUATION METHODS

2.1 Introduction

Radiowave propagation governed by Helmholtz equation can be approximated by the Parabolic Equation (PE) under certain circumstances if the spectral content of waves is narrow around the propagation axis and refractive index inhomogeneity of the atmosphere is smooth [46]. Conventional narrow-angle PE approximation of wave propagation assumes maximum ray angle to be within $\pm 15^o$ with respect to the axis of propagation (range). The main distinction between the Helmholtz equation and PE is the reduction of 2nd order derivative to a 1st order derivative along the range, which is based on ignoring back-scattering in the domain. This facilitates a marching-in range technique for numerical computation. Most practical PE applications are concerned with far-range wave behavior, e.g. in tropospheric calculations, where the grazing angles are already very small, which makes the error due to large propagating angles affordable. Another application of PE is propagation prediction in tunnels with lossy walls, where the wave content in long ranges is dominated by the small grazing angles as well [57]. In optics and photonics research on the other hand, the PE methods have been widely used, often referred to as the Beam Propagation Method [30, 34].

Two schemes are available for the solution of PE, first of which is the Split-Step Fourier PE technique (SSPE) that is applicable when analytical eigenfunctions exist for the underlying geometry [44], [18]. This scheme has extensively been used for long-range communications. Purely numerical schemes based on Finite Differences

(FD) on the other hand are applicable for more general geometries with boundaries. The popular methods based on FD discretization include the Crank-Nicolson scheme [78] and the Alternating Direction Implicit (ADI) method [56]. Throughout this work problems that require numerical solutions with the SSPE and Crank-Nicolson FD scheme will be encountered, therefore here we will detail only these methods. For brevity, we refer to the Crank-Nicolson FD scheme simply as FDPE. While both methods have advantages depending on the application type [74], for long-range propagation it is common to use the latter in order to avoid numerical issues associated with long-range absorbing boundary modeling in the former [66].

We will initially give the derivation of PE approximation. Afterwards, SSPE and FDPE will be detailed.

2.2 Standard PE in Atmosphere

The scalar Helmholtz equation for the solution $u(t, x)$ to the time-harmonic Maxwell's equations in a two-dimensional space (t, x), with an inhomogeneous atmosphere above the Earth surface, is [44]:

$$\nabla^2 u(t,x) + k_o^2 \left[n^2(t,x) + 2\frac{x}{a_e} \right] u(t,x) = 0, \tag{2.1}$$

where $\nabla^2 \equiv \left(\frac{\partial^2}{\partial t^2} + \frac{\partial^2}{\partial x^2} \right)$. The above equation was derived utilizing a transformation from the spherical Maxwell's equations to the rectangular coordinates (t, x) whereas the spherical origin is assumed the inner core center of the Earth, a_e is the Earth's radius. Here t represents the range coordinate variable, tangential to the Earth surface, and x the elevation coordinate variable of the atmosphere, normal to the Earth surface, k_o is the wave-number in free space at the radian frequency ω, $n(t, x)$ is the refractive index of the atmosphere which can deviate slightly from the free-space case having $n(t, x) \equiv n_o = 1$. Throughout this work we assume a $e^{-i\omega\tau}$ time convention,

where $i = \sqrt{-1}$, and τ is the time variable. Now assume no wave propagation along negative 't', and in accordance define a reduced wave function $\psi(t,x) := e^{-ik_o t}u(t,x)$. Then, the Helmholtz equation can be re-written in terms of the reduced field by substituting it in (2.1):

$$\frac{\partial}{\partial t}\left[e^{ik_o t}\left(\frac{\partial}{\partial t}\psi + ik_o\psi\right)\right] + e^{ik_o t}\left(\frac{\partial^2}{\partial x^2} + k_o^2 n^2 + 2k_o^2\frac{x}{a_e}\right)\psi = 0. \tag{2.2}$$

Next, the additional assumption that the variation of ψ along t is gradual is enforced, so that $|\partial^2\psi/\partial t^2| \ll k_o\,|\partial\psi/\partial t|$, and the smooth inhomogeneity via $n+1 \approx 2$, we arrive at the standard PE in the reduced variable $\psi(t,x)$ as:

$$\frac{\partial\psi}{\partial t} = \left[\frac{i}{2k_o}\frac{\partial^2}{\partial x^2} + ik_o\left(n + \frac{x}{a_e} - 1\right)\right]\psi. \tag{2.3}$$

Note that equation (2.3) is parabolic type due to the first order derivative in t, rather than the elliptic Helmholtz equation in (2.1). In the next sections, we will present the split-step solution and the Crank-Nicolson solution to (2.3).

2.3 Split-Step Parabolic Equation (SSPE) Formulation

In the form given in (2.3), $\psi(t,x)$ has a solution in the form of a propagator along positive 't', updating the solution every range step Δt. However, the complicated operator in the brackets in (2.3) could be simplified by use of Fourier transformations defined between the spatial $x-$domain, and the spectral $p-$domain. With the assumption of perfectly conducting smooth Earth surface, the SSPE makes use of sine-transforms to update the field quantity along t:

$$\psi(t_o + \Delta t, x) = e^{ik_o(\overline{m}-1)\Delta t}\int_0^\infty e^{-ip^2\frac{\Delta t}{2k_o}}\tilde{\psi}(t_o,p)\sin px\ dp, \tag{2.4}$$

where $\overline{m}$ is an average modified refractive index in the range step $(t_o, t_o + \Delta t)$ which can tolerate only smooth variation in refractive index along height. The modified refractive index is $m = n + x/a_e$. Apart from being simple to implement using Fast Fourier Transforms (FFTs), the split-step Fourier propagator is robust with respect to Δt. On the other hand, one needs to take into consideration the maximum spectral component present in the narrow-angle PE to be solved, so that the spatial discretization size Δx does not cause aliasing in discrete transform pairs. Specifically, the maximum spectral component in $p-$domain is $p_{max} = k_o \sin\theta_{max}$, where θ_{max} is the maximum angle of propagation with respect to t, that we assume to be less than 15^o in accordance with the narrow-angle PE [46]. Note that to prevent aliasing $p_{max} < 2\pi/\Delta x$ should be assured. Therefore, the restriction in discretization of x becomes

$$\Delta x \leq \frac{2\pi}{k_o \sin\theta_{max}}. \tag{2.5}$$

The forward sine-transform that transforms x-varying field into the spectral p-domain is:

$$\tilde{\psi}(t,p) = \frac{2}{\pi}\int_0^\infty \psi(t,x)\sin px \; dx. \tag{2.6}$$

Note that the Dirichlet boundary condition on Earth surface, *viz.*, $\psi(t,0) = 0$ is already satisfied in (2.4). Before each of forward and backward transforms in the course of the propagator above, the nonzero field quantity at a designated truncation height x_{max} however needs to be smoothly tapered to prevent numerical reflections incurred in numerical transforms. For this, at each step we pre-multiply spatial and spectral quantities with a Hanning window as suggested in [44].

Besides the discretization restriction in (2.5), the range step Δt can be fairly large in practical SSPE applications, which makes this technique the natural choice for long-range propagation environments.

The refractive index n in lower troposphere is in the most general case modelled as having a slight negative gradient with height x, and is independent of operating frequency for microwaves [77]. However, roughly around 100 meters elevation, refractive index changes often exhibit a "ducting effect" that has attributes changing in real-time. For demonstration of a test case of propagation in the presence of a ducting layer, we will use the same model and excitation, and compare the propagation factor (PF) result with that given in [44]. The modified refractivity for this model is:

$$M(x) = \begin{cases} 340 + 0.118x, & x < 135\text{m} \\ 499 - 1.06x, & 135\text{m} \leq x < 150\text{m} \\ 322.33 + 0.118x, & 150\text{m} \leq x, \end{cases} \tag{2.7}$$

where $M = (n + x/a_e - 1) \times 10^6$. For this example, the excitation is a unit delta function from an antenna located at $x_t = 30$m height at $t = 0$, and operating at 3 GHz, and observation is at $t_{obs} = 80$ km. The PF is defined as the total observed field in the presence of inhomogeneities,ψ_{tot}, normalized by ψ_{FS}:

$$PF = \left| \frac{\psi_{tot}(t_{obs}, x)}{\psi_{FS}(t_{obs}, x)} \right|, \tag{2.8}$$

where ψ_{FS} is the field solution when the excited source propagates in free-space.

For the refractivity profile in (2.7), the Split-Step propagator we use accurately matches with the data manually extracted from Kuttler and Dockery [44], and depicted in Figure 2.1. Next, we will consider the FDPE for the homogeneous (free-space) environment.

2.4 Crank-Nicolson PE Scheme (FDPE)

The second formulation for numerical solution of (2.3), FDPE, is based on the FD discretization according to a stencil as depicted in Figure 2.2. We assume the discrete

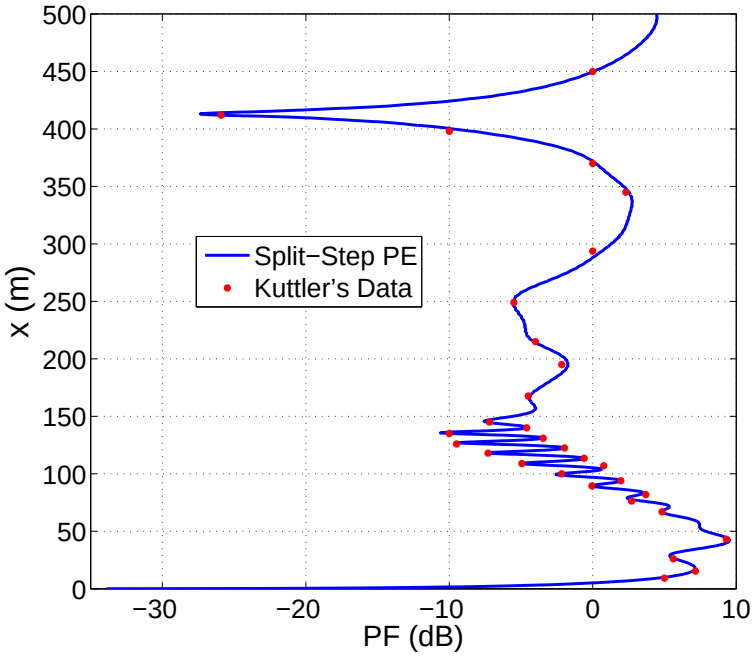

Figure 2.1: Propagation factor (dB) along height, at 80 km, for an antenna located at $t = 0, x_t = 30$ m, operating at 3 GHz. The discretization parameters are $\Delta t = 25$ m, $\Delta x = 0.1$m.

notation $\psi(m\Delta t, j\Delta x) =: \psi_j^m$, and $n(m\Delta t, j\Delta x) =: n_j^m$ where $m \in \mathbb{N}$ and $j \in \mathbb{N}$ are the discrete indices along the range and elevation axes, respectively. In (2.3), both the second derivative along x and the first derivative along t will be discretized using second order central difference approximation. The derivative along x is enforced at discrete index j, whereas the derivative along t is enforced at a hypothetical half-index $m + 1/2$:

$$\begin{aligned} \left.\frac{\partial^2 \psi(t,x)}{\partial x^2}\right|_{x=j\Delta x} &\approx \frac{\psi(t,(j-1)\Delta x) - 2\psi(t,j\Delta x) + \psi(t,(j+1)\Delta x)}{(\Delta x)^2}, \\ \left.\frac{\partial \psi(t,x)}{\partial t}\right|_{t=(m+1/2)\Delta t} &\approx \frac{\psi((m+1)\Delta t, x) - \psi(m\Delta t, x)}{\Delta t}. \end{aligned} \tag{2.9}$$

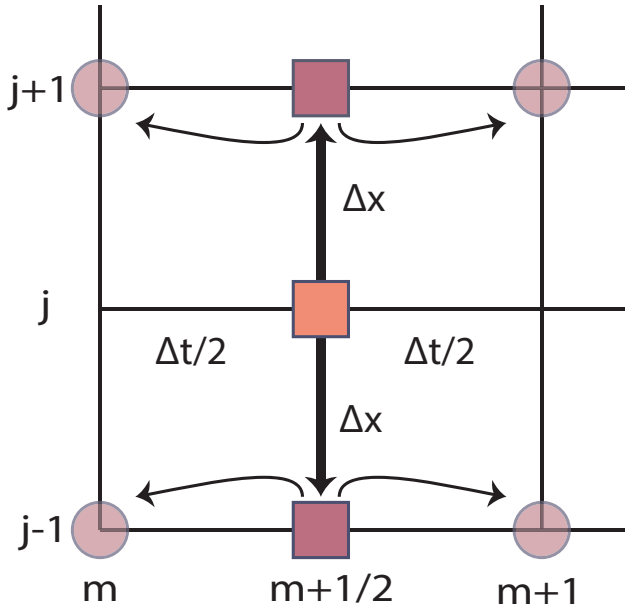

Figure 2.2: Stencil for FDPE discretization. Through the arithmetic averaging invoked at $m + 1/2$, only the indices in the four corners (disks) of this stencil are used in the resultant discrete equation.

Finally, (2.9) are enforced in (2.3), and all terms that reside at hypothetical range index $m + 1/2$ are approximated as the arithmetical average of the same terms avail-

able at ranges m and $m+1$. This is the unconditionally stable and implicit Crank-Nicolson scheme, and for (2.3) it results:

$$\begin{aligned}\psi_j^{m+1}\left[R+2i-2i(k_o\Delta x)^2\left(n_j^{m+1}+\frac{j\Delta x}{a_e}-1\right)\right]-i\psi_{j-1}^{m+1}-i\psi_{j+1}^{m+1}\\ =\psi_j^m\left[R-2i+2i(k_o\Delta x)^2\left(n_j^m+\frac{j\Delta x}{a_e}-1\right)\right]+i\psi_{j-1}^m+i\psi_{j+1}^m,\end{aligned}\tag{2.10}$$

where $R=\frac{(2k_o\Delta x)^2}{k_o\Delta t}$ is a unit-less parameter. Upon discretization of the computation domain (t,x), the FDPE in (2.10) is used as the discrete equation that solves for the reduced wave function ψ in (2.3). Now assume the computational domain $[0,M\Delta t]\times[0,J\Delta x]$, where the elevation axis is uniformly discretized in $J+1$ indices, and the range axis is discretized in $M+1$ indices. The march-in step solution along t is performed by enforcing (2.10) at each range step, $m=0,1,...,M$. The resultant set of equations are then represented in the following matrix equation:

$$\mathbf{S}^{m+1}\underline{\psi}^{m+1}=\mathbf{T}^m\underline{\psi}^m,\tag{2.11}$$

where $\underline{\psi}^m$ and $\underline{\psi}^{m+1}$ are the vector of field values along x at discrete ranges m and $m+1$, respectively. The matrices $\mathbf{S}^{m+1},\mathbf{T}^m$ are used to update the field vectors. If one assumes truncation of the domain at $x=0$ and $x=J\Delta x$ with Dirichlet boundary conditions, *viz.*, $\psi(t,0)=\psi(t,J\Delta x)=0$, the matrices can be written as:

$$\mathbf{S}^{m+1}=\begin{bmatrix}s_1^{m+1} & -i & 0 & . & .\\ -i & s_2^{m+1} & -i & 0 & .\\ 0 & -i & s_3^{m+1} & -i & 0\\ . & . & . & . & .\\ . & . & 0 & -i & s_{J-1}^{m+1}\end{bmatrix},\tag{2.12}$$

$$\mathbf{T}^m = \begin{bmatrix} t_1^m & i & 0 & . & . \\ i & t_2^m & i & 0 & . \\ 0 & i & t_3^m & i & 0 \\ . & . & . & . & . \\ . & . & 0 & i & t_{J-1}^m \end{bmatrix}, \tag{2.13}$$

where s_j^{m+1} and t_j^m are the terms in square brackets in the left and the right of the equality sign in (2.10), respectively.

Note that (2.10) is in the most general sense discretizes the inhomogeneous atmosphere, and is often used for propagation in free-space while neglecting the effect of the finite Earth radius a_e. Since SSPE is a more common choice in far-range and high-elevation problems where t, x become comparable to a_e, FDPE is often formulated without the term that contains a_e in (2.10). This case will be utilized for propagation in free-space in the next chapter.

CHAPTER 3

DOMAIN TRUNCATION FOR FDPE

In this chapter we use the FDPE scheme in Section 2.4 in free-space and formulate efficient transparent boundary conditions (TBCs) for FDPE. As discussed in Chapter 2, mainly due to computational reasons, the FDPE scheme is usually used for shorter range problems that are truncated at lower elevations. Therefore, here the effect of Earth radius a_e is omitted, and we assume no atmospheric inhomogeneity, i.e. $n(t,x) \equiv 1$. The PE in this form simplifies to:

$$\frac{\partial \psi}{\partial t} = \frac{i}{2k_o}\frac{\partial^2 \psi}{\partial x^2}, \tag{3.1}$$

for which the FDPE in (2.10) reduces to:

$$\psi_j^{m+1}\left(R+2i\right) - i\left(\psi_{j-1}^{m+1} + \psi_{j+1}^{m+1}\right) = \psi_j^{m}\left(R-2i\right) + i\left(\psi_{j-1}^{m} + \psi_{j+1}^{m}\right). \tag{3.2}$$

Through the two-dimensional free-space we will demonstrate the performance of the TBCs in comparison to the perfectly matched layer (PML) formulated for the same space. For this, in the next section we introduce the PML applied to the FDPE. Another section will be reserved for an alternate derivation of the discrete transparent boundary condition (DTBC), after which the two "localized" DTBCs will be discussed as more efficient alternatives to the original DTBC and the PML. At the end, sample simulation results with aforementioned truncation methods along with performance comparison will be shown. Majority of the figures and data displayed in this chapter is found in [66].

3.1 PML Implementation for FDPE in Free-Space

The two-dimensional PML is constructed by replacing the height x with complex stretched-coordinate $\widetilde{x}$ [15] given by:

$$\widetilde{x}(x) = x + i \int_0^x \sigma(s) ds. \tag{3.3}$$

The damping factor σ is the normalized conductivity (unit-less), a nonnegative quantity that is used to diminish the waves propagating in both positive and negative x. Note that plus sign in (3.3) is consistent with the $e^{-i\omega\tau}$ time convention, that any component of the form $e^{ik_o\widetilde{(x)}}$ radiated out in positive x will not point to a nonphysical solution. We use a quadratic profile along x for σ:

$$\sigma(x) = \begin{cases} \sigma_o \eta_o k_o (x - x_h)^2 & , x \geq x_h \\ 0 & , x < x_h \end{cases} \tag{3.4}$$

This is not the only selection one could make for damping waves and other models exist [42], however above selection ensured good performance. In (3.4) η_o is the wave impedance in free space and σ_o is the true conductivity (S/m). Recall that the product $\sigma_o \eta_o$ has units m^{-1} thus $\sigma(x)$ remains unit-less. In (3.4) x_h denotes the domain height at which it is truncated. Another height x_t is where the excitation will be placed at the source range of $t = 0$. Height x_t will be referred to as the mean height of the excited Gaussian source that will be discussed later in the paper. The PML, which is placed above the elevation of x_h, is backed with a perfectly conducting electric (PEC) surface, therefore waves entering the PML will experience damping both along positive x, and along negative x after they reflect back from the PEC surface. The finite thickness of the PML is δ.

According to the coordinate stretching in (3.3), the homogeneous PE in (3.1) is modified as:

$$\frac{\partial \psi}{\partial t} = \frac{i}{2k_o} \frac{1}{1 + i\sigma(x)} \frac{\partial}{\partial x} \left[\frac{1}{1 + i\sigma(x)} \frac{\partial}{\partial x} \psi \right]. \tag{3.5}$$

Similar to the FDPE formulation in Section 2.4, we will use the FD stencil of Figure 2.2, which results in the below discrete equation in the presence of the PML layer:

$$\begin{aligned} &\psi_j^{m+1} \left[R + \tfrac{i}{1+i\sigma_j} \left(\tfrac{1}{1+i\sigma_{j+1/2}} + \tfrac{1}{1+i\sigma_{j-1/2}} \right) \right] - \tfrac{1}{1+i\sigma_j} p_j^{m+1} \\ &= \psi_j^m \left[R - \tfrac{i}{1+i\sigma_j} \left(\tfrac{1}{1+i\sigma_{j+1/2}} + \tfrac{1}{1+i\sigma_{j-1/2}} \right) \right] + \tfrac{1}{1+i\sigma_j} p_j^m, \end{aligned} \tag{3.6}$$

where

$$\begin{aligned} p_j^{m+1} &= \frac{i}{1 + i\sigma_{j+1/2}} \psi_{j+1}^{m+1} - \frac{i}{1 + i\sigma_{j-1/2}} \psi_{j-1}^{m+1}, \\ p_j^m &= \frac{i}{1 + i\sigma_{j+1/2}} \psi_{j+1}^m + \frac{i}{1 + i\sigma_{j-1/2}} \psi_{j-1}^m. \end{aligned} \tag{3.7}$$

and $\sigma(j\Delta x) =: \sigma_j$. Figure 3.1 depicts the computation domain, truncated by the PML above height x_h. Note that the conductivity is discretized at half-integer indices $j+1/2$ in (3.6), therefore the discretization for the PML is twice as fine as the domain of interest. Note in (3.6) that $\sigma_o = 0$ basically reduces it to (3.2). The rays that enter the PML experience a controlled loss twice as they reflect back into the domain. We have control over the reflection of rays through σ_o and δ. The reflection coefficient from the PML for a ray with paraxial angle θ (with respect to t axis) is [15], [10]:

$$\Gamma(\theta) = -\exp\left[-i2k_o \sin\theta \widetilde{x}(x_h + \delta)\right]. \tag{3.8}$$

This results in an equation for the true conductivity in terms of the desired reflection coefficient as:

$$\sigma_o = \frac{-3|\ln \Gamma(\theta_o)|}{2k_o^2 \sin\theta_o \eta_o \delta^3}. \tag{3.9}$$

One aspect to note about reflection is that, it is smaller for wider angle θ, which leads to the fact that PML simulates a better absorption for waves propagating at wider angles than those at shallower angles [46]. The reflection coefficient is one in magnitude for $\theta = 0$. That is why σ_o is chosen by setting the reflection Γ for a small grazing angle, i.e. a small θ_o, so that higher angle content will reflect even less back into the domain. One restriction on layer thickness δ is that it is not desirable to set it too high, since it will increase the matrix sizes for each marching-in range computation. Typical values we select in the simulations with PML are $\theta_o = 0.5^o$, $\Gamma(\theta_o) = 10^{-3}$, and $\delta = 10\lambda$, where λ is the free-space wavelength.

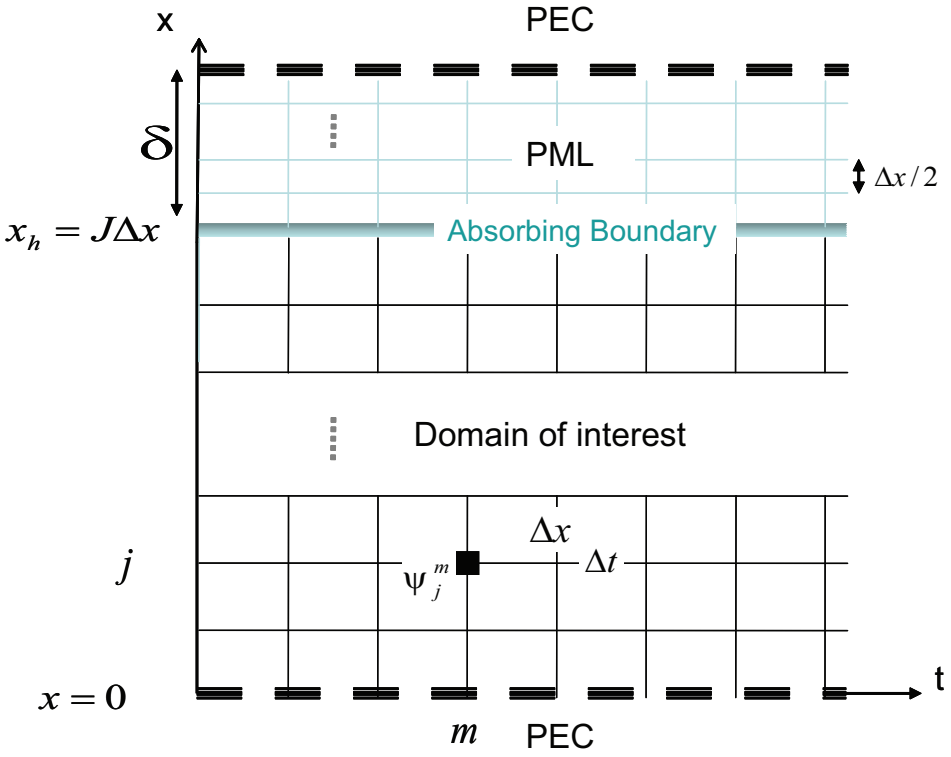

Figure 3.1: Computation domain, top layer being absorbing boundary and bottom layer PEC

If one writes (3.6) in terms of a matrix equation to update the vector of fields at each range step m, $\underline{\psi}^m$, it is in the same form as in (2.11). However in this case the

matrices $\mathbf{S}^{m+1}$, $\mathbf{T}^m$ are both $(J-1+2\delta/\Delta x)-$by$-(j-1+2\delta/\Delta x)$, due to the $\Delta x/2$ discretization of the PML in Figure 3.1.

3.2 Discrete Transparent Boundary Condition (DTBC) Derivation

We will now derive and approximate the DTBC directly for the Crank-Nicolson scheme in (3.2). The original derivation of DTBC is given in [19]. However, we derive a newer form that is amenable to approximations. Solving the discrete PE on and above the boundary layer while assuming a decaying nature of the fields above this layer results in [19]:

$$\sum_{u=0}^{m} \kappa_u \psi_j^{m-u} + \sum_{v=0}^{m} \mu_v \psi_{j-1}^{m-v} = 0, j \geq J. \tag{3.10}$$

κ_u and μ_v are weights of convolutions on a layer j and on the layer $(j-1)$, below it. Such a convolution-type relation of fields leads us to use $\mathcal{Z}$-transforms, which translates the relation of field values on successive layers on or above the boundary layer to a polynomial in the complex $\mathcal{Z}$-domain. We will use a $\mathcal{Z}$-transform as

$$\mathcal{Z}\{\psi_j^m\} =: U_j(z) = \sum_{m=0}^{\infty} \psi_j^m z^m, \tag{3.11}$$

where $|z| < 1$ and an inverse $\mathcal{Z}$-transform as

$$\psi_j^m = \frac{1}{2\pi i} \oint_{C_j} U_j(z) z^{m-1} dz. \tag{3.12}$$

The inversion contour C_j is counter-clockwise as indicated in Figure 3.2. Also, $\psi_j^0 = 0$ is assumed for $j \geq J-2$. This is crucial for the derivation of DTBC [19]. Taking the $\mathcal{Z}$-transform on both sides of (3.2) results in:

$$(1+z)\,U_{j+1}(z) + [(1-z)\,iR - 2\,(1+z)]\,U_j(z) + (1+z)\,U_{j-1}(z) = 0, \qquad (3.13)$$

where $j \geq J-1$. More specifically, the transfer function relating field on the boundary layer in z-domain to the field on the layer just below it is:

$$\nu(z) = \frac{U_{J-1}(z)}{U_J(z)} = 1 - i\frac{R}{2}\frac{1-z}{1+z} - \sqrt{-i\frac{R}{2}\frac{1-z}{1+z}\left(2 - i\frac{R}{2}\frac{1-z}{1+z}\right)}. \qquad (3.14)$$

The transfer function $\nu(z)$ in general is multi-valued, therefore the $\sqrt{.}$ operator above is defined to ensure $|\nu(z)| > 1$, which reflects decaying nature of $U_j(z)$ for $j \geq J-1$. Let f denote a modified transfer function defined as:

$$\begin{aligned} f(z) &:= (1+z)\nu(z) \\ &= (1+z) - 2i(1-z)\tan\alpha_o - 2\tan\alpha_o\sqrt{-ie^{-i\alpha_o}\csc\alpha_o}\times \\ &\times \sqrt{-z^2e^{2i\alpha_o} + 2iz\sin\alpha_o e^{i\alpha_o} + 1}, \end{aligned} \qquad (3.15)$$

with $\tan\alpha_o = \frac{R}{4}$. We introduce a new variable $\zeta = -ize^{i\alpha_o}$ and take the first derivative of (3.15). This is so that the resulting function $\frac{1}{\sqrt{\zeta^2-2\sin\alpha_o\zeta+1}}$ can be expressed in terms of Legendre polynomials as $\sum_{l=0}^{\infty}\zeta^l P_l(\sin\alpha_o)$ where $P_l(.)$ are the Legendre polynomials [1]. The derivative of f with respect to ζ is:

$$f'(\zeta) = A + B\frac{\zeta - \sin\alpha_o}{\sqrt{\zeta^2 - 2\sin\alpha_o\zeta + 1}}, \qquad (3.16)$$

where

$$\begin{aligned} A &= -\sin\alpha_o + i\left(\frac{1+\sin^2\alpha_o}{\cos\alpha_o}\right), \\ B &= -2i\sqrt{\tan^2\alpha_o + i\tan\alpha_o}. \end{aligned} \tag{3.17}$$

Using the Legendre function representation of the quantity under the radical sign gives

$$f'(\zeta) = A - B\sin\alpha_o \sum_{l=0}^{\infty} \zeta^l P_l(\sin\alpha_o) + B\sum_{l=0}^{\infty} \zeta^l P_{l-1}(\sin\alpha_o), \tag{3.18}$$

with $P_{-1}(.) = 0$. The Taylor-series expansion of $f^{'}(\zeta)$ can be written as:

$$f'(\zeta) = \sum_{l=0}^{\infty} c_l \zeta^l, \tag{3.19}$$

with coefficients

$$\begin{aligned} c_0 &= A - B\sin\alpha_o P_o(\sin\alpha_o), \\ c_l &= B\left[P_{l-1}(\sin\alpha_o) - \sin\alpha_o P_l(\sin\alpha_o)\right],\ l = 1, 2, .. \end{aligned} \tag{3.20}$$

As already indicated the multi-valued $\sqrt{.}$ operator in (3.14) is defined such that $|f(0)| = |\nu(0)| > 1$. Using (3.19), the modified and exact transfer functions can finally be written as:

$$f(\zeta) = -\sum_{l=0}^{\infty} a_l \zeta^l,$$

$$\begin{aligned} a_0 &= -f(0), \\ a_l &= -\frac{c_{l-1}}{l},\ l = 1, 2, .., \infty, \end{aligned} \tag{3.21}$$

and

$$\nu(z) = \frac{f(z)}{1+z} = -\frac{\sum_{l=0}^{\infty} \gamma_l z^l}{1+z}, \tag{3.22}$$

with $\gamma_l = (-i)^l e^{il\alpha_o} a_l$. The region of convergence of the series depends on the singularities of $\nu(z)$. This leads to the investigation of properties of the exact transfer function f in z-plane. The branch cut in z-plane for the function given in (3.14) is depicted in Figure 3.2, as a bold dashed curve separating the two sheets with $|\nu(z)| = 1$ on it. It can be shown that the branch points are at $z_0 = 1$ and $z_1 = (R+4i)/(R-4i)$. Repending on R the point z_1 in general could be in either of 1st or 2nd quadrants of the $z-$plane.

There is a practical reason why (3.14) or (3.22) is not suitable for direct use in the Crank-Nicolson scheme. Because we are interested in a bounded computation domain that starts at range $t = 0$, the infinite summation in (3.22) reduces to a convolution of size $M = \frac{t}{\Delta t}$ where t is the range of the present marching step. The upper limit in (3.22) will be referred as being M henceforth. This is usually a large number, especially for fine discretizations and far ranges. To have an idea of how this transfer function affects the boundary computation in the spatial domain and how ineffective the convolution is, the nodes used in convolution are depicted in Figure 3.3. There, the boundary is at Jth discrete layer and all the nodes on that layer are involved in the first summation in (3.10). The two nodes on $(J-1)$th layer contribute to the second summation in (3.10), i.e. only the first two terms are non-zero in the second summation. This is because of the second degree polynomial in the denominator of $\nu(z)$ in (3.22).

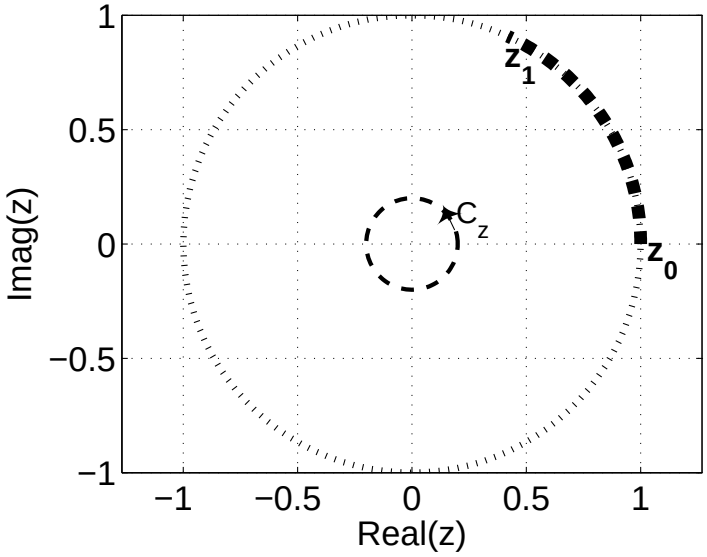

Figure 3.2: Branch cut on z-plane for $|\nu(z)| = 1$, $R = 0.63$. C_z is the inversion circle around origin.

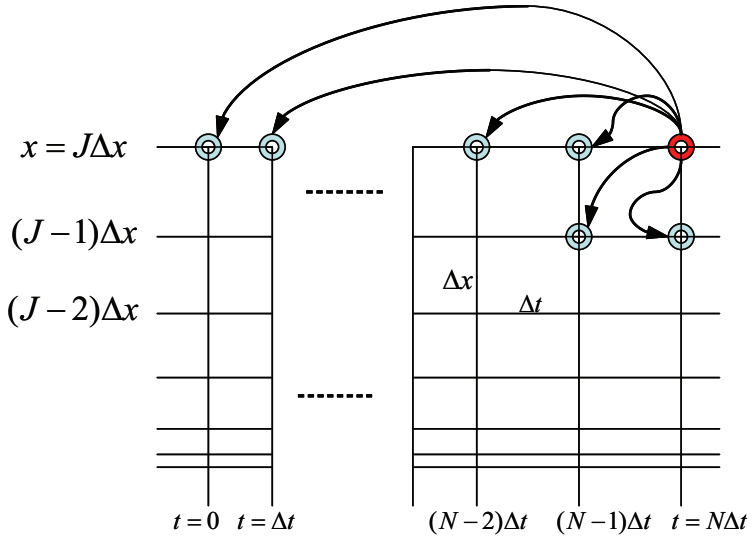

Figure 3.3: Exact DTBC convolution stencil. The two layers of nodes correspond to the two convolutions in (3.10). This stencil is valid at all elevations greater than $(J-1)\Delta x$

3.3 Localized DTBC (LDTBC) Approximation

The first approximation we consider, which was originally proposed in [19], is replacing the length$-(N+1)$ summation in (3.22) by a Padé approximant of order P/Q,

$$f(z) \approx -\frac{\sum_{u=0}^{P} d_u z^u}{\sum_{v=0}^{Q} e_v z^v}, \tag{3.23}$$

where d_u's and e_v's are determined by conventional Padé approximant procedure [5]. The Taylor series expansion derived in (3.22) is very convenient in this regard. We will set the leading denominator coefficient $e_o = 1$ for convenience. The relations (3.22) and (3.23) result in $\nu(z)$ also in a rational form:

$$\nu(z) = \frac{f(z)}{1+z} \approx -\frac{\sum_{u=0}^{P} d_u z^u}{\sum_{v=-1}^{Q} g_v z^v}, \tag{3.24}$$

where $g_v = e_v + e_{v+1}$ for $v = 0, 1, .., Q-1$, $g_Q = e_Q$ and $g_{-1} = e_o = 1$.

The transfer function $\nu(z)$ in (3.24) is plotted in Figure 3.4 for $z = 0.9e^{j\theta}$, $\theta = [0, 2\pi)$. It should be stressed at this point that the Padé approximation above is obtained by enforcing continuities at the origin in z-domain, thus an approximation of order P/Q is less valid at points closer to the unit circle than near the origin. Points on $|z| = 0.9$ circle are utilized above for the sake of demonstrating severity of the approximation (the approximation will be worst for $|z| = 1$). It is seen that an approximation of higher order is always favorable and that an approximation of order $P = 10/Q = 4$ is good enough to mimic the exact transfer function for this case. To appreciate the effect of using interior domain points, i.e. on one layer below the absorbing layer, the coefficient magnitudes for the two cases, $Q = 0$ case and $Q > 0$ case, are shown in Figure 3.5 for the same P value. Clearly, the dominance of low

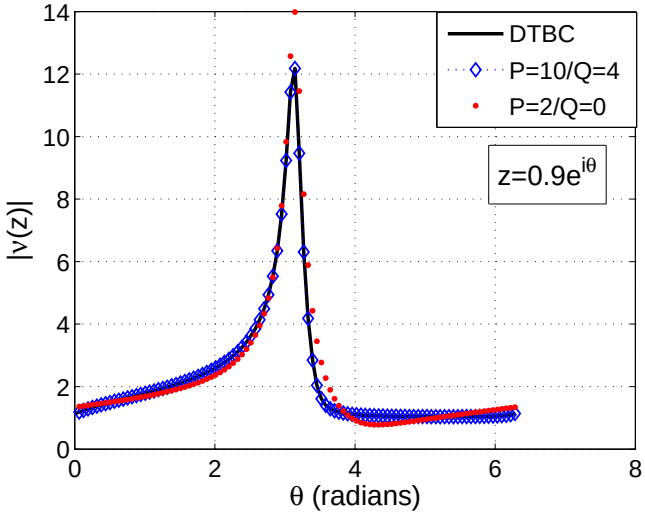

Figure 3.4: $|\nu(z)|$ for the z values on the $|z| = 0.9$ circle, $R = 0.63$.

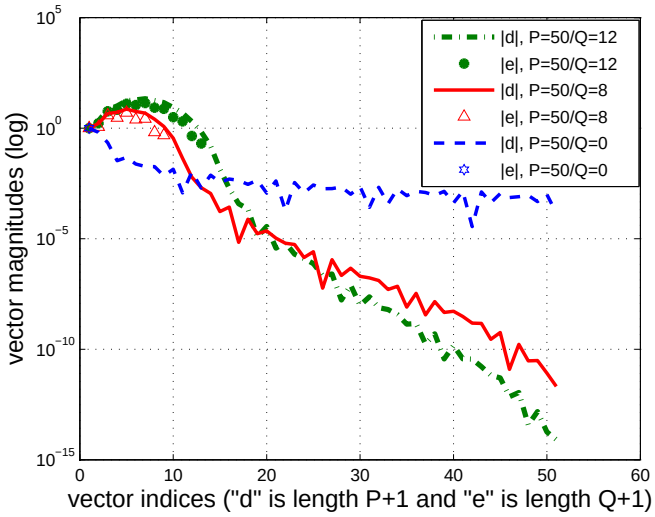

Figure 3.5: Pade coefficient magnitudes of different LDTBC approximations, $R = 0.63$. $\underline{d}$ and $\underline{e}$ are respective vectors of numerator and denominator coefficients of the corresponding approximation in each case.

order terms in vector $\underline{d}$ against higher order terms in it is much more significant for approximations with higher Q. In other words to realize a given accuracy, a smaller P is needed with $Q = 12$ than with $Q = 8$, which will result in a smaller convolution in boundary terms. More simulation results for different P/Q pairs are shown in section 3.5.

Transforming from $\nu(z)$ in (3.24) back to the spatial domain through inverse $\mathcal{Z}$-transform, the boundary value at arbitrary range index m is determined in terms of already computed boundary values (convolution of length $P + 1$) and values on the uppermost computation layer (convolution of length $Q + 2$). Inverse $\mathcal{Z}$-transform of (3.24) gives the boundary value at arbitrary discrete range $m\Delta t$, $m = 1, 2, ..., M = \frac{t}{\Delta t}$, as:

$$\psi_J^m = -\frac{1}{d_0}\left[\sum_{u=1}^{P} d_u \psi_J^{m-u} + \sum_{v=0}^{Q+1} g_v \psi_{J-1}^{m-v}\right]. \tag{3.25}$$

The matrix representation of (3.2) with an absorbing boundary at the top and PEC boundary at the bottom will be of the form

$$\mathbf{S}\underline{\psi}^{m+1} = \mathbf{T}\underline{\psi}^{m} + i\underline{W}^{m}, \tag{3.26}$$

where

$$\mathbf{S} = \begin{bmatrix} R+2i & -i & 0 & . & . \\ -i & R+2i & -i & 0 & . \\ 0 & -i & R+2i & -i & 0 \\ . & . & . & . & . \\ . & . & 0 & -i & s_c \end{bmatrix}, \tag{3.27}$$

$$\mathbf{T} = \begin{bmatrix} R-2i & i & 0 & . & . \\ i & R-2i & i & 0 & . \\ 0 & i & R-2i & i & 0 \\ . & . & . & . & . \\ . & . & 0 & i & t_c \end{bmatrix}, \tag{3.28}$$

$$s_c = R + 2i + i\frac{g_0}{d_0}, \tag{3.29}$$

$$t_c = R - 2i - i\frac{g_1}{d_0}, \tag{3.30}$$

and for $j = 1, 2, .., J-1$, $Q > 0$,

$$W_j^m = \delta_j^{J-1} \left[\sum_{u=0}^{P-1} \left(\delta_0^u - \frac{d_{u+1}}{d_o} \right) \psi_J^{m-u} - \sum_{v=2}^{Q+1} \frac{g_v}{d_o} \psi_{J-1}^{m-v+1} \right]. \tag{3.31}$$

The unconditional stability of Crank-Nicolson scheme in (3.2) is well known [60]. However, when the exact transfer function (3.22) is approximated as in (3.24), the scheme is not unconditionally stable anymore and it may not be trivial to derive a stability condition for a given geometry and discretization. Instead we study the reduced geometry depicted in Figure 3.6, i.e. for a 3 layer problem–the top layer being absorbing boundary, the mid-layer being the computation domain and the bottom layer being the PEC. Although we do not prove that stability of this reduced geometry leads to stability of the larger domain in Figure 3.1, it still provides a stability check since the instability comes only from associated approximate boundary conditions. The excitation we use in this case is a point source of magnitude A, located in the

middle layer, i.e. at $j = J - 1 = 1$. Since an impulse source in spatial domain will have components in all angular spectra, such an excitation is a worst-case test for the narrow-angle PE. For this small geometry in Figure 3.6, (3.2) reduces to:

$$(R + 2i)\psi_1^{m+1} - i\psi_2^{m+1} = (R - 2i)\psi_1^m + i\psi_2^m, \tag{3.32}$$

where $\psi_0^m = 0, m = 0, 1, ..$ is enforced by the PEC bottom layer. Recalling $\psi_1^0 = A$, the z-domain version of (3.32) becomes

$$\begin{aligned}(R + 2i)z^{-1}U_1(z) - A(R + 2i)z^{-1} - iz^{-1}\tfrac{U_1(z)}{\nu(z)} \\ = (R - 2i)U_1(z) + i\tfrac{U_1(z)}{\nu(z)},\end{aligned} \tag{3.33}$$

where $U_j(z) = \mathcal{Z}\{\psi_j^n\}$, $j = 1, 2$ and $\nu(z) = \frac{U_1(z)}{U_2(z)}$. Furthermore, substitution of (3.24) for $\nu(z)$ gives

$$U_1(z) = A\sum_{l=0}^{P} \frac{r_l}{z - z_l}, \tag{3.34}$$

r_l being residues and z_l poles of the function. Equation (3.34) is true if $P > Q$. This is always the case here, because P/Q pairs were obtained through truncating a very long convolution by P terms and padding new terms to a length-2 convolution (revisit Figure 3.3). Transforming (3.34) back to spatial domain gives

$$\psi_1^m = \mathcal{Z}^{-1}\{U_1(z)\} = A\sum_{l=0}^{P} r_l z_l^{-m-1}. \tag{3.35}$$

It is sufficient for the poles z_l of the system to all lie outside the unit circle for stability (or each $1/z_l$ should lie inside the unit circle). Figure 3.7 depicts two cases, where the approximation is stable in one case and unstable in the other.

One point to emphasize about this stability analysis is that it may not always be trivial to find a stable P/Q pair for every discretization Δx and Δt, especially if P and Q are desired to be significantly large.

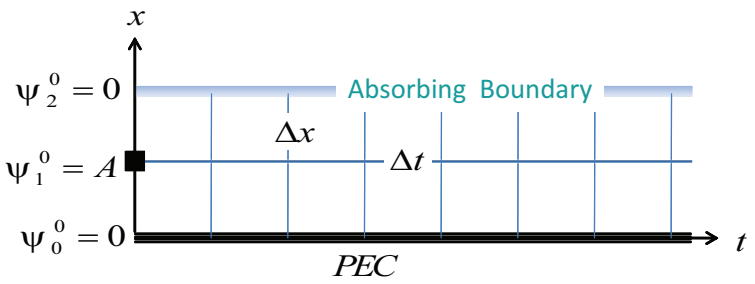

Figure 3.6: Reduced geometry to study the approximation stability

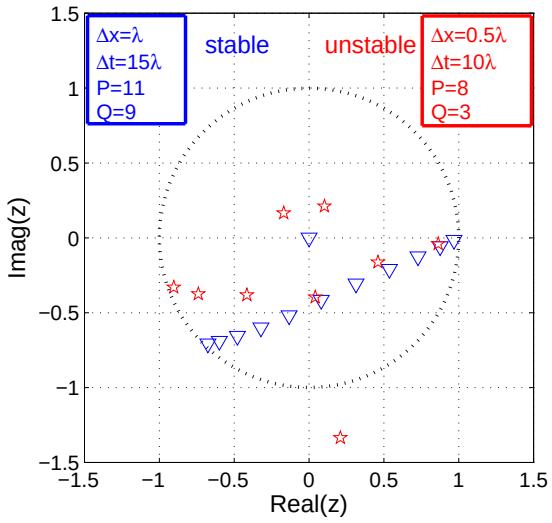

Figure 3.7: Inverse pole locations $\frac{1}{z_l}$ for reduced-domain LDTBC solutions on z-domain, $l = 0, 1, .., P$. Stars are for the unstable case and inverted triangles are for the stable case.

3.4 Approximation by Partial Fractions: LDTBC$_2$

LDTBC formulated above introduces tolerable inaccuracy while avoiding a convolution involving all boundary values. However, the numerical results for quite long ranges will show that a large order P/Q pair will have to be used in LDTBC approximation. The immediate question of how easy is it to find a stable P/Q pair for moderate orders comes up. Moreover, such a stable LDTBC approximation still requires two convolutions at each march-in range, i.e. one on boundary layer values of order $P+1$ and another of order $Q+2$ on one layer below the boundary. This may be undesirable.

We give a second approximation to the exact and modified transfer functions in (3.21), which is still in the form of a Padé approximant, but of order $[L/(L+1)]$. Although a similar approach was suggested in [2], our approach includes a strategy to avoid instabilities, thus is practical. This approach corresponds to approximation by partial fractions with $L+1$ simple poles in the z-domain, assuming they all lie outside the unit circle (to assure stability). The polynomial corresponding to the spatial boundary layer convolution in (3.22) is approximated as:

$$f(z) \approx -\sum_{v=0}^{V-1} \gamma_v z^V - z^Y \sum_{l=0}^{L} \frac{b_l}{z-h_l}. \tag{3.36}$$

Namely, the approximation is:

$$\sum_{v=0}^{m-V} \gamma_{v+V} z^v \approx \sum_{v=0}^{m-V} \widetilde{\gamma}_{v+V} z^v = \sum_{l=0}^{L} \frac{b_l}{z-h_l}. \tag{3.37}$$

We retain the original coefficients for the first V terms so that

$$\widetilde{\gamma}_v = \begin{cases} \gamma_v & , \quad v = 0, 1, ..., V-1 \\ -\sum_{l=0}^{L} \frac{b_l}{h_l^{-V+v+1}} & , \quad v \geq V \end{cases} , \tag{3.38}$$

with $V \geq 1$ and $|h_l| > 1$, $l = 0, 1, .., L$. The standard Padé approximant that gives unique set of h_l's involves a $(L+1) \times (L+1)$ linear system to solve [5] and b_l's are determined by back-substitution; thus $\widetilde{\gamma}_v = \gamma_v$ is satisfied for $v = 0, 1, .., 2L + V + 1$. The higher order approximate coefficients given by (3.38) are desired to mimic exact γ_v at as many points as possible, and the quality of the approximation at orders higher than $2L + V + 1$ will be the deciding factor for choosing L. A scheme with very large L is however prone to instabilities due to numerical roundoff. The stability condition of this approximation is directly given by the system pole locations, i.e. $|h_l| > 1$ is necessary for stability. However the original function will have branch point singularities at $|z| = 1$ as already demonstrated in Figure 3.2, this implies that the approximation could be marginally stable at best. Any LDTBC$_2$ solution that turns out to be unstable is expected to possess almost all of its poles in the vicinity of the unit circle but some just inside. In other words, when approximate $f(z)$ is expanded by $L+1$ partial fractions, all or most of the poles of the solution are outside the unit circle, while the rest of the poles are very close to and inside the unit circle if any.

Practical calculations reveal that the LDTBC$_2$ approximation with more than 30-to-40 simple poles (depending on R) turn out to be unstable. Approximation with fewer poles on the other hand cannot ensure the approximate coefficients in (3.38) to mimic high order exact coefficients. Such an approximation results in inaccuracy in long-range simulations. For instance, LDTBC$_2$ approximation of order $L > 100$ is necessary for $\widetilde{\gamma}_v$ to accurately mimic γ_v in (3.38), $v = 0, 1, .., 2000$ for the given $R = 0.63$. The poles of the LDTBC$_2$ approximation that are inside the unit circle for

this case are depicted in Figure 3.8. Furthermore, given an unstable LDTBC_2 approximation with given number of poles and an R parameter, LDTBC_2 approximation with more poles for the same R is also another unstable approximation. Hence appropriate pole location modifications are necessary for the sake of stability. Because the poles making the approximation unstable are close to the unit circle, inverting their magnitudes, while their arguments kept unchanged, results in a new stable approximation with undetermined residues. The way to set new residues for the "re-located" poles relies on enforcing continuity of the exact transfer function and its derivatives at $z = 0$, up to the order to give a linear system to uniquely determine these new residues. We summarize this stabilization scheme for LDTBC_2 as:

- LDTBC_2 with $L + 1$ partial fractions (Padé approximation of order $[L/L + 1]$) is applied to approximate the exact solution, B of the simple poles lying inside the unit circle.

- If $B \neq 0$, meaning the approximation is unstable, the poles inside are pushed out of the unit circle through $\widetilde{h_k} = \frac{h_k}{|h_k|^2}$, $k = 0, 1, .., B - 1$. Note here that h_k and $\widetilde{h_k}$ are reordered for convenience.

- $f^{(y)}(0) = \frac{d^y}{dz^y}\left[\sum_{l=0}^{L-B} \frac{b_l}{z-h_l} + \sum_{k=1}^{B} \frac{\widetilde{b_k}}{z-\widetilde{h_k}}\right]_{z=0}$ is enforced for $y = 0, 1, .., B - 1$ giving unique solution of new residues $\widetilde{b_k}$ corresponding to re-located poles $\widetilde{h_k}$. Here h_l are also reordered.

Although the two are in the same rational form, LDTBC_2, providing recursive computation, is superior to LDTBC. Namely there will not be a whole new boundary layer convolution at each march-in range. Instead, the history on the boundary layer will be cumulative, thus could be recursively computed by adding a new term after each march-in range. The approximation in (3.37) translates in the spatial domain as:

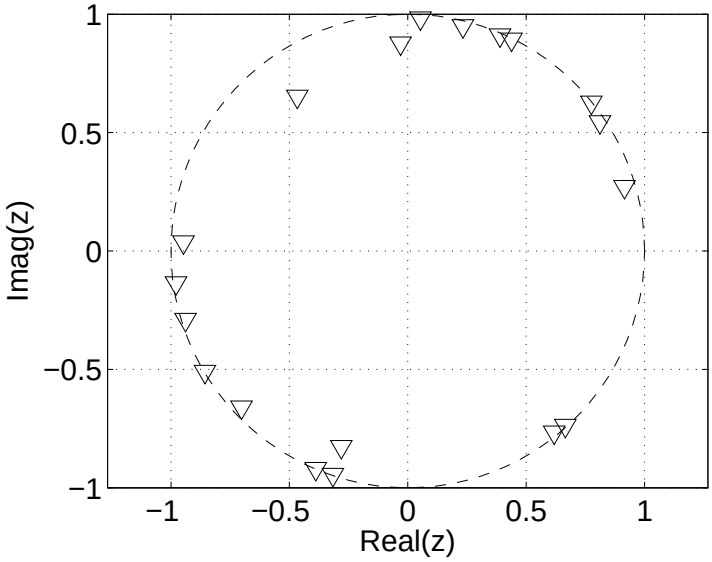

Figure 3.8: The poles of LDTBC_2 approximate solution lying inside unit circle in the case of $L = 100$, $V = 0$ and $R = 0.63$

$$\sum_{v=0}^{m} \gamma_v \psi_J^{m-v} \approx \sum_{v=0}^{V-1} \gamma_v \psi_J^{m-v} + \sum_{l=0}^{L} D_l(m-V), \tag{3.39}$$

where

$$D_l(s) = \begin{cases} \frac{b_l}{h_l}\psi_J^s + \frac{1}{h_l} D_l(s-1) & , s > 0 \\ 0 & , s \leq 0 \end{cases}. \tag{3.40}$$

The convolution of order V in (3.39) is to be computed at each range step; on the other hand D_l are updated at each step recursively, that results in the boundary layer value at discrete range m:

$$\psi_J^m = -\frac{1}{\gamma_0}\left[\sum_{v=1}^{V-1} \gamma_v \psi_J^{m-v} + \sum_{l=0}^{L} D_l(m-V) + \psi_{J-1}^m + \psi_{J-1}^{m-1}\right]. \tag{3.41}$$

The reason for keeping the first V-term convolution and not associating it in the approximation is revealed in the nature of γ_v coefficients for small v. The low order terms of the Legendre polynomials with specific arguments make the first few coefficients very large compared with higher order coefficients [2]. This is why the first V $\widetilde{\gamma}_v$ are set to be equal to γ_v. This makes the dynamic range of the coefficients that rational approximation is enforced on smaller, resulting in a more accurate approximation for orders higher than $2L + V + 1$. The fact that the first few coefficients are very large compared with higher order coefficients is depicted in Figure 3.5, where $\underline{d}$ reduces to $\underline{\gamma}$ in the case of simple convolution truncation ($Q = 0$ case). Choice of $V = 2$ will improve the coefficient approximation to an extent where it cannot be pushed further, due to the fact that γ_0 and γ_1 are those big coefficients making the dynamic range of coefficient magnitudes huge. The dynamic range of $\underline{\gamma}$ in Figure 3.5 ($|\underline{d}|$ in blue) will be more severe for smaller R, thus makes the need to shift the approximation termination by V terms inevitable. Therefore, for the sample simulations in the next section we keep $V = 2$.

3.5 Numerical Results

Numerical results for the Crank-Nicolson FD scheme outlined above for LDTBC and LDTBC$_2$ as well as the PML are compared in this section. There will be two sets of results. The first set of results will demonstrate the comparison of DTBC, LDTBC, LDTBC$_2$ and the PML with an analytical solution for a fixed geometry. The second set of results will be used for the performance comparison of PML and LDTBC$_2$ for long-range simulations where LDTBC suffers from lack of instability issues and DTBC suffers from the computation time. For all results, the model geometry is the half-open free-space truncated at elevation x_h above the PEC at $x = 0$. The source function $s(x)$ is always excited at $t = 0$.

As mentioned previously, the initial domain truncation enforces $\psi_j^0 = 0$, $j \geq J-2$ where the absorbing boundary is placed at Jth layer. We generate a Gaussian source with a standard deviation σ_t and centered at height x_t. Since the above enforcement dictates the source field to be identical to 0 at $x = 0$ and $x = x_h$, we consider the Gaussian beam to be expressed as an infinite sum of eigenfunctions of the parallel-plate waveguide with PEC walls at $x = 0$ and $x = x_h$. The approximate Gaussian function is obtained by retaining only the first K number of eigenfunctions:

$$\psi(x, t = 0) =: s(x) = A \sum_{m=1}^{K} \sin \frac{m\pi x_t}{x_h} \sin \frac{m\pi x}{x_h} e^{-m^2\pi^2\sigma_t^2/2x_h^2}, \quad 0 \leq x \leq x_h. \quad (3.42)$$

The standard deviation σ_t is chosen so that the effective beam-width remains well within the PE approximation. The solution of the standard PE in (3.1) at a range t for the excitation in (3.42) and a PEC boundary at $x = 0$ could be shown to be (see Appendix A):

$$\begin{aligned} \psi(x,t) &= -A\sqrt{\frac{i}{8}} \sum_{m=1}^{K} \sin \frac{m\pi x_t}{x_h} e^{-i\frac{m^2\pi^2 t}{2k_o x_h^2}} e^{-\frac{m^2\pi^2\sigma_t^2}{2x_h^2}} \times \\ &\quad \times \left\{ e^{i\frac{m\pi x}{x_h}} \left[\mathcal{F}\left(\sqrt{\frac{k_o x_h^2}{\pi t}} + \beta_- \right) + \mathcal{F}\left(\sqrt{\frac{k_o x_h^2}{\pi t}} - \beta_- \right) \right] \right. \\ &\quad \left. - e^{-i\frac{m\pi x}{x_h}} \left[\mathcal{F}\left(\sqrt{\frac{k_o x_h^2}{\pi t}} + \beta_+ \right) + \mathcal{F}\left(\sqrt{\frac{k_o x_h^2}{\pi t}} - \beta_+ \right) \right] \right\}, \end{aligned} \quad (3.43)$$

where $\mathcal{F}(x) = \int_0^x e^{i\frac{\pi}{2}u^2} du$ is the Fresnel Integral [1] and

$$\beta_\pm = \frac{1}{\sqrt{\pi}} \left(\sqrt{\frac{k_o x^2}{t}} \pm \sqrt{\frac{t m^2 \pi^2}{k_o x_h^2}} \right). \quad (3.44)$$

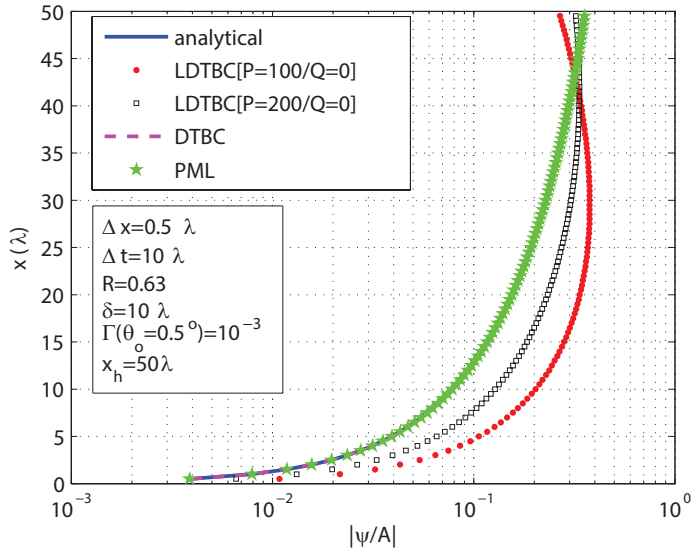

Figure 3.9: Field magnitudes normalized by the excitation ($|\psi/A|$) for the first problem set (DTBC, LDTBC and PML). The range is $t = 10,000\lambda$, with $\sigma_t = 1\lambda$, $x_t = x_h/2 = 25\lambda$ and $K = 400$ for the excitation. The dashed DTBC solution curve is indistinguishable from the solid analytical solution curve.

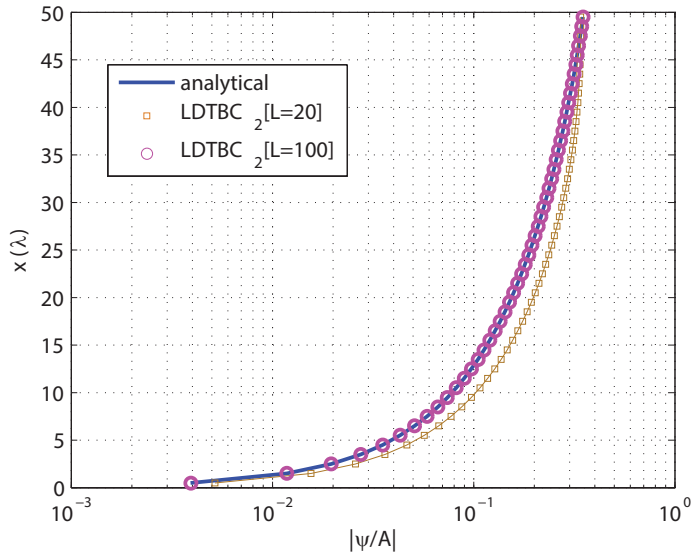

Figure 3.10: Field magnitudes normalized by the excitation ($|\psi/A|$) for the first problem set (LDTBC_2). Simulation parameters are the same as in Figure 3.9.

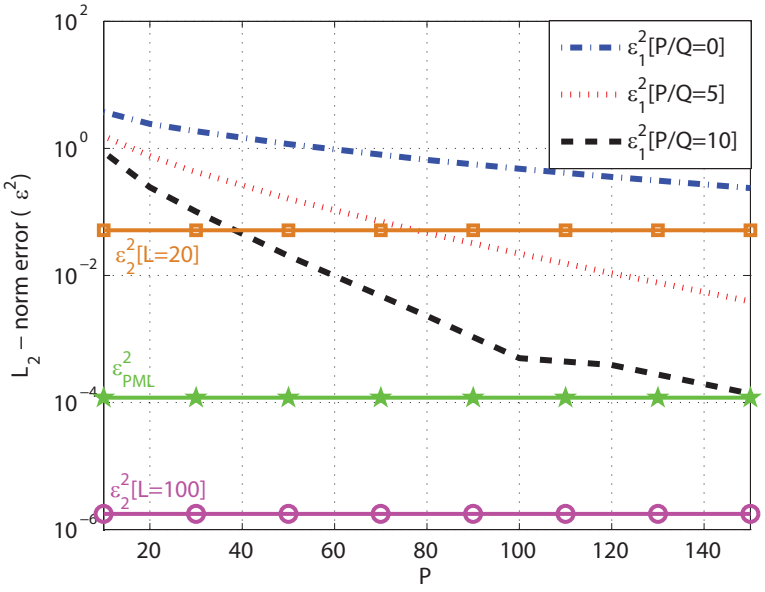

Figure 3.11: L_2-norm errors corresponding to the solutions in Figures 3.9 and 3.10. The dashed curves show LDTBC errors for varying P. Straight solid lines with squares, pentagrams and circles denote error levels for PML and LDTBC_2.

Note that there is no PEC boundary at $x = x_h$ for $t > 0$. The model geometry (half-open 2-D free space) is truncated at $x_h = 50\lambda$ above the ground plane for the first set of results. This deliberate choice of a short geometry helps simulate far-range solutions quickly, while each excited mode in (3.42) is assured to experience lot of reflections from both boundaries before arriving at the observation range. The standard deviation of the excitation in (3.42) is set as $\sigma_t = 1\lambda$, which results in half power points of approximately $\pm 7.5^o$ around the paraxial axis [37]. The observation is at $10,000\lambda$ range.

Figure 3.9 depicts solutions of the first problem. The exact DTBC solution (dashed) and the PML solution (pentagrams) are obviously very accurate, they match the analytical solution (solid curve) at every elevation of the model geometry. The two approximations, i.e. inaccurate LDTBC solutions are selected on purpose, just to demonstrate that LDTBC approximation is indeed severe and useless if $Q = 0$. In that case it is just truncation of the boundary layer convolution in Figure 3.3 by P nodes. We choose an L_2-norm error definition to quantify the magnitude of inaccuracies:

$$\epsilon^2 = \frac{\sum\limits_j |\psi_j^{soln} - \psi_j^{analy}|^2}{\sum\limits_j |\psi_j^{analy}|^2}, \tag{3.45}$$

where at discrete altitude j, ψ_j^{analy} is the analytical field solution and ψ_j^{soln} is the numerical field solution computed (could be one of PML, DTBC, LDTBC or LDTBC_2). Because it avoids the exponential convolution cost to a linear cost through recursive computation, LDTBC_2 offers for a fast and accurate approximate solution as it is depicted in Figure 3.10. The LDTBC_2 approximation with 21 poles (brown squares) for given discretization and range is not as accurate; on the other hand the approximation with 101 poles (purple circles) was not stable originally. However, with the

stabilization strategy given in Section 3.4, LDTBC$_2$ with 101 simple poles becomes stable and accurate as shown in Figure 3.10. It accurately mimics the analytical solution while being efficient in CPU time. The errors are depicted in Figure 3.11, where the three dashed curves show the L_2-norm errors for LDTBC approximations with different Q. The horizontal axis is P varying from 10 to 150, and the three errors expectedly decay with increasing P. One thing to recall is that LDTBC is not necessarily stable for a given P/Q pair, therefore while generating the dashed curves, 10 stable P/Q pairs for each Q are first selected based on the 3-layer model discussed in 3.3, then the curves are formed by linear interpolation of errors defined in (3.45). These errors are denoted as ϵ_1^2. The errors produced by the LDTBC$_2$ solutions are shown in Figure 3.11 with respective color curves, denoted as ϵ_2^2. These curves denote nothing but the error level for the respective approximations in Figure 3.10, thus they are independent of P.

The quantity ϵ_{PML}^2 in Figure 3.11 denotes the error level for the PML solution (green pentagrams) for which the solution was depicted in Figure 3.9. At this range, PML results are always accurate and robust. Having control over δ, Γ and hence over σ_o, excellent absorption could be achieved with PML even though a significant spectrum of the excitation contains low grazing angle waves. Another factor in favor of PML over DTBC and thus over LDTBC for long ranges is the computational effort, where the convolution in (3.25) is avoided altogether. To achieve the very low error level of ϵ_{PML}^2 in Figure 3.11, a LDTBC approximation of order $P = 150/Q = 10$ would be needed, which is neither as accurate nor as fast at this range even if stable. Thus it is clear that PML and LDTBC$_2$ are the two efficient and accurate numerical solutions for domain truncation at moderate ranges.

Because the grazing angle content becomes very narrow for longer ranges, the large ratio between observation range and domain height can render the PML solution inaccurate, i.e. PML would fail to absorb dominant propagating ray [46]. The second

set of simulation results will depict such a more realistic case, where the domain sizes will be expressed in metric units and are larger along both altitude and range. The Gaussian source (3.42) will reside at $x_t = 10$ m, the source width is $\sigma_t = 30$ cm and the operating frequency is 1 GHz. Two different cases are depicted in Figure 3.12. The dashed curves are solutions at 50 km range for a 100 m domain truncation and the solid curves are solutions at 20 km range for 50 m domain truncation and both are cases of far-range and high-domain simulations for which the LDTBC approximation seemed to fail. For this reason only PML and LDTBC_2 are subject to comparison with respective L_2-norm errors as marked in the figure. Although both are perfectly absorbing at moderate and small ranges, LDTBC_2 generally produces a smaller error than PML does at far ranges. This is mainly due to the fact that PML cannot be pushed further, i.e. using a thicker matching layer or setting an extremely small reference reflection Γ does not help beyond a certain limit. Indeed, the PML parameters used in Figure 3.12 are the limits for this case which do not improve further. The parameter L on the other hand determines the order and the accuracy of LDTBC_2, thus could be set to reasonably large values to simulate accurate absorption. However, there is also a limit to L, thus there is a range-to-height ratio limit to accurate absorbing LDTBC_2 solutions. This limit will be discussed later.

Figure 3.13 in this regard analyzes the effect of observation range and domain height with respect to the error. The range that PML or LDTBC_2 with fixed parameters start to fail at is closer when $x_h = 50$ m than when $x_h = 100$ m. This is obvious since each undesired boundary reflection adds inaccuracy to the solution, making smaller altitude boundary problems harder to simulate at far ranges. The error comparison is held up to a range where the L_2-norm errors become comparable to 1 (which is huge in this case). The LDTBC_2 error, i.e. ϵ_2^2 in Figure 3.13 is always smaller than its PML counterpart ϵ_{PML}^2. Therefore LDTBC_2 with 151 simple poles for our case is clearly more accurate than any PML solution at far ranges. Is

it possible then to improve it further by setting a bigger L? As indicated before, there also is a certain limit to how big L would be chosen. Firstly, solving for the residues b_l and poles h_l in (3.40) involves inverting a $(L+1) \times (L+1)$ full-matrix. Moreover this matrix to be inverted contains the derivatives of the transfer function $f^{(y)}(z=0)$, $y = V, V+1, .., 2L+V$. Therefore depending on the nature of the transfer function $f(z)$ or of its exact Taylor coefficients $\underline{\gamma}$, this matrix could turn out to be ill-conditioned. Practical simulations for problems of our interest show that the condition number ρ of this matrix becomes extremely large if $L > 200$ and MATLAB cannot handle such ill-conditioned matrices. That is why our choices of L in above results represents approximation orders close to the practical limit.

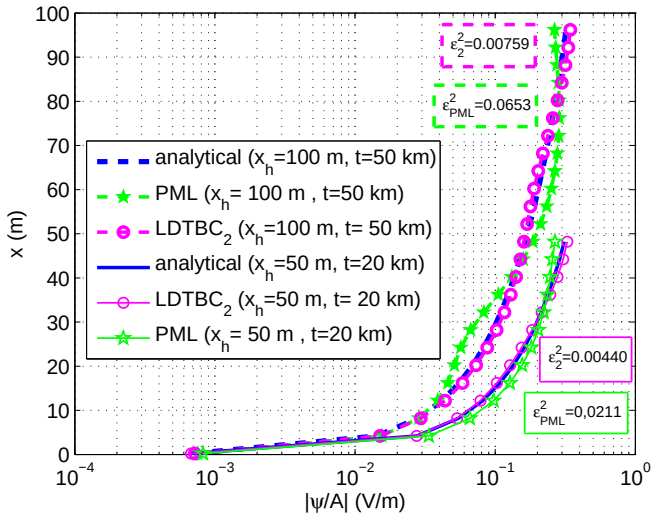

Figure 3.12: Field magnitudes (V/m) for two different problems. The solid curves are solutions at $t = 20km$ range for a $x_h = 50m$ domain and dashed lines at $t = 50km$ range for $x_h = 100m$. The simulation parameters are $\Delta x = 20cm$, $\Delta t = 5m$, $x_t = 10m$, $\sigma_t = 30cm$, $\delta = 3m$, $L = 150$.

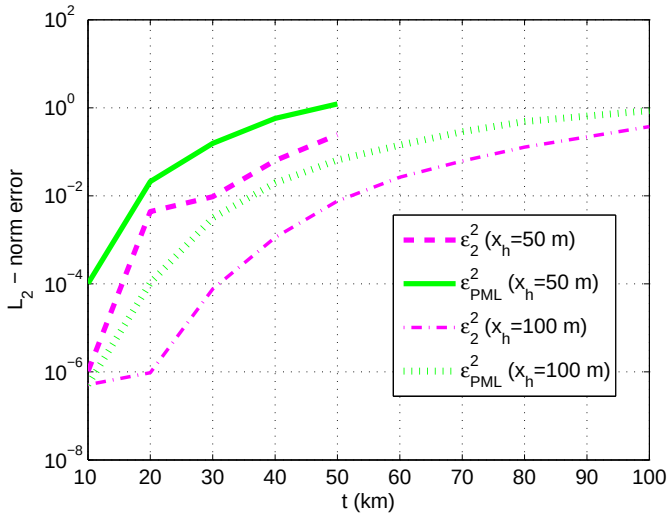

Figure 3.13: L_2-norm errors ϵ^2. All parameters are the same as in Figure 3.12.

3.6 CPU Time Comparison

Finally, Figure 3.14 shows the CPU time for DTBC and LDTBC$_2$ convolutions with increasing range. Computing a whole new convolution of all the boundary layer values at each march-in range, exact DTBC solution has quadratic dependency on time for increasing order, whereas recursive computation in LDTBC$_2$ solution is linearly dependent on range. This comparison between DTBC and LDTBC$_2$ depicted in Figure 3.14 is only for the boundary computation, i.e. the CPU time comparison does not consider time for matrix multiplication operations, which is not as costly as the convolutions incurred in DTBC performed at far ranges. Since PML is totally local, i.e. does not employ a boundary layer convolution, there really is no significant added cost to implement it even though the matching layer enlarges the computation domain height by δ. Therefore, we can surely say that PML is the fastest in CPU time among all techniques discussed here.

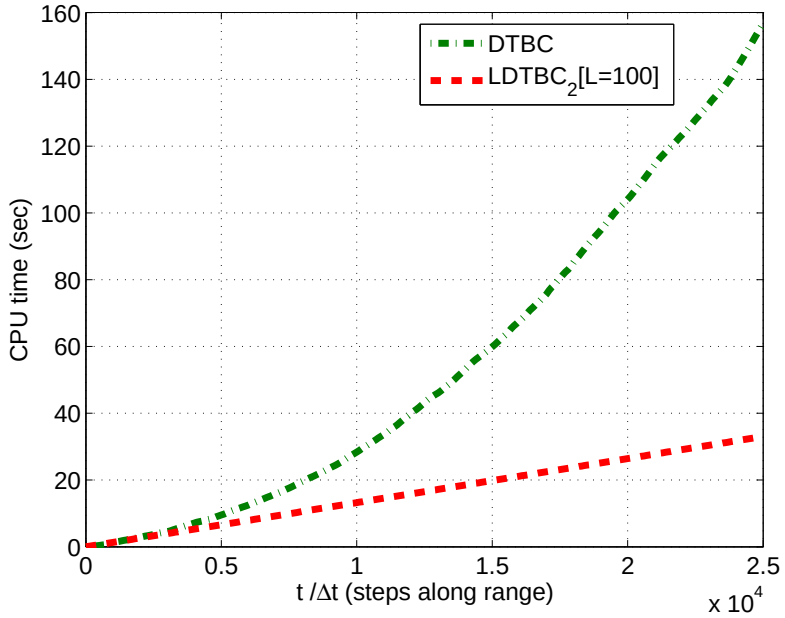

Figure 3.14: CPU time taken by the boundary computation (convolution in DTBC case).

CHAPTER 4

SPARSE GRID COLLOCATION METHODS

In this chapter we present the Sparse Grid Collocation (SGC) method and its adaptive variations that are used for multi-dimensional interpolation/quadrature for quantifying uncertainty in electromagnetic propagation and scattering phenomena. These methods are based on extension of the Smolyak's formula [79] to multi-dimensional function interpolation, and our notation is based on [95], [94]. First the construction of the sparse grid is presented. Afterwards, two recently developed algorithms we use are given. These algorithms are used for adaptive construction of the original sparse grid, where we make certain modifications depending on the benefit in applying to the problems of our interest. The two methods presented in this chapter will constitute methods of uncertainty quantification that we compare to Monte Carlo sampling, and will be demonstrated with the wave propagation examples of next chapter.

4.1 Construction of the Non-Adaptive Sparse Grid

Consider the following system

$$\begin{array}{l} \mathcal{L}(w,r;f) = h(w,r) \quad , \quad r \in D \\ \mathcal{B}(w,r;f) = h_b(w,r) \quad , \quad r \in \partial D \end{array} , \tag{4.1}$$

where $\mathcal{L}$ may be a differential or an integral operator defined in space D, and $\mathcal{B}$ is an operator defined on ∂D, the boundary of the space, $h(y,r)$ is a source function

with both deterministic and random arguments, and $h_b(y,r)$ is a boundary condition. The domain D in general may include both space and time variables and $r = (x_1, x_2, ..., x_T)$, T being the dimensionality of the vector of independent deterministic variables present in D. The quantity f is the solution sought to (4.1). The randomness in (4.1) comes from variable $w \in \Omega$, where in the most general sense Ω is the probabilistic event space. For (4.1) to be numerically solvable it is necessary to reduce infinite dimensional Ω to a finite dimensional space of random events, and we assume that this is already satisfied, $y(w) = (Y_1(w), Y_2(w), ..., Y_N(w))$ are the independent continuous RVs representing all randomness in (4.1). If random variables Y_i have probability density functions (pdf) $\rho_i : \Gamma_i \to \mathbb{R}^+$, where $\Gamma_i \equiv Y_i(\Omega)$ are the supports, $i = 1, 2, .., N$; then the joint pdf is $\rho(y) = \prod_{i=1}^{N} \rho_i(Y_i)$ and the joint support is $\Gamma = \prod_{i=1}^{N} \Gamma_i \subset \mathbb{R}^N$. With above decomposition, system (4.1) can be written in the following form:

$$\begin{aligned} \mathcal{L}(y, r; f) &= h(y, r) \quad , \quad (y, r) \in \Gamma \times D \\ \mathcal{B}(y, r; f) &= h_b(y, r) \quad , \quad (y, r) \in \Gamma \times \partial D \end{aligned} \quad . \tag{4.2}$$

In order to not deviate the interest of the reader, it is important to stress that what we ultimately seek is to find the moments of $f(r, y)$ in (4.2) starting with the mean value. Therefore, for one to evaluate $\mathrm{E}[f]$, the mean of f, the problem indeed reduces to a $N-$dimensional integral. Monte Carlo (MC) sampling is the simplest and widely used way of computing $\mathrm{E}[f]$.

The SGC method is based on efficient computation of multi-dimensional integrals on Smolyak's sparse grids [79], [64]. The sparse grid algorithm basically is the construction of a set of nodes from the sample space of the N-dimensional Γ such that desired accuracy in the function interpolation is achieved with less number of points than the brute-force MC sampling. Once the function interpolation is achieved, the

mean value integration is just a matter of integration of the basis functions employed in the random space.

Before going into details of how the sparse grid is constructed, it is necessary to discern how it differs from MC. Suppose one is interested in solving for the mean of $f(r, y)$ in (4.2), and for the sampling based estimators $\mathcal{L}$ and $\mathcal{B}$ do not matter at all, they are just operators that $f(r, y)$ is the solution of in $\Gamma \times D$, including the boundary ∂D. Since the mean-value integration is evaluated on random variables y in Γ, there is no need to keep writing r in the equations. Therefore we drop r and switch to a new function $f(y)$, where y is still the $N-$variate random variable defined above, and the mean of f is computed by sampling y many times as the ensemble average converges to the exact mean $\widetilde{f}$. Note that the exact mean of the function and its approximation are

$$\begin{aligned} \widetilde{f} &:= \int_{\Gamma} f(y)\rho(y)dy \\ &= \int_{Y_1} .. \int_{Y_N} f(Y_1, .., Y_N)\rho_1(Y_1)..\rho_N(Y_N)dY_N..dY_1 \\ &\approx \sum_{q=1}^{Q} f(y_q)\alpha_q, \end{aligned} \tag{4.3}$$

where $\Gamma \subset \mathbb{R}^N$, Q is the number of realizations of the random variable $y = (Y_1, Y_2, .., Y_N)$, i.e. number of samples used in approximating the mean-value integral. Note that the mean is a function of temporal-spatial variables r only. α_q are the weights corresponding for each realization y_q, $q = 1, 2, .., Q$. If one uses MC sampling, then y_q are drawn totally uniformly in $\Gamma = \Gamma_1 \times \Gamma_2 \times .. \times \Gamma_N$ and $\alpha_q = \frac{1}{Q}$, thus making each sample equally weighted. Despite the dimension-independence property of the simple MC sampling, for functions with smooth variation in their supports more clever sampling based techniques have been devised for up to moderate dimensions N. The

SGC method, which is what we will consider next, solely interpolates the function at appropriate nodes y_q and computes the appropriate α_q, q =1,2,..,Q, while decreasing the sample size Q for a given accuracy in interpolating f.

Suppose that $\mathcal{U}^i$ is a 1-dimensional interpolation rule along $\Gamma_i \subset \mathbb{R}$, i.e.

$$\mathcal{U}^i(f) := \sum_{k=1}^{q_i} f(Y_k^i)\zeta_k^i(Y), \tag{4.4}$$

q_i is the interpolant size along the i^{th} dimension along Γ_i, $i = 1, 2, .., N$. The set of nodes in Γ_i is defined as $\Theta^i = \{Y_k^i \mid Y_k^i \epsilon [0,1], k = 1, 2, .., q_i.\}$. $\zeta_k^i(Y)$ is a member function from the interpolation basis set, choice of which will be mentioned shortly. The 1-dimensional support is assumed to be the unity range, $Y \in [0, 1]$, whereas one can pass to any finite support interpolation once the interpolation in [0,1] is known. In cases where the dimensionality is low, e.g. $N \leq 4$, the first obvious set of points for constructing the N-dimensional grid is to sample from tensor product of 1-dimensional interpolation rules, i.e. from $\mathcal{U}^{i_1} \otimes \mathcal{U}^{i_2} \otimes .. \otimes \mathcal{U}^{i_N}$, where $\otimes$ is the tensor product symbol. It is apparent that the sample size $Q = \prod_{i=1}^{N} q_i$ for the tensor product, and one easily realizes it will grow rapidly for large N.

The sparse grid interpolation for the $N-$dimensional function f is constructed on the Smolyak sparse grid as [64]

$$\begin{aligned} f &\approx \mathcal{A}_{(N,d)}(f) \\ &:= \sum_{|\mathbf{i}|_1 \leq N+d} (-1)^{N+d-|\mathbf{i}|_1} . \binom{N-1}{N+d-|\mathbf{i}|_1} \left(\mathcal{U}^{i_1} \otimes .. \otimes \mathcal{U}^{i_N}\right)(f) \\ &= \sum_{|\mathbf{i}|_1 \leq N+d} \Delta^{i_1} \otimes .. \otimes \Delta^{i_N}(f), \end{aligned} \tag{4.5}$$

where $\mathbf{i} = (i_1, i_2, .., i_N)$, the first norm is $|\mathbf{i}|_1 = \sum_{k=1}^{N} i_k$, $\Delta^k = \mathcal{U}^k - \mathcal{U}^{k-1}$, $k > 1$, and $\Delta^1 = \mathcal{U}^1$. The last equality in (4.5) is not straightforward to see, but is essential in constructing a hierarchical formulation [90], through which we have the control over accuracy improvement from certain level of interpolation of f to the next level. $d \geq 0$ is referred to as the "level" of the Smolyak algorithm [63], with which both Q as well as the accuracy in the approximation increases. $\mathcal{A}_{(N,d)}(f)$ is thus the sparse grid interpolant to f constructed on dth level Smolyak interpolant. The sample set of dth level interpolant (4.5) is thus

$$\mathcal{H}_{(N+d,N)} := \bigcup_{|i|_1 = N+d} \Theta^{i_1} \times \Theta^{i_2} \times ... \times \Theta^{i_N}, \tag{4.6}$$

where $\mathbf{i} = (i_1, i_2, .., i_N)$. In other words, $\mathcal{H}_{(N+d,N)}$ is the set of N-dimensional points that $A_{(N+d,N)}(f)$ samples. If nested sets are used in (4.5), Smolyak's sparse grid construction employs $Q \sim (2N)^d / d!$ samples for $N \gg 1$ [94], which offers great sample size reduction with respect to the N-tensor products. What is meant by a "nested" set is $\Theta^{k+1} \supset \Theta^k$, $k \geq 1$ where Θ^k is the set of nodes used by $\mathcal{U}^k$. Clenshaw-Curtis nodes which sample Y_k^i at the extrema of Chebyshev polynomials [14], and Gauss-Patterson nodes which sample Y_k^i on the Gaussian nodes augmented by Patterson [69] are the two widely used nested sets for sparse grid interpolation. Another set of points is the Newton-Cotes set, i.e. set of equi-distributed nodes. Choice among these is a trade-off between accuracy and sample size Q, the Gauss-Patterson samples more points than the other two node sets at the same level interpolation [25], [50], [85]. Newton-Cotes and Clenshaw-Curtis sets are our only selections in this work, where we will refer to these sets as "equi-distant nodes" and "Chebyshev nodes", respectively. We select as basis polynomials the local triangular functions when equi-distant nodes are employed, but Lagrange characteristic polynomials when Chebyshev nodes are

employed. This is due to Runge's phenomenon associated with Lagrange polynomial interpolation when used with equi-distant nodes [11]. For a uni-dimensional interpolation $\mathcal{U}^i$, the cardinality that we use with both Chebyshev and equi-distant nodes is [94]:

$$q_i = \begin{cases} 2^{i-1}+1 & , \ i > 1, \\ 1 & , \ i = 1. \end{cases} \tag{4.7}$$

As noted before, these nodes are nested, i.e. the q_{i+1} nodes used in $\mathcal{U}^{i+1}$ contain all of the q_i nodes used in $\mathcal{U}^i$. The equi-distant nodes are

$$Y_k^i = \begin{cases} \frac{k-1}{q_i-1} & , k = 1, 2, .., q_i \quad , i > 1, \\ 0.5 & , k = 1 \qquad , i = 1, \end{cases} \tag{4.8}$$

and the corresponding local triangular basis functions are

$$\zeta_k^i(Y) = \begin{cases} 1 - (q_i - 1)\left|Y - Y_k^i\right| & , \text{if} \left|Y - Y_k^i\right| < \frac{1}{q_i - 1}, \\ 0 & , \text{otherwise}, \end{cases} \tag{4.9}$$

and $\zeta_1^1(Y) = 1$, $Y \epsilon [0, 1]$. Similarly, the Chebyshev nodes are

$$Y_k^i = \begin{cases} \frac{1}{2} - \frac{1}{2}\cos\left(\frac{k-1}{q_i-1}\pi\right) & , k = 1, 2, .., q_i \quad , i > 1, \\ 0.5 & , k = 1 \qquad , i = 1, \end{cases} \tag{4.10}$$

and the corresponding Lagrange characteristic polynomial bases are

$$\zeta_k^i(Y) = \begin{cases} \prod\limits_{l=1, l\neq k}^{q_i} \frac{Y - Y_l^i}{Y_k^i - Y_l^i} & , k = 1, 2, .., q_i \quad , i > 1, \\ 1 & , k = 1 \qquad , i = 1, \end{cases} \tag{4.11}$$

with $\zeta_k^i(Y_k^i) = 1$ and $\zeta_k^i(Y_l^i) = 0$ for $l \neq k$.

The Lagrange characteristic polynomials in (4.11) require division/multiplication arithmetic of large numbers if $i \gg 1$. Therefore, we instead use the "barycentric formulation" [11], [32], which is identical to (4.11) but numerically stable for any i:

$$\zeta_k^i(Y) = \begin{cases} \frac{\frac{\nu_k^i}{Y-Y_k^i}}{\sum_{l=1}^{q_i} \frac{\nu_l^i}{Y-Y_l^i}} & , k = 1, 2, .., q_i \quad , i > 1, \\ 1 \qquad\qquad , k = 1 \qquad , i = 1. \end{cases} \tag{4.12}$$

If the barycentric Lagrange interpolation is employed with Chebyshev nodes (which is the only use of it in our case), then the weights ν_k^i are given as [72]:

$$\nu_k^i = (-1)^{q_i - k} \delta_k 2^{q_i - 1} \quad , \; \delta_k = \begin{cases} 1/2 & , k = 1 \text{ or } k = q_i, \\ 1 & , \text{otherwise.} \end{cases} \tag{4.13}$$

Note that the nodes and corresponding basis functions given above have assumed the unity interval $Y \in [0, 1]$. One can map everything to the general case of $Z \in [a, b]$ via the transformation $Z = a + (b - a)Y$.

With above nodes and basis functions, one needs to analytically or numerically integrate tensor products of $\zeta_k^i(Y)$ and pdfs that appear in (4.5) to pass to the moments of f. This is simple, since each of the N dimensions are statistically independent. Detailed discussion of the basis integrations we use throughout this work is given in Appendix B. An alternate formulation to (4.5) is considered next, which will eventually allow adaptive methods to hierarchically construct the sparse grid.

The sparse grid in dth level non-adaptive collocation formula in (4.6) is deterministic in the sense that all nodes in the sparse grid and their corresponding basis tensor products are a-priori known without the knowledge of how smooth f is in Γ. A good adaptivity algorithm is expected to measure importance of f in Γ, thus leading to dense grids in statistically important regions in the next level $(d + 1)$. On the other hand, it is for computational simplicity that a given node included in the sparse

grid at a certain level d is not re-visited in further levels. This is in contrast to (4.5). Therefore, the SC in (4.5) can be manipulated to utilize a hierarchical formulation, as described in [43], where a given node in the sparse grid is passed to the deterministic solver only once:

$$\begin{aligned} \mathcal{A}_{(N+d,N)}(f) &= \mathcal{A}_{(N+d-1,N)}(f) + \Delta\mathcal{A}_{(N+d,N)}(f), \\ \Delta\mathcal{A}_{(N+d,N)}(f) &= \sum_{|\mathbf{i}|=N+d} \sum_{\mathbf{n}\in B_{\mathbf{i}}} \left(\xi_{n_1}^{i_1} \otimes .. \otimes \xi_{n_N}^{i_N}\right) w_{\mathbf{n}}^{\mathbf{i}}, \end{aligned} \tag{4.14}$$

where $w_{\mathbf{n}}^{\mathbf{i}}$ is a surplus, defined for each of the new nodes that are included in the sparse grid at dth level, and indicates the proximity of a certain level interpolation to the exact function value evaluated at the given node:

$$w_{\mathbf{n}}^{\mathbf{i}} = f\left(X_{n_1}^{i_1}, .., X_{n_N}^{i_N}\right) - \mathcal{A}_{(|\mathbf{i}|-1,N)}(f)\left(X_{n_1}^{i_1}, .., X_{n_N}^{i_N}\right). \tag{4.15}$$

The hierarchical multi-index set is defined as

$$\begin{aligned} B_{\mathbf{i}} = \{\mathbf{n} \in \mathbb{N}^N : X_{n_l}^{i_l} \in \Theta_{\Delta}^{i_l} \quad &, \quad n_l = 1, 2, .., q_{i_l}^{\Delta} \\ &, \quad l = 1, 2, .., N\}. \end{aligned} \tag{4.16}$$

We henceforth name $\mathbf{i}$ as the "super-index vector" and $\mathbf{n} = (n_1, n_2, ..., n_N)$ as the "sub-index vector", respectively. The hierarchical set $\Theta_{\Delta}^{i_l} = \Theta^{i_l} \setminus \Theta^{i_l-1}$ indicates the difference in successive level uni-dimensional node sets, and its cardinality is $q_{i_l}^{\Delta} = q_{i_l} - q_{i_{l-1}}$. Therefore, a given pair of basis function $\xi_n^i(Y)$ and uni-dimensional node X_n^i in (4.15) correspond to the original pair $\zeta_k^i(Y)$ and Y_k^i, respectively, except that the indices in (4.15) are renumbered to follow the indexing in set $B_{\mathbf{i}}$. The two index conventions are demonstrated in Figures 4.1, 4.2. Figures 4.1a and 4.1b depict

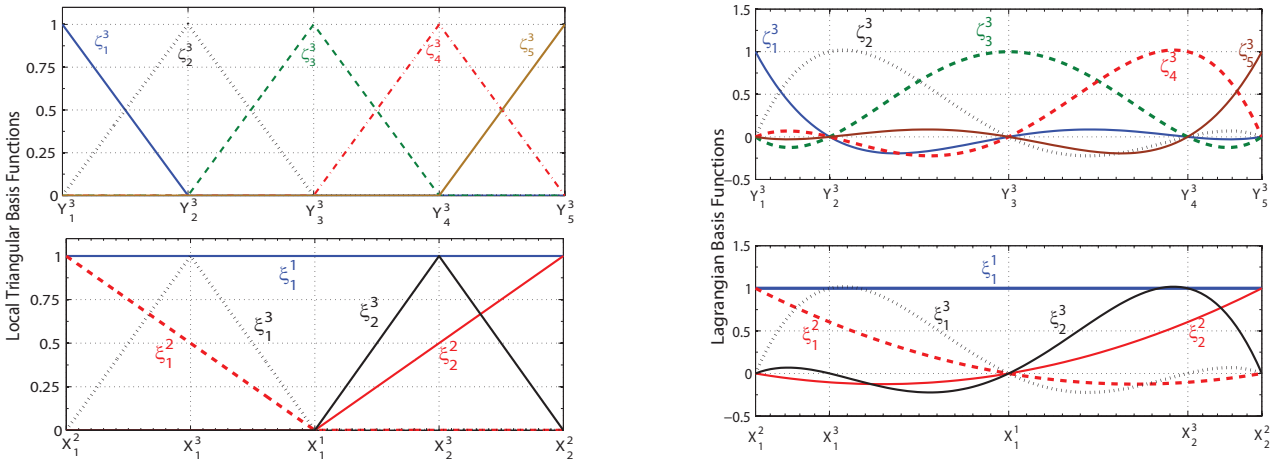

(a) (b)

Figure 4.1: The basis functions used in the construction of the sparse grid at level $d = 3$, according to Equation (4.5) (top) and Equation (4.14) (bottom): (a) local triangular basis functions, (b) Lagrange characteristic polynomial basis functions.

the basis functions used up to order $d = 3$ for local triangular basis functions and Lagrange polynomial basis functions, respectively. It is apparent from Figure 4.1 that $\xi_2^2 \equiv \zeta_3^2$ and $X_2^2 = Y_3^2$, $\xi_2^4 \equiv \zeta_4^4$ and $X_2^4 = Y_4^4$, etc. In other words, the top figures in both Figure 4.1a and Figure 4.1b depict all five nodes and basis functions that appear at $d = 3$ if one follows (4.5) for uni-dimensional case, whereas the bottom figuress depict all nodes and basis functions that appear in the same uni-dimensional problem, from level $d = 0$ up to level $d = 3$, if one follows the hierarchical formulation in (4.14). Since we follow the hierarchical formulation of (4.14) rather than (4.5), the hierarchical node subsets are $\mathcal{H}^{\Delta}_{N+d,N} = \mathcal{H}_{N+d,N} \setminus \mathcal{H}_{N+d-1,N}$, the set of nodes that are sampled at level d. For a 2-dimensional case, these set of nodes are demonstrated in Figures 4.2a and 4.2b, for equi-distant nodes and Chebyshev nodes, respectively.

Note that, each node that contributes at level d has two neighbors along each dimension, all of which will contribute to SGC formula in (4.14) at level $d+1$ (except for the nodes near the boundaries of the domain). For instance, in Figure 4.2 the

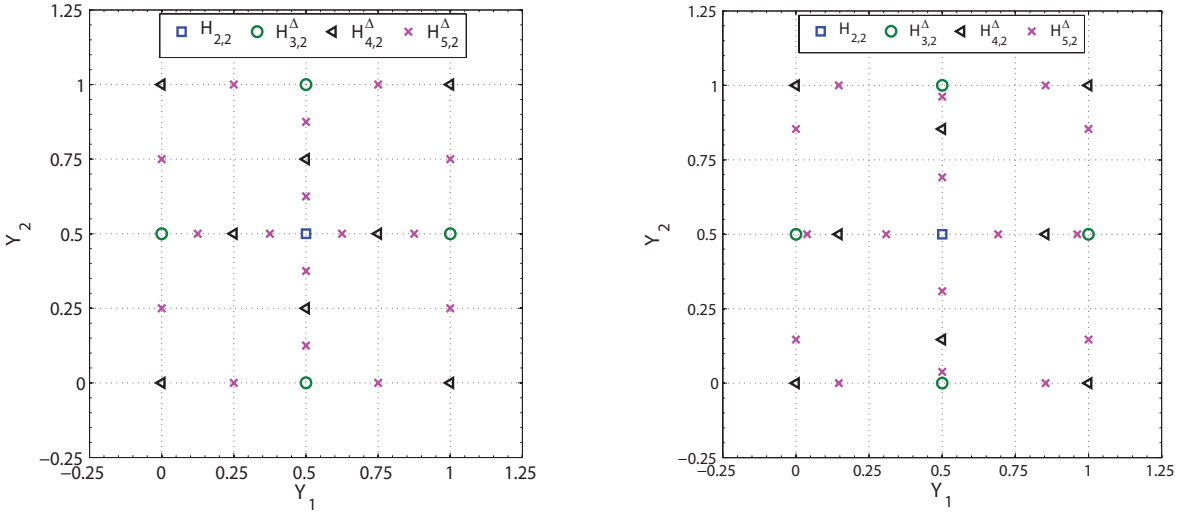

(a) (b)

Figure 4.2: The hierarchical node subsets from sparse grid level $d = 0$ up to level $d = 3$, $N = 2$ and $\Gamma = [0, 1]^2$, for (a) equi-distant nodes, (b) Chebyshev nodes.

origin $(0.5, 0.5)$ contributes at level $d = 0$, and it has $2N = 4$ neighbors contributing at level $d = 1$ (the set $\mathcal{H}^{\Delta}_{3,2}$). Hence, the SGC approximation to f at desired level d_{max} can be constructed starting with the origin at $d = 0$, then at each level detecting all neighbors to contribute the next level, and updating the function approximation hierarchically according to (4.14).

Once the sparse grid for $N-$dimensional function interpolation is constructed according to (4.14), $E[f]$ can now be computed as superposition of expectations of hierarchical differences, which is obtained by substituting (4.14) in (4.3):

$$E[\Delta\mathcal{A}_{(N+d,d)}(f)] = \sum_{|\mathbf{i}|_1=N+d} r_{\mathbf{i}}, \tag{4.17}$$

where

$$r_{\mathbf{i}} = \sum_{\mathbf{n} \in B_{\mathbf{i}}} w_{\mathbf{n}}^{\mathbf{i}} \left[\int_{Y_1} .. \int_{Y_N} \xi_{n_1}^{i_1}(Y_1) \otimes ... \otimes \xi_{n_N}^{i_N}(Y_N) \rho_1(Y_1) .. \rho_N(Y_N) dY_N .. dY_1 \right]. \quad (4.18)$$

4.2 Adaptive Sparse Grid Collocation Method

Among several adaptive construction enhancements to SGC, in this section we present the Adaptive Sparse Grid Collocation (ASGC) method [73], which resulted in one of the best performances for interpolating wave propagation problems we are interested in. Although the hierarchical construction we follow was detailed and the term "ASGC" was coined in [54], the algorithm in [73] presents slight differences and we follow the latter. In cases the function behavior is smooth with respect to a node, i.e. the surpluses $w_{\mathbf{n}}^{\mathbf{i}}(r)$ in (4.15) for the specific node are not significant with respect to the exact function $f(r)$, then simply the specific node under investigation is discarded from further neighbor refinement in the sparse grid. This way, the sparse grid is adaptively refined towards the singular, if not non-smooth regions in Γ. The threshold for adaptivity can be assumed in different means. We use a constant mean percentage error threshold t_e, where the error is defined as

$$\gamma_{\mathbf{n}}^{\mathbf{i}} = 100 \times Average \left(w_{\mathbf{n}}^{\mathbf{i}}(r) / f(r) \right). \quad (4.19)$$

The $Average(.)$ in (4.19) arithmetically averages its argument at all r, so that function interpolation at all r is performed simultaneously. If the error is smaller than a threshold, $\gamma_{\mathbf{n}}^{\mathbf{i}} < t_e$ for a particular node, the ASGC algorithm terminates the neighbor search for that node, and goes on to the rest of the nodes under search. Also note that ASGC method with $t_e = 0$ is non-adaptive, i.e. the case of SGC. To demonstrate how ASGC differs from the non-adaptive SGC, we consider finding the mean value of a test function:

$$f(Y_1, Y_2) = \frac{1}{\sqrt{10^{-4} + |(Y_1 - 1)^2 + (Y_2 - 1)^2 - 0.25|}}, \; Y_1, Y_2 \in [0, 2]. \quad (4.20)$$

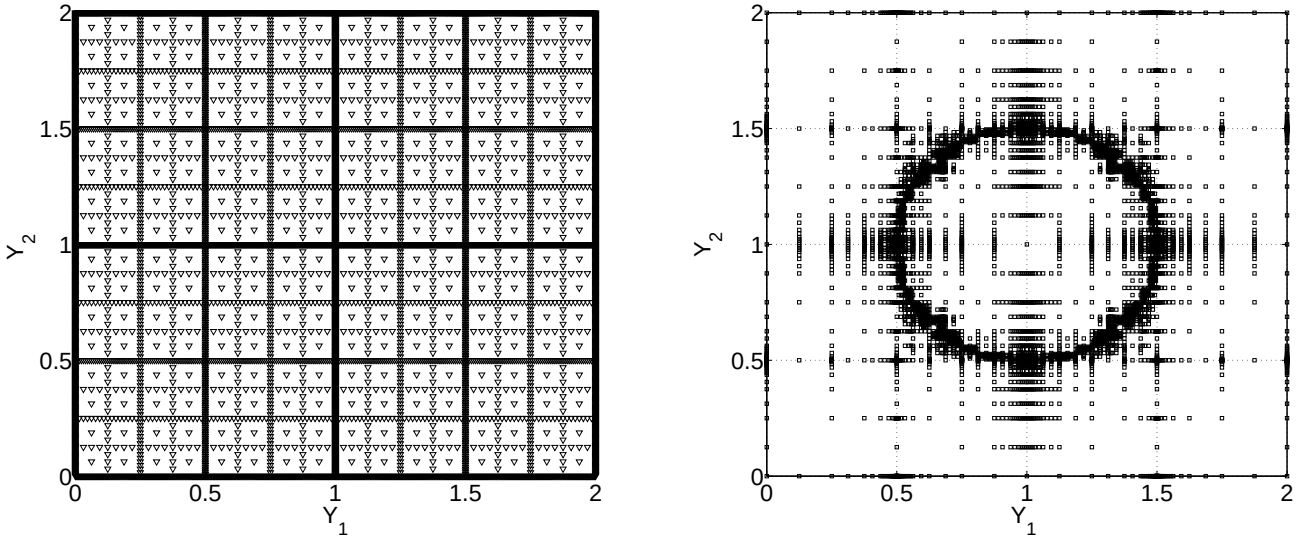

Figure 4.3: Demonstration of (a) SGC and (b) ASGC through the test example in (4.20).

This test function is deliberately chosen, that it takes large values around regions of the space $[0, 2]^2$ where $(Y_1 - 1)^2 + (Y_2 - 1)^2 = 0.25$, therefore the ASGC is expected to sample much denser in such regions. Figures 4.3a and 4.3b depict the nodes sampled by SGC and ASGC, respectively. Both sparse grid constructions were terminated after they sampled more than $7,000$ nodes. The SGC samples the $2-$dimensional space withouth taking into account the non-smooth regions of it, where it sampled $7,169$ nodes at level $d_{max} = 10$. However, as expected, the ASGC sampled much denser around the circle of radius 0.5 where the denominator in (4.20) very small, as well as around single nodes which also result in very large function value. The ASGC was terminated at level $d_{max} = 16$, and it sampled $7,221$ nodes with a threshold of $t_e = 20\%$, depicted in Figure 4.3b.

The ASGC grid refinement algorithm can be summarized as follows [73] (we here assume $\Gamma = [0, 1]^N$):

1. $d = 0$: The ASGC always starts with the origin of Γ, $\overline{y}_{origin}$, which is the only node in $\mathcal{H}_{N,N}$. $\mathcal{A}_{N,N} = f(\overline{y}_{origin})$. Now consider three node sets: the set of "frozen" nodes $\mathcal{F}_n$, the set of "active" nodes $\mathcal{A}_n$, and an "old" node set $\mathcal{O}_n$. d_{max} represents a maximum interpolation level for the sparse grid beyond which the algorithm terminates.

2. Put in $\mathcal{A}_n$ the $2N$ neighbors of the origin (from level $d = 1$). $\mathcal{F}_n = \varnothing$, $d = 1$.

3. while $\mathcal{A}_n$ is not empty and $d < d_{max}$ do:

   - $\mathcal{O}_n = \mathcal{A}_n$, then set $\mathcal{A}_n = \varnothing$. For each of the nodes in $\mathcal{O}_n$, check their $2N$ immediate neighbors (from level d). If all of them are in $\mathcal{F}_n$, freeze the current node also, and consider the next node in $\mathcal{O}_n$. If not all neighbors were frozen, calculate the surplus $w_{\mathbf{n}}^{\mathbf{i}}$.

     (a) if the calculated surplus results in $\gamma_{\mathbf{n}}^{\mathbf{i}} \geq t_e$, refine the current node further, i.e. determine its neighbors from level $d + 1$, put them in $\mathcal{A}_n$. Update $\mathcal{A}_{(N+d,N)}(f)$.

     (b) else put the current node in $\mathcal{F}_n$.

     (c) endif

   - $d = d + 1$.

   - Update any desired statistics of f, e.g. the expectation $E[f]$.

4. endwhile

4.3 $h-$Adaptive Generalized Sparse Grid Method

The second adaptive strategy we will apply for computing $E[f]$ is the $h-$Adaptive Generalized Sparse Grid ($h-$GSG) method [36]. Although this method also is based on Smolyak's sparse grid construction and obeys (4.15) and (4.16), the construction

structure is different than in (4.14). Namely, the concept of "level" $|\mathbf{i}|_1 = N + d$ is not kept in this method, but rather each super-index $\mathbf{i}$ is treated itself, rather than along with the same level super-indices as in (4.14). Different from ASGC, this method creates an adaptive refinement not only in the nodes of the sparse grid, but also in the super-indices $\mathbf{i}$. The method roots back to [26], where in that original work only super-indices $\mathbf{i}$ are adaptively selected, and all nodes entailed with $\mathbf{i}$ according to the node set $B_{\mathbf{i}}$, are included in the sparse grid. In $h-$GSG however, adaptive refinement in between the nodes in $B_{\mathbf{i}}$ of a selected index $\mathbf{i}$ is also present.

The $h-$GSG algorithm of [36] is summarized below:

1. $\mathbf{i} = \mathbf{1} = (1, 1, .., 1)$. The algorithm always starts with the unity super-index, which entails only a single node, the origin of Γ, $\overline{y}_{origin}$. Now consider two index sets, the "active" index set $\mathcal{A}_i$ and the "old" index set $\mathcal{O}_i$. Also, let r denote a global error indicate, and ϵ_{tol} a pre-determined tolerable error level.

2. $\mathcal{A}_i = \{\mathbf{i}\}$, $\mathcal{O}_i = \varnothing$, compute $r_{\mathbf{i}}$ according to (4.18), and set $r = r_{\mathbf{i}}$.

3. <u>while</u> $r > \epsilon_{tol}$ do:

   - select $\mathbf{i}_b \in \mathcal{A}_i$ with largest $r_{\mathbf{i}}$ of all indices in $\mathcal{A}_i$.
   - $\mathcal{A}_i = \mathcal{A}_i \setminus \{\mathbf{i}_b\}$, $\mathcal{O}_i = \mathcal{O}_i \cup \{\mathbf{i}_b\}$.
   - $r = r - r_{\mathbf{i}_b}$.
   - <u>for</u> $m = 1, 2, .., N$ do:

     (a) $\mathbf{j} = \mathbf{i} + \mathbf{e}_m$, where $\mathbf{e}_m$ is the mth unit-vector.

     (b) <u>if</u> $\mathbf{j} - \mathbf{e}_k \in \mathcal{O}_i$, $\forall k = 1, 2, .., N$, then

     - $\mathcal{A}_i = \mathcal{A}_i \cup \{\mathbf{j}\}$
     - $CreateGrid(\mathbf{j})$

- $r = r + r_{\mathbf{j}}$.
- Update any desired statistics of f, e.g. the mean value $E[f]$.

(c) endif

- endfor

4. endwhile

The *CreateGrid*($\mathbf{i}$) routine identifies the selected nodes entailed with a super-index $\mathbf{i}$, and includes them in the sparse grid. This routine detects the nodes $X_{\mathbf{n}}^{\mathbf{i}}$ according to (4.16), but includes only those nodes that are significant. For details of this node refinement routine we refer the reader to [36], as we exactly follow it for $h-$GSG. A demonstration of the $h-$GSG sparse grid algorithm is depicted in Figure 4.4 for an $N = 2-$dimensional domain. The top row depicts a sample evolution of the sets $\mathcal{A}_i$ and $\mathcal{O}_i$. The textured grey boxes represent old indices (set $\mathcal{O}_i$), and solid blue boxes with label "A" represent the active indices (set $\mathcal{A}_i$). In the second row of Figure 4.4, the nodes that correspond to old indices from the top row are depicted. The label "O" stand for those indices, at each step, that were included in $\mathcal{O}_i$ and excluded from $\mathcal{A}_i$. The indices indicated as light blue boxes on the other hand are at each step of the algorithm evolution the index $\mathbf{i}_b \in \mathcal{A}_i$ that has the highest $r_{\mathbf{i}}$. Note that such an index has $2N$ forward neighbors to be included in $\mathcal{A}_\rangle$ (neighbors pointed with arrows in Figure 4.4). Note that in generation of Figure 4.4 Chebyshev nodes are assumed.

In order to pictorially discern $h-$GSG from SGC and ASGC, a similar $N = 2-$dimensional index evolution in Figure 4.5 is depicted for SGC formula of (4.5), where in this case at level d of SGC, all indices that satisfy $|\mathbf{i}|_1 = d$ are included in the sparse grid at the same time (shown as solid black boxes in the top row). The bottom row depicts the nodes present after the corresponding SGC level. Note that for demonstration purpose equi-distant nodes are assumed in Figure 4.5.

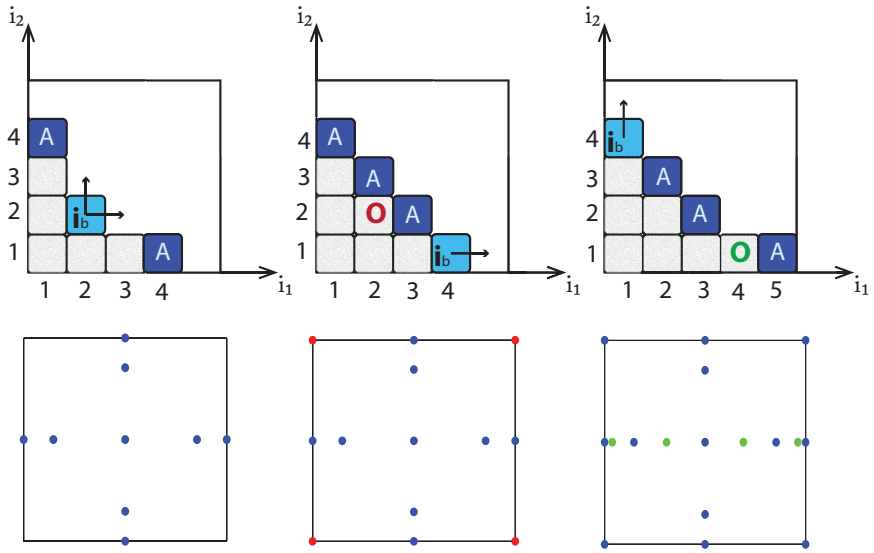

Figure 4.4: A sample evolution of index sets of $h-$GSG for an $N = 2-$dimensinal case. The top row depicts sets $\mathcal{O}_i$ (textured grey) and $\mathcal{A}_i$ (solid blue), whereas the bottom row depicts nodes (Chebyshev) entailed with $\mathcal{O}_i$.

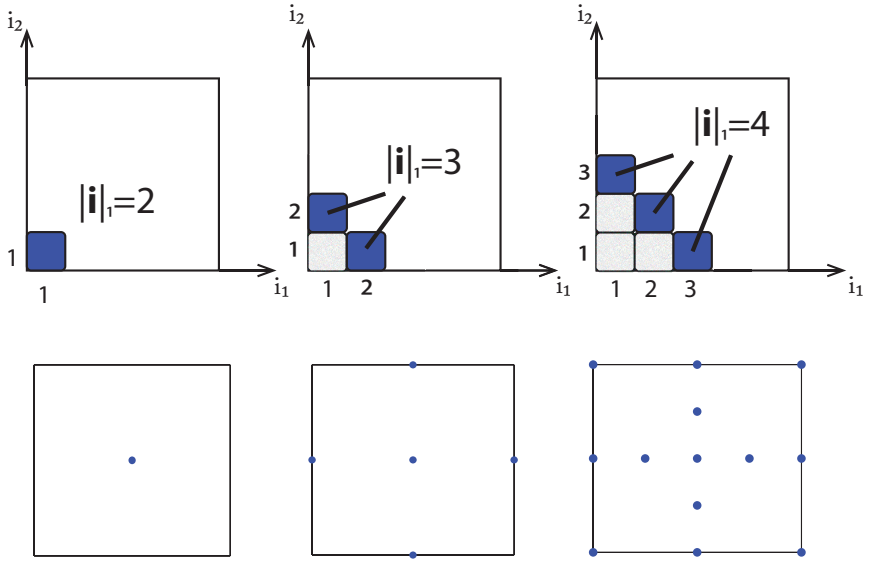

Figure 4.5: Index evolution of the non-adaptive SGC formula in (4.5), from level $d = 0$ to $d = 2$, where $N = 2$. The top row corresponds to indices added to sparse grid at level $|\mathbf{i}|_1 = N+d$, and the bottom row depicts the nodes (equi-distant) present after the corresponding sparse grid level.

4.4 High Dimensional Model Representations

Given the fact that the curse of dimensionality occurs soon enough with increasing N for sparse grid methods, the high-dimensional model representations (HDMR) will be used for as a dimensionality-reducing tool and as a tool to avoid redundant sampling.

First developed with the interest of extracting input parameter correlations in chemical reactions and in finance, the HDMR is an exact expansion of a high dimensional system in terms of pth dimensional sub-system, or "components", $p = 0, 1, .., N$ [71, 70]. Lately, Ma and Zabaras [55] have merged their ASGC method with HDMR, and given a thorough interface algorithm between HDMR and ASGC, henceforth referred to as "HDMR+ASGC". Although we made a specific modification to their original proposition in a way that resulted in better adaptivity in constructing the sparse grid in our applications, the rest of what is presented next owes the credit to [55].

The HDMR were derived in accordance with a theorem of Kolmogorov [52], which allows high-dimensional functions to be represented as superposition of uni-variate functions. For the $N-$dimensional target function, the HDMR is:

$$\begin{aligned} f(y) = f_0 \quad &+ \quad \sum_{i=1}^{N} f_i(Y_i) + \sum_{1 \le i_1 < i_2 \le N} f_{i_1 i_2}(Y_{i_1}, Y_{i_2}) \\ &+ \quad ... + \sum_{1 \le i_1 < ... < i_p \le N} f_{i_1 ... i_p}(Y_{i_1}, ..., Y_{i_p}) \\ &+ \quad f_{12...N}(Y_1, ..., Y_N). \end{aligned} \tag{4.21}$$

f_0 is the mean component evaluated at an $N-$dimensional predetermined node. Since we have no a-priori knowledge of the system, the geometric center of Γ is selected: $f_0 = f(\overline{y}_{origin})$. $f_{i_1 i_2 ... i_p}$ is a pth order component function and is subject to p dimensional uncertainty in Γ. Note that the total number of components up to

lth order in (4.21) is $\sum_{p=0}^{p=l} \frac{l!}{p!(l-p)!} = 2^l$. The component functions can be recursively computed, which is detailed in [29], where below only components up to 2nd order are given:

$$\begin{aligned} f_0 &=: P_0[f(y)] = f(\overline{y}_{origin}), \\ f_j(Y_j) &=: P_j[f(y)] = F^j(Y_j) - P_0[f(y)], \\ f_{j_1 j_2}(Y_{j_1}, Y_{j_2}) &=: P_{j_1 j_2}[f(y)] \\ &= F^{j_1 j_2}(Y_{j_1}, Y_{j_2}) - P_{j_1}[f(y)] - P_{j_2}[f(y)] - f_0, \end{aligned} \tag{4.22}$$

and in general all 2^N components can be computed through

$$f_{\mathbf{u}}(y_{\mathbf{u}}) =: P_{\mathbf{u}}(y_{\mathbf{u}}) = F^{\mathbf{u}}(y_{\mathbf{u}}) - \sum_{\mathbf{v} \subset \mathbf{u}} f_{\mathbf{v}}(y_{\mathbf{v}}), \tag{4.23}$$

where for an order-s component vector $\mathbf{u} = \{j_1, .., j_s\}, j_1 < .. < j_s$, $y_{\mathbf{u}} := (Y_{j_1}, .., Y_{j_s})$, $|\mathbf{u}| = s \leq N$. Note that in the expansion form (4.21) we only need $P_{\mathbf{u}}$, which is recursively computed from (4.23). Finally, $F^{\mathbf{u}}(y_{\mathbf{u}})$ is an $s-$dimensional term, that is obtained by setting all variables in $y = (Y_1, .., Y_N)$ to their fixed position at $\overline{y}_{origin}$, except for the s variables present in $\mathbf{u}$. For instance, for a $3-$dimensional system in the domain $\Gamma = [0, 1]^3$, $F^2(Y_2) = f(0.5, Y_2, 0.5)$, is a uni-dimensional term that is only a function of Y_2. To illustrate how the $N-$dimensional domain Γ is partitioned in the coarse of HDMR, Figure 4.6 demonstrates for $N = 2$ and $N = 3$ cases.

For several physical systems it has been shown that the first few order components in (4.21) dominate the overall behavior of f, thus majority of the components can be eliminated, or adaptive selection among them are allowed. To demonstrate the effect of component orders, we depict in Figure 4.7 the absolute value of each component's contribution to the expected value $E[f]$, for f the target function to a $N = 20-$dimensional problem that will be studied in Section 5.1. The twenty components of order $p = 1$ indicate how important the nth axis of Γ is, $n = 1, 2, ..., 20$.

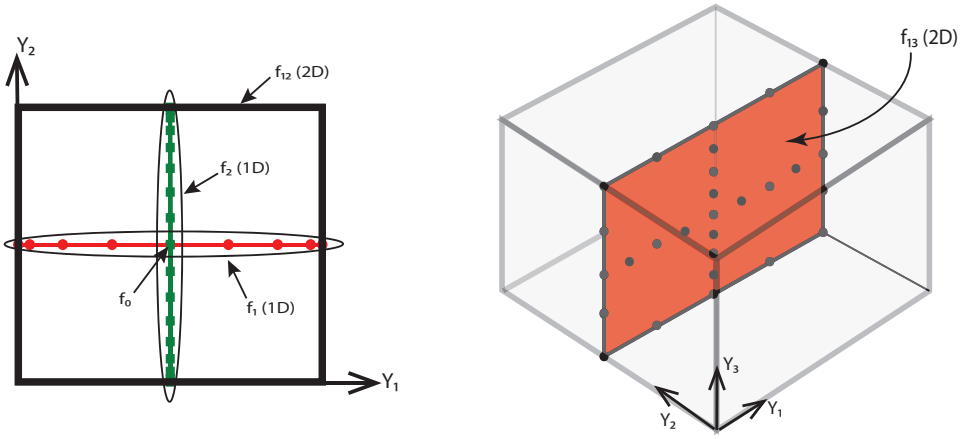

Figure 4.6: Demonstration of domains for sample uni-dimensional (left) and 2−dimensional (left and right) HDMR components.

Similarly, the magnitudes for second order components give idea of how each 2-tuple axes behave collaboratively towards $E[f]$. Prior to applying any elimination strategy the HDMR in (4.21) is simply truncated at order $p = 4$. It is seen from Figure 4.7 that most of the 4th order component contributions are nearly zero. Note that out of the 2^{20} total components, only first few hundred components contribute up to an accuracy of one millionth of $|f_0|$. Also each pth order component is a p-dimensional problem to be interpolated, and the ASGC will be used for tackling each component.

4.4.1 HDMR+ASGC

In this subsection we present how adaptive elimination of HDMR components, and solution of each component without redundant sampling is presented. This method aims computation of the expectation of a high-dimensional funcion, $E[f]$. As stated above, we follow [55] for the most part. Below our procedure is given:

1. Let θ denote a threshold value, which will be used as an indicator for an elimination to be explained later. For example, $\theta = 0.01$ means that the elimination will be based on 1% error.

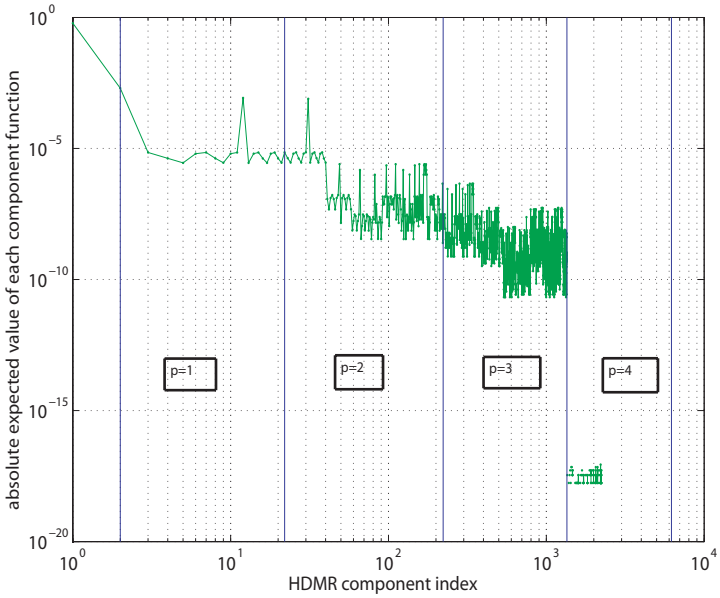

Figure 4.7: The contribution of each component function at orders $p \leq p_{max} = 4$, for an $N = 20$ dimensional problem with FDFD solver from Section 5.1.

2. Let $p_{max} \in \mathbb{N}^+$ denote the maximum order at which HDMR in (4.21) will be truncated, i.e. it represents the highest dimensionality a component in (4.21) can have.

3. Pre-determine parameters of the ASGC method to be accessed: determine d_{max} and t_e of Section 4.2.

4. Now define four sets that hold component vectors ($\mathbf{u}$),

   - $\mathcal{R}_u$: set of "admissible" components, which are each order $p+1$. The set is redefined at each order p, $p = 0, 1, .., p_{max} - 1$.

   - $\mathcal{T}_u$: set of "selected" components, redefined at each order according to θ criterion.

- $\mathcal{C}_u$: set of "all" components considered in the coarse of HDMR. This set will monotonically enlarge, where the cardinality of this set can never exceed 2^N according to (4.21).

- $\mathcal{I}$: set of "important dimensions", i.e. important order-1 components out of the N order-1 components in (4.21).

5. Set $\mathcal{R}_u = \varnothing$, $\mathcal{T}_u = \varnothing$, $\mathcal{C}_u = \varnothing$, $\mathcal{I} = \varnothing$. Compute $f_0 = f(\overline{y}_{origin})$. Set $p = 1$.

6. Interpolate each of the N order-1 components using ASGC with parameters d_{max} and t_e, and compute $E[f_j]$, $j = 1, 2, .., N$. Add each order-1 component $\{j\}$ in $\mathcal{C}_u$. Those order-1 components that satisfy $\eta_j > \theta$ are labelled as being "important", and only these components $\{j\}$ are put in both $\mathcal{I}$ and $\mathcal{T}_u$, where

$$\eta_j = \frac{|E[f_j]|_{L_1(D)}}{|f_0|_{L_1(D)}}, \tag{4.24}$$

   where as the first norm $|.|_{L_1(D)}$, we use the sum of absolute values of the evaluated function at each spatial/temporal variable r ($f(y) \equiv f(y, r)$).

7. <u>while</u> $p < p_{max}$

   - Components to be considered (at order$-(p+1)$) are obtained by the routine $CompAdmit(.,.)$, which is detailed later in this section, and these components are put in the admissible set: $\mathcal{R}_u \leftarrow CompAdmit(\mathcal{T}_u, \mathcal{I})$.

   - $\mathcal{T}_u = \varnothing$.

   - If $\mathcal{R}_u \neq \varnothing$, for each component $\mathbf{u}$ from $\mathcal{R}_u$ use ASGC with parameters d_{max} and t_e to get $E[f_{\mathbf{u}}(y_{\mathbf{u}})]$.

– for each $\mathbf{u}$ from $\mathcal{R}_u$ compute error $\eta_{\mathbf{u}}$, where

$$\eta_{\mathbf{u}} = \frac{|E[f_{\mathbf{u}}]|_{L_1(D)}}{\left|\sum_{\mathbf{v}\in\mathcal{C}_u,|\mathbf{v}|<|\mathbf{u}|} E[f_{\mathbf{v}}]\right|_{L_1(D)}}. \tag{4.25}$$

– Put component $\mathbf{u}$ into $\mathcal{C}_u$

– If $\eta_{\mathbf{u}} > \theta$ put component $\mathbf{u}$ into $\mathcal{T}_u$.

– endfor

– $\mathcal{R}_u = \varnothing$.

- $p = p + 1$.

8. endwhile

Next, we discuss how the order$-(p+1)$ components are admitted, given the set of "important" dimensions ($\mathcal{I}$) and order$-p$ components already computed ($\mathcal{T}_u$).

CompAdmit$(\mathcal{T}_{\mathbf{u}}, \mathcal{I})$

This routine is the main difference we have with respect to the procedure in [55], where they use a more conservative component admission strategy than ours. Below routine returns the components to be admitted at order$-(p+1)$. The assumption is that all components in the input $\mathcal{T}_u$ are order$-p$.

- $\mathcal{R}_u = \varnothing$
- for $n = 1$, $n \leq \mathcal{I}$.size(), $n++$
  - for $m = 1$, $m \leq \mathcal{T}_u$.size(); $m++$
    - if $n \notin \mathcal{T}_u(m)$, then $\mathcal{R}_u = \mathcal{R}_u \cup Concatenate\{\mathcal{T}_u(m), n\}$.
  - endfor

- endfor
- return $\mathcal{R}_u$.

The concatenation of component vectors restricts ascending order, and a component vector can contain unique integers only. For instance, $Concatenate\{\{1,2,3\},\{1,4\}\} = \{1,2,3,4\}$. Finally, we demonstrate a sample adaptive component elimination in Table 4.1, for an $N = 5-$dimensional system that will be studied in Section 5.3. This elimination was performed with $\Theta = 10^{-4}$. Note that the first RV, that corresponds to the component f_1 in (4.21) and component vector $\{1\}$ in Table 4.1, produces an indicator of 10^{-11}, and is the only unimportant dimension according to $\theta = 10^{-4}$. Out of the 31 components (other than f_0) present for this $5-$dimensional system, 14 of them were considered and interpolated with an ASGC solver with parameters $t_e = 0.5$ and $d_{max} = 6$. Indeed, as the data in Table 4.1 will be revisited in Section 5.3, it corresponds to the "HDMR+ASGC" curve in Figure 5.17a. This elimination resulted in use of $1,777$ nodes (samples) to evaluate the function f at, whereas the SGC method (non-adaptive) of $d_{max} = 6$ in an $N = 5-$dimensional space requires $6,993$ evaluations.

$\mathbf{u}$	$\eta_{\mathbf{u}}$	$\mathbf{u}$	$\eta_{\mathbf{u}}$
{1}	10^{-11}	{3,4}	1.03×10^{-3}
{2}	0.0160	{3,5}	5.31×10^{-4}
{3}	0.0761	{4,5}	3.20×10^{-3}
{4}	9.21×10^{-3}	{2,3,4}	4.01×10^{-5}
{5}	0.0206	{2,3,5}	7.04×10^{-6}
{2,3}	1.89×10^{-4}	{3,4,5}	9.10×10^{-5}
{2,4}	5.18×10^{-5}		
{2,5}	1.56×10^{-6}		

Table 4.1: The errors $\eta_{\mathbf{u}}$, for a sample HDMR+ASGC component elimination performed ($N = 5$), where the data corresponds to Figure 5.17a.

Why not HDMR+$h-$GSG?

Note that the sparse grid interpolator in HDMR+ASGC could be replaced with any other interpolation scheme, e.g. with $h-$GSG that would make the method HDMR+$h-$GSG. However, a drawback about the use of the $h-$GSG method is that, it is often unpredictable if the $h-$GSG algorithm will terminate after the optimum Q have reached. In other words, it is common that the $h-$GSG algorithm, with a prescribed ϵ_{tol}, does not terminate, and keeps increasing the number of samples Q. This is occurring because the $h-$GSG makes a search of individual super-indices $\mathbf{i}$ to include in the sparse grid. However ASGC makes a "macro-search", in the way that all super-indices $\mathbf{i}$ associated with a level d in (4.14) are included altogether. Therefore, with the setting presented in Section 4.3, it is not as compatible to be interfaced with the HDMR.

Lastly, the memory performance comparison of HDMR+ASGC and $h-$GSG is postponed to the next chapter, and will be discussed in Section 5.1.1 through a $N = 100-$dimensional test example.

4.5 About Quasi Monte Carlo Methods and Convergence Rates

The low discrepancy sequences generated in a quasi-random fashion have gained popularity due to their widespread availability and fast converging ability for low and moderate dimensional systems. These methods are named Quasi-Monte Carlo (QMC) methods in general, and among the choices we select to use two famous sequences: Sobol quasi-random sequences [80] and Halton quasi-random sequences [31]. Although it is not the purpose of this work to test the strength of the QMC methods, we will use them as a reference for cases where the performance of the sparse grids are questionable. Therefore, for each application in the following sections, we demonstrate the QMC methods with some of the selected test problems. The

QMC methods have $O(\log^N(Q)/Q)$ convergence rate [62]. Although empirical results show that $O(1/Q)$ rate have been achieved for many analytical function types [75], the performance is dominated by the $\log(.)$ term for high$-N$ cases. In the error convergence results with QMC sequences we demonstrate, some examples will not achieve the $O(1/Q)$ rate. This might be due to insufficient highest Q we consider for asymptotic analysis, or due to the $\log^N(Q)$ term in high$-N$ cases.

The SGC method on the other hand has convergence rate of $O\left(\frac{(\log Q)^{(N-1)(s+1)}}{Q^s}\right)$ [64]. Here s represents a "smoothness" of the target function f, and causes the numerator term to dominate as the function is less smooth in the random space. However, for an arbitrary problem we do not have a value for s. Since both HDMR+ASGC and $h-$GSG methods are based on the SGC method, they are expected to attain better convergence than the above rate. However, we do not have an explicit expression for these adaptive methods' performance.

As mentioned before, MC sampling has $O(1/\sqrt{Q})$ rate irrespective of target function and dimensionality.

CHAPTER 5

PROPAGATION PROBLEMS WITH UNCERTAINTY

There are several sources of uncertainties in propagation environments. In this chapter we consider electromagnetic propagation/scattering problems that are subject to different uncertainties. There will be three different model problems studied in respective sections.

The first problem is the simplest scenario of waves scattered from spatially one-dimensional dielectric media, where the permittivity and permeability of the dielectrics are uncertain. A finite difference method is used as the numerical solver to the problem. The dimensionality of randomness studied in this example will vary from $N = 2$ up to $N = 100$. Through different uncertainties imposed in the dielectrics, the performance of $h-$GSG and HDMR+ASGC methods presented in Chapter 4 will be assessed. Also, the $N = 100-$dimensional example will be used for comparing physical memory required by these methods.

The second problem is the forward-scattering problem of low-grazing angle propagation over randomly shaped perfectly conducting (PEC) surfaces, where the propagation environment is half-open free-space, similar to the model geometry in Chapter 3. The numerical solver of the problem is an integral equation solver that solves for the PE type propagation from Chapter 5.6 [45], [61]. Through generation of the random surface by assuming Gauss-shaped hills, the dimensionality N of the problem is kept controlled. This is a simplification to the originally proposed problem of scattering from a numerically generated rough surface with Gaussian height statistics, in

which the sparse grid methods fail to give better estimates than MC sampling and QMC methods.

The last problem is the prediction of expected power and complex field magnitude far from the transmitter in lower troposphere, where the randomness is present due to uncertain ducting that is realized at low elevations. The dimensionality of this problem is fixed at $N = 5$, and the support each independent RV is derived from published measured data [102]. Due to low dimensionality, this example will clearly assert the favor of sparse grid methods compared with MC sampling and QMC methods.

This chapter contains three sections, reserved for above problems in the given order, and in the final section we will conclude the use of sparse grid methods for the applications studied.

5.1 First Scattering Example: Reflection from multi-layered slabs

A test case to study performance of sparse grid methods is the problem of plane wave normally incident on a series of infinite (in the transverse plane) planar dielectric slabs of finite thicknesses as shown in Figure 5.1, where the K slabs are assumed to exist between two open half-infinite free space regions. The parameters of the $k-$th slab are the thickness h_k, permittivity ϵ_k, permeability μ_k, conductivity σ_k, and thus complex wave number γ_k, $k = 1, 2, .., K$. This example is instructive because it will explain how sparse grids may be applied to more complicated scattering problems, such as rough surface scattering. The target in this example is to compute expected value of the reflection coefficient, $|E[R]|$, where R is the reflection coefficient for the normally incident wave, as depicted in Figure 5.1.

The analytical solution for R is straightforward to derive utilizing opposite directed plane wave pair-solutions in each slab and enforcing field continuities at interfaces [6]. Numerical solvers require a $1-$dimensional discretization only. The plane wave

normally incident from the left side of the slabs can be represented as $\psi^{inc} = e^{ik_o z}$, where it has unity magnitude, $i = \sqrt{-1}$, k_o is the free space wave number, z is the space coordinate normal to the slabs, and the time convention is $e^{-i\omega\tau}$ in radian frequency ω and time τ. The governing equation is the 1−dimensional Helmholtz equation

$$\left(\frac{\partial^2}{\partial z^2} - \gamma^2(z)\right)\psi = 0, \tag{5.1}$$

where $\gamma(z)$ is the complex wavenumber which reduces to $\gamma_o = -ik_o$ in free space. The Finite Difference Frequency Domain (FDFD) formulation [9] is straightforward to apply at a fixed frequency. The discretization of (5.1) along z with second order central-difference approximation of the derivative, like in (2.9), results in the matrix equation

$$\overline{\psi} = S^{-1}F, \tag{5.2}$$

where $\overline{\psi}$ represents the vector of discrete values for x component of the electric field along z. The continuity of magnetic fields requires continuity of $\partial/\partial z\,[\psi]_{z=z_k}$, where z_k is the position of $k-$th interface in Figure 5.1, $k = 1, 2.., K+1$. Recall that the two sides of the slabs are open free space, therefore absorbing boundary conditions (ABCs) are placed at one free space wavelength distance from the first and last interfaces. At the operating frequency of 300 MHz in our simulations, this corresponds to 1 meter. Regarding domain truncation in the numerical scheme , perfect absorption can be performed by the following absorbing conditions formulated for the discrete version of equation (5.2):

$$\begin{aligned} \overline{\psi}(I+1) &= e^{-j\theta}\overline{\psi}(I), \\ \overline{\psi}^{ref}(0) &= e^{-j\theta}\overline{\psi}^{ref}(1), \end{aligned} \tag{5.3}$$

where $\theta = \cos^{-1}\left[1 - \frac{(k_o\Delta_o)^2}{2}\right]$, and I is the size of $\overline{\psi}$. Δ_o is the step size used for discretization of the free-space regions. $\overline{\psi}^{ref}$ is the "reflected" field, which is propagating along negative z. One can easily switch to the total field formulation by using the field separation $\overline{\psi} = \overline{\psi}^{ref} + \overline{\psi}^{inc}$.

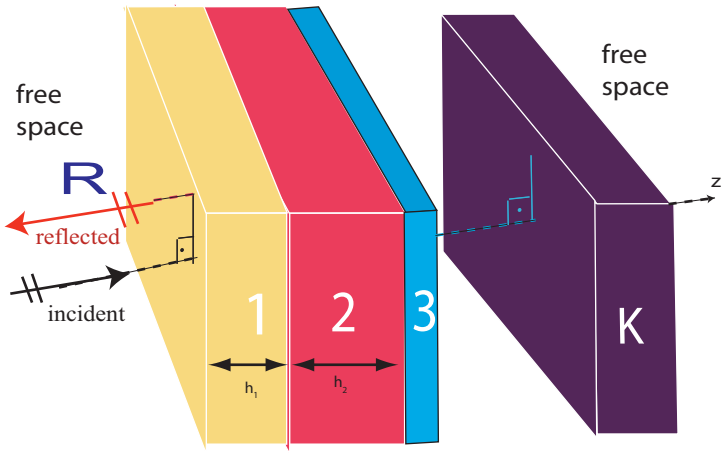

Figure 5.1: Normal-incidence reflection from multi-layered media.

The size of vector $\overline{\psi}$ is

$$I = 1 + \frac{2\lambda_o}{\Delta_o} + \sum_{k=1}^{K} \frac{h_k}{\Delta_k}, \tag{5.4}$$

where λ_o is the free space wavelength and Δ_k is the step size in $k-$th slab. A demonstration of the numerical code is in Figure 5.2 for a 3-slabs problem, where the left axis corresponds to the magnitude of analytical and numerical R, and the right axis corresponds to the magnitude of the total field ψ. The ABCs and the

material interfaces are marked with vertical lines, where "FS" denotes free space. Both numerical and analytical reflected fields normalized by the magnitude of incident plane wave are plotted between the ABC at $z = 0$ and the first interface, where the solid curve is the total field (normalized by the incident plane wave magnitude) everywhere. The FDFD solver gives a reflection coefficient $|R| = 0.1494$, which is confirmed by the analytical result with a relative error of 0.0185% at the ABC location ($z = 0$). The thicknesses h_k are randomly selected from a uniform RV $U[0.1, 3.1]$ meters, and both the relative permittivities ϵ_k and relative permeabilities μ_k are selected from $U[5, 15]$, $k = 1, 2, 3$. The conductivity of each slab is fixed at $5mS/$meters, which is kept fairly small with respect to $\omega\epsilon_o$, so that the slabs are only slightly lossy, where ϵ_o is the free space permittivity. We keep a constant step size ratio $\frac{\lambda_k}{\Delta_k}$ for each slab and free space where λ_k is the wavelength in $k-$th slab, thus prevent over-or-under sampling. This is useful especially for cases where dynamic variability of the slab materials is large, which makes large wavenumber fluctuations from one slab to the next. For the example in Figure 5.2 this ratio is 20. Increasing this ratio makes the FDFD solver even more accurate than in Figure 5.2 in the expense of increased problem size. The sampled parameters are given in the caption of Figure 5.2. It is important to remind the reader that once all random parameters are fixed, the sampled problem becomes deterministic and is solved with the FDFD solver.

The series of examples that will be considered next will shed light on the convergence performance of the sparse grid methods applied to the canonical reflection problem discussed above. In all the results, we seek the mean value $|E[R]|$ of the reflection coefficient. These examples are listed in Table 5.1 along with the reference solution (exact $|E[R]|$), at the operating frequency of 300 MHz.

The first example is the case of a single infinite slab inserted in free space, with 2 RVs ($N = 2$): relative permittivity and relative permeability of the slab are uniform

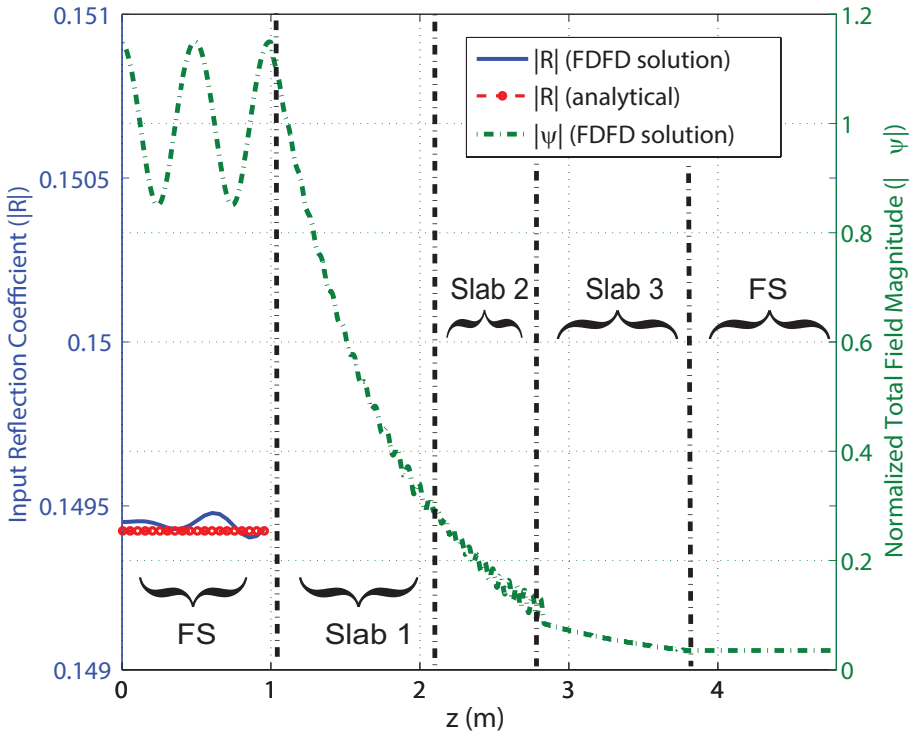

Figure 5.2: Analytical reflection coefficient (red circles), numerical reflection coefficient (solid blue), and total field magnitude (dashed green). Parameters: f=300 MHz, $h_1 = 1.07$ m, $h_2 = 0.765$ m, $h_3 = 0.970$ m, $\epsilon_1 = 5.10$, $\epsilon_2 = 6.37$, $\epsilon_3 = 13.19$, $\mu_1 = 9.31$, $\mu_2 = 13.90$, $\mu_3 = 12.4$, $\sigma_1 = \sigma_2 = \sigma_3 = 5$ mS/m. $|R| = 0.1494$ (analytical).

RVs $\epsilon = U[1,5]$, $\mu = U[1,5]$. The slab thickness is 0.5 meters, and the conductivity in the slab is $\sigma = 1mS/$meters. The magnitude of the mean reflection coefficient is $|E[R]| = 0.00538$, which is obtained from 10^7 MC samples, where the convergence results are shown in Figure 5.3a. The magnitude of the corresponding mean reflection estimates, $|E[R]|$ are depicted in Figure 5.3b. For this first example, note that we only depict solutions with the SGC (non-adaptive) and ASGC (adaptive) methods, with increasing levels d from (4.14). In Figure 5.3a the first-norm errors are defined as:

$$Err_{L_1} = \frac{|h_{tar} - h_{ref}|}{|h_{ref}|}, \tag{5.5}$$

where h_{tar} and h_{ref} are the estimate and exact (reference) $E[R]$, respectively.

To demonstrate use of different node sets, we depict both SGC and ASGC results with both equi-distant and Chebyshev nodes. It should be stressed that in Figure 5.3a, and in all upcoming error convergence results, each marker of SGC and ASGC methods corresponds to a level d in (4.14). For instance, it is apparent from both equi-distant and Chebyshev cases that SGC method at level $d = 8$ ($Q = 1,537$), attains smaller error than the MC sampling with $Q = 10^6$ nodes. This is expected since the dimensionality in this example is only $N = 2$. On the other hand, the ASGC method in both equi-distant and Chebyshev cases improved the error convergence of their non-adaptive (SGC) counterparts, where the ASGC with Chebyshev nodes attained the lowest error depicted in Figure 5.3a while using only 423 nodes. The convergence rates listed in the legend are obtained from the slopes of the best-fit lines for each curve. Note that MC sampling curve has a rate of $Q^{-0.491}$, which is quite close to the asymptotic rate of $1/\sqrt{Q}$ one expects in MC sampling.

A higher dimensional case is considered in Example 2, where the random permittivities and permeabilities of the three slabs make the problem $N = 6-$dimensional. Each slab is 0.5 m thick, and each has conductivity 1 $mS/$meters. In this particular

Example	K (# slabs)	N	RV List	$\lvert E[R]\rvert$ (reference)	Fixed Values
1	1	2	ϵ_1, μ_1	5.3861×10^{-3}	$\sigma_1 = 1mS/\text{m}$ $h_1 = 0.5\text{m}$
2	3	6	$\epsilon_1, \epsilon_2, \epsilon_3$ μ_1, μ_2, μ_3	1.032×10^{-2}	$\sigma_1 = \sigma_2 = \sigma_3 = 1mS/\text{m}$ $h_1 = h_2 = h_3 = 0.5\text{m}$
3	10	20	$\epsilon_1, .., \epsilon_{10},$ $\mu_1, .., \mu_{10}$	0.60437	$\sigma_1 = 1.67mS/\text{m}$ $\sigma_k = 0, k \neq 1$ $h_1 = 2\text{m}$, $h_k = 0.5\text{m}$,$k \neq 1$
4	50	100	$\epsilon_1, .., \epsilon_{50},$ $\mu_1, .., \mu_{50}$	0.634229	$\sigma_1 = 1.67mS/\text{m}$ $\sigma_k = 0, k \neq 1$ $h_1 = 2\text{m}$, $h_k = 0.1\text{m}$,$k \neq 1$

Table 5.1: Table of examples considered in Section 5.1.

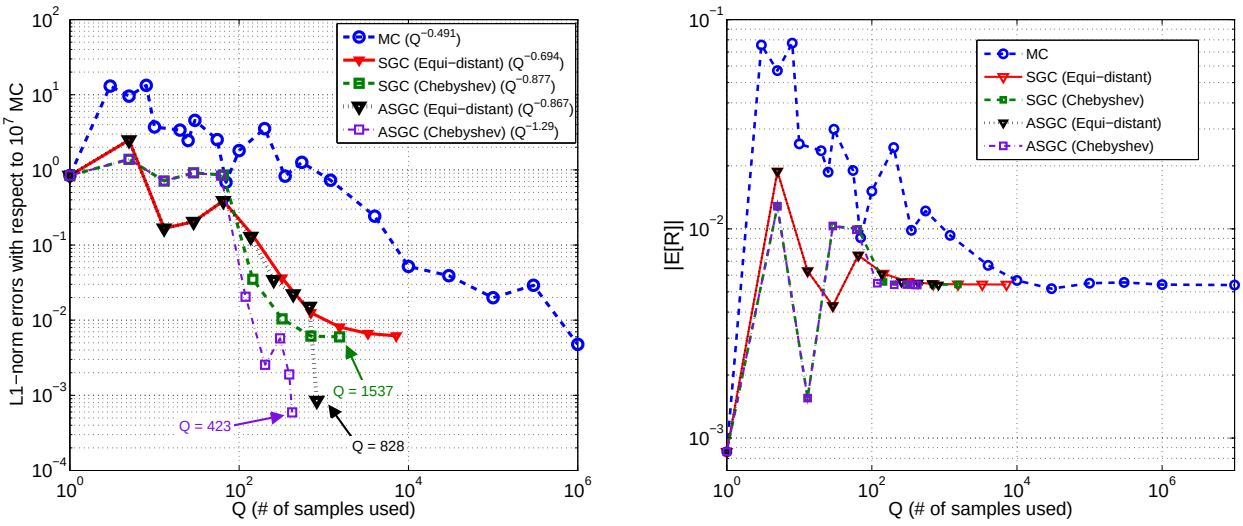

(a) (b)

Figure 5.3: (a) Error convergence for Example 1 of Section 5.1 for non-adaptive (SGC) and adaptive (ASGC) methods for increasing levels d. (b) $|E[R]|$ estimates corresponding to the curves in (a).

example we consider a case where each individual RV and $p-$tuple combinations of RVs contribute significantly to the target function R, where p corresponds to the component orders in (4.21). In Figure 5.4a the error convergence for MC sampling, ASGC and HDMR+ASGC are depicted. The ASGC solution was applied with Chebyshev nodes, with a threshold parameter $t_e = 0$, therefore it is indeed a non-adaptive solution (SGC). The markers on the ASGC curve denote errors for increasing levels d, as a function of the nodes (Q) used in the sparse grid. Note that the error attained at level $d = 5$, using 4,865 samples, is much lower than the MC sampling would attain with 10^6 samples. The HDMR+ASGC curve on the other hand depicts the errors with increasing component orders p, while keeping $d_{max} = 5$ in the algorithm in Section 4.4.1, as a function of Q. The HDMR error indicator was selected $\theta = 0$, and $p_{max} = N = 6$, so that the decomposition in (4.21) does not make any component elimination, and at order $p_{max} = N = 6$ completely recovers the ASGC solution it was applied upon. In Figure 5.4b, component importance indicators $\eta_{\mathbf{u}}$ are depicted as a function of the index of the components $\mathbf{u}$. Note that for this example there are a total of 2^6 components in (4.21), and all $\eta_{\mathbf{u}}$ except for the $0th$ order term are depicted ($\eta_0 = 1$ always). It is obvious in Figure 5.4b that unlike the general use of HDMR+ASGC algorithm for dimensionality reduction, this example reveals a case where all components up to $p = 5$th order are quite important, and cannot be eliminated. This is also obvious in Figure 5.4a that the HDMR+ASGC error is quite high unless all components are included. Through Example 2, we have considered a case where the physics of the geometry and the RVs assumed therein do not allow adaptation along certain reduced dimensional subspaces of the $6-$dimensional space (Γ). It is in general the case in the K-Slabs problem in this section, that unless some RVs are deliberately made less-important, all permittivities and permeabilities are comparably important in the input reflection coefficient R.

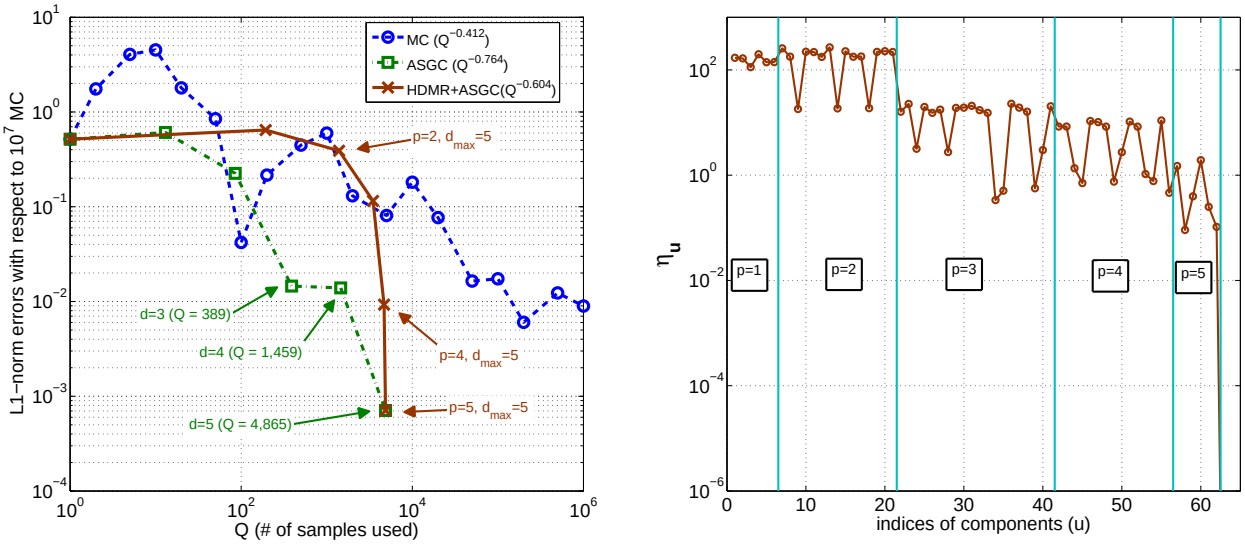

(a) (b)

Figure 5.4: (a) Error convergence for Example 2 of Section 5.1 for MC sampling, ASGC method for increasing levels d, and HDMR+ASGC for increasing component orders p. (b) $\eta_{\mathbf{u}}$ corresponding to the components of the HDMR expansion (HMDR+ASGC curve in (a)).

The following two examples (Examples 3 and 4) in this section will represent cases where we deliberately cast importance in Γ along certain axes, i.e. certain RVs are made more significant than others. The goal is to study how HDMR+ASGC and $h-$GSG methods perform compared to the MC sampling and QMC methods in high-dimensional problems.

Example 3 is the case of 10 dielectric slabs, thus the problem is $N = 20-$dimensional. In this example, the thickness of the first slab is $h_1 = 2$ meters, whereas the other nine slabs have thicknesses $h_2 = h_3 = ... = h_{10} = 0.5$ meters. Accordingly, for the purpose of creating a high-impedance first slab compared to the remaining nine slabs, all RVs are identical and uniform, except that the permeability of the first slab is much higher than other permeabilities: $\epsilon_1, \epsilon_2, .., \epsilon_{10}, \mu_2, \mu_3, .., \mu_{10} \sim U[1, 1.5]$, and $\mu_1 \sim U[20, 21]$. With such distinction of μ_1 from other RVs, and the first slab being four times thicker than the other slabs, the random problem becomes more fluctuating due to the uncertainty in μ_1 than other RVs. Figure 5.5 depicts the first norm errors for Example 3 with respect to 10^7 MC samples, which gives the reference value of $|E[R]| = 0.60437$. The error attained with MC with increasing sample size is depicted in both Figures 5.5a and 5.5b, whereas in Figure 5.5a the QMC methods (Sobol and Halton sequences) are compared to it, and the sparse grid methods are compared to it in Figure 5.5b. Note that both Sobol and Halton sequences attained a lower error than MC, Sobol has a convergence of $Q^{-0.637}$ and Halton has a convergence of $Q^{-0.657}$. On the other hand, HDMR+ASGC and $h-$GSG convergence are depicted in Figure 5.5b, both of them having significantly improved convergence than MC and QMC. The $h-$GSG sparse grid construction terminated after having used $Q = 855$ samples, where the tolerable error level parameter of $h-$GSG was $\epsilon_{tol} = 10^{-4}$. For the HDMR+ASGC, the parameter set was $\theta = 10^{-4}$, $d_{max} = 6$, and $t_e = 0.2\%$. The HDMR algorithm terminated after order $p = 2$, which used $Q = 692$ nodes and attained more than two orders of magnitude less error than the MC sampling with the similar Q. Indeed,

as stated in Section 4.4.1, the HDMR components are demonstrated with respect to their importance to the 20−dimensional overall function behavior in Figure 4.7. The vertical axis in Figure 4.7 depicts $|E[f_{\mathbf{u}}]|$ for each component function $\mathbf{u}$ in the HDMR expansion of Example 3. As noted again, components of dimensionality higher than two are very insignificant. This is revealed in the termination of the HDMR+ASGC method after order $p = 2$ in Figure 5.5b. The error that $h-$GSG attained with 855 samples is even lower, and represents a lower error than MC sampling with 10^6 samples has, as depicted in Figure 5.5b.

Example 4, the last example of this section, is a 50 dielectric slabs problem, which makes Γ 100−dimensional. Through this example we intend to demonstrate a high-dimensional case ($N = 100$) where the randomness in Γ is highly along a specific RV, which we expect to be ideal for interpolating with $h-$GSG. Our experience and related literature shows that the methods based on SGC, which is ASGC and HDMR+ASGC in our case, fail to attain better convergence than the MC and QMC with such high-dimensional examples. The difference of thicknesses of slabs is made very severe: $h_1 = 2$ meters, $h_2 = h_3 = ... = h_{50} = 0.1$ meters. Similar to Example 3, only the permeability of the first slab (μ_1) is assigned a large support and all other 99 RVs have much more restricted variation. This time we assume normal RVs, where the two arguments of a normal variable $N[.,.]$ stand for the mean and the standard deviation. The 99 restricted RVs are $\epsilon_1, \epsilon_2, .., \epsilon_{50}, \mu_2, \mu_3, .., \mu_{50} \sim N[1, 0.05]$, and $\mu_1 \sim N[20, 0.5]$. For this example, since the thicknesses, $h_k = 0.1$ meters, $k = 2, 3, .., 50$ are quite small compared to the smallest wavelength possible in the kth slab, appropriate discretization of each slab and enforcement of the boundary conditions at the interfaces require finer discretization than previous examples. Therefore, since the numerical solver is not the main contributor of this work, and not to make each deterministic solution of the problem time-consuming we skip using FDFD solver, but use an analytical solution for Example 4.

Figure 5.6a depicts the performance of QMC and sparse grid methods in Example 4 with respect to the reference solution. The reference solution in this case was obtained with 4×10^8 samples. Note in Figure 5.6a that the performance of both QMC sequences are slightly better than MC sampling, yet are not worse than the 20−dimensional case in Example 3. This is an indication that although we have a 100−dimensional problem in Example 4, the randomness in Γ is not significantly higher than in Example 3. Although we have chosen $Q = 4 \times 10^8$ samples for reference solution by the virtue of the analytical solution and up to $Q = 5 \times 10^5$ quasi-random samples to simulate with QMC methods, in Figure 5.6a the QMC methods did not achieve $O(1/Q)$ convergence. We believe this is due to the high-dimensional nature of Example 4. As expected, in Figure 5.6b the performance of $h-$GSG method is the best of all methods considered, and terminated at $Q = 2,029$ with $\epsilon_{tol} = 10^{-6}$. The fast decaying pattern in the error of $h-$GSG curve represent a super-index search along the axis of the μ_1 RV, for this example basically only that axis is very densely discretized due to its importance. The HDMR+ASGC on the other hand, terminates after order $p = 2$, and cannot draw nearer to the reference solution in a decent sparse grid size. This is mainly due to the fact, as explained earlier in Section 4.4.1, that the ASGC method at level d considers admissibility of all indices altogether, that satisfy $|\mathbf{i}|_1 = N + d$, thus unlike $h-$GSG cannot perform adaptivity along a single axis of Γ.

5.1.1 About Memory and Time Usages

Although we wrote the routines used in HDMR+ASGC and $h-$GSG methods as separate packages, we compare the memory and time usages of these individual methods in order to have an idea of their computational performances. For this, we select the Example 4 of Section 5.1 ($N = 100$ case) as test case. Since in this example we used an analytical solver, great majority of the monitored memory will be taken by the operations unique to sparse grid methods. Also, by avoiding the deterministic

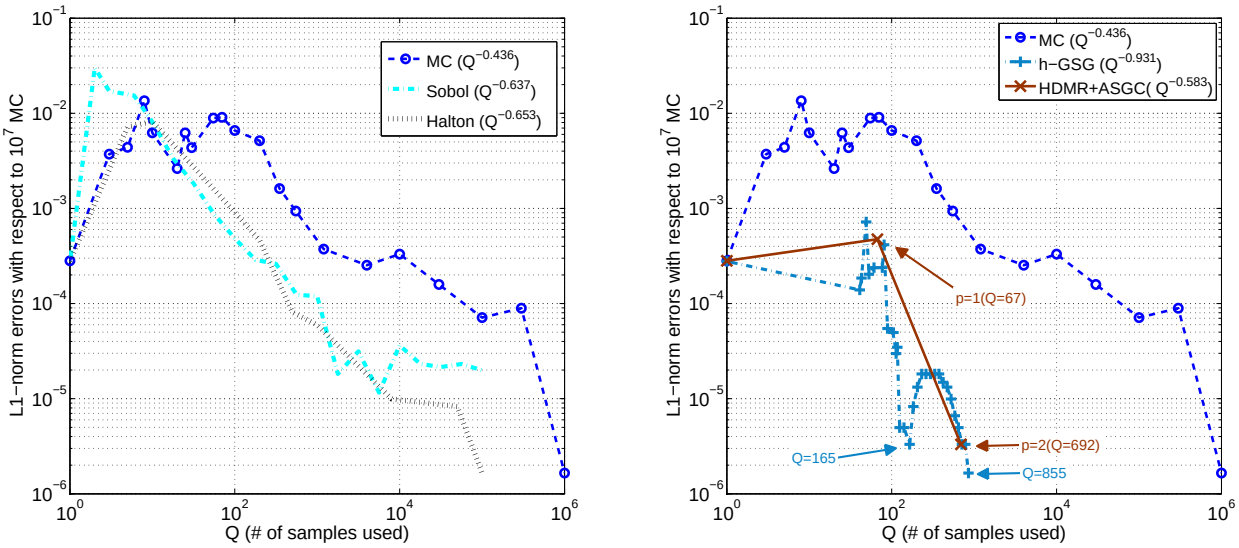

(a) (b)

Figure 5.5: (a) Error convergence for Example 3 ($N = 20$) of Section 5.1 for MC sampling, and QMC methods based on Sobol and Halton sequences. (b) Same comparison as in (a) made for $h-$GSG and HDMR+ASGC methods.

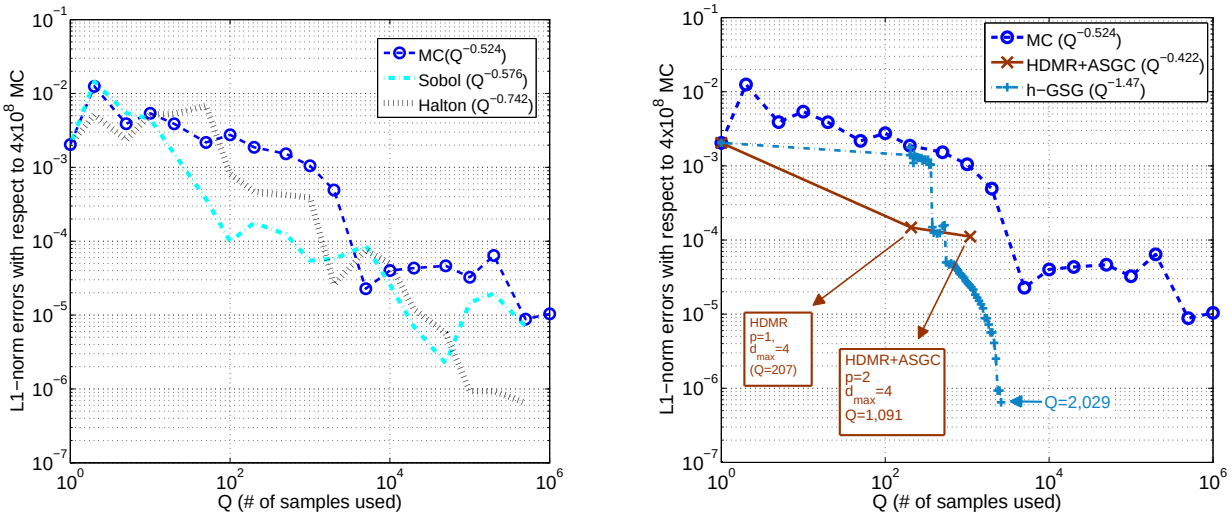

(a) (b)

Figure 5.6: (a) Error convergence for Example 4 ($N = 100$) of Section 5.1 for MC sampling, and QMC methods based on Sobol and Halton sequences. (b) Same comparison as in (a) made for $h-$GSG and HDMR+ASGC methods.

solver time by evaluating each sample analytically, we monitor the time incurred with sparse grids for high-dimensional problems.

Method	Samples Used (Q)	Peak Physical Memory	Total Time
MC	2,000	2.4 MB	0.54 sec.
HDMR+ASGC	1,091	5.3 MB	170 sec.
h-GSG	2,029	14 MB	77 sec.

Table 5.2: Memory and time usages in Example 4 of Section 5.1.

The HDMR+ASGC method, as depicted in Figure 5.6b, terminated after order $p = 2$ with a sample size of $Q = 1,091$. The peak physical memory taken during this execution was monitored as 5.3 MB and the method elapsed 170 seconds before termination. On the other hand, the $h-$GSG execution, which terminated after $Q = 2,029$, took 14 MB of peak physical memory and a total of 70 seconds. These are tabulated in Table 5.2. For both codes, it is a general trend that as Q monotonically increases, so does the memory in a *linear* fashion. We think this is due to the dynamic sized sets of objects that we store sparse grid nodes' attributes in. Each object in the set has attributes for its position in Γ, its super-index $\mathbf{i}$, and its sub-index $\mathbf{n}$. For holding these objects the standard *set* library of C++ is used. As a linear algebra package we used the *Eigen* library [35]. Similarly, for the MC sampling, the memory usage increases almost linearly with Q, and for the above considered problem, MC sampling with $Q = 2,000$ samples took 2.4 MB of physical memory.

The conclusion is, although the memory usage of sparse grid methods depend on how the operations with the nodes in Γ are performed, the above numbers suggest that for a $N = 100-$dimensional problem, the sparse grid methods take memories in the order of megabytes. In cases where the deterministic solver is a very heavy numerical solver, e.g. that involves inversion of large dense matrices, above values of memory and time in Table 5.2 will be negligible compared to those taken by the

solver. This will be verified in the upcoming applications through demonstration of error evolution with number of samples and with elapsed time.

5.1.2 Conclusions about the application

In summary, in this section we have considered a very simple one-dimensional reflection problem with a FDFD numerical solver, which also has a closed form solution. Although the problem and the deterministic solver are straightforward from a computational point of view, through different dielectric-layer scenarios the $N-$dimensional random problem has revealed the limitations in applicability of the sparse grid methods. Through Example 1 ($N = 2$) and Example 2 ($N = 6$), we have confirmed convergence with sparse grid better than the MC sampling for low-dimensionality. Example 3 ($N = 20$) and Example 4 ($N = 100$) were cases in which the randomness was deliberately cast into narrow sub-spaces and along individual axes of Γ, so that the HDMR+ASGC and $h-$GSG offer good convergence in high-dimensions. Although we have not shown such a case, a typical $N = 100-$dimensional problem in which the randomness is not along certain RVs, is prone to the "curse of dimensionality", and QMC methods are the only alternative to MC sampling in such high$-N$ cases [87].

5.2 A More Complicated Scattering Problem: Low-Grazing Angle Propagation Over a Random Surface

In this section we consider a scattering problem, in which the expected normalized total field is sought above a random surface and we restrict the problem to moderate dimensionality here. The fields propagate with low grazing angles to the surface, therefore the PE method from Chapters 2, 3 is used to govern the solution far from the source. As discussed before the method is subject to restrictions in surface roughness, domain parameters and the source [46]. To repeat (3.1), the PE in free space is

$$\frac{\partial}{\partial t}\psi(t,x) = \frac{i}{2k_o}\frac{\partial^2}{\partial x^2}\psi(t,x). \tag{5.6}$$

The problem geometry is depicted in Figure 5.7, where the surface profile $g(t)$ is randomly shaped and assumed perfectly conducting (PEC). The mean field, as a function of x at the observation range t_{obs} is sought due to a distributed source $s(x)$ excited from $t = 0$ plane. The numerical solution for a given surface profile is detailed in [61] and in [45], thus we will not go into details of the numerical solver, but rather focus on how the sparse grid methods perform.

The total field at (t, x) in Figure 5.7 is [45]

$$\psi_{tot}(t,x) = \psi_{FS}(t,x) + \psi_{sca}(t,x), \tag{5.7}$$

where ψ_{FS} is the solution obtained when propagated in free space with no boundaries, and ψ_{sca} is the field scattered by the PEC surface $g(t)$. These are [45], [61]

$$\psi_{FS}(t,x) = \int_{g_o}^{\infty} s(\eta)G_o(t,x;0,\eta)d\eta, \tag{5.8}$$

and

$$\psi_{sca}(t,x) = \frac{i}{2k_o}\int_0^t J(\xi)G_o(t,x;\xi,g(\xi))d\xi, \tag{5.9}$$

where $g_o := g(t = 0)$, $J(t)$ is a current induced on the surface, and $G_o(t,x;\xi,\eta)$ is the free-space Green's function for (5.6) in observation coordinates (t, x) and source

coordinates (ξ, η) [61]:

$$G_o(t, x; \xi, \eta) = \sqrt{\frac{k_o}{2\pi i(t-\xi)}} e^{i\frac{k_o}{2(t-\xi)}(x-\eta)^2}. \tag{5.10}$$

The excitation $s(x)$ may be a distributed source due to fields and media to the left of $t = 0$ plane. We will assume the source function to be a Gaussian-like distribution with mean height x_t:

$$s(x) = A_s e^{-ik_o x \sin(\alpha) - (x-x_t)^2/2\sigma_t^2}. \tag{5.11}$$

Angle $\alpha > 0$ (see Figure 5.7) is used to steer the excited beam with respect to the t axis, in order to control the interaction range of the waves with the surface $g(t)$. The current $J(t)$ is subject to the Volterra integral equation of second kind [61]:

$$\begin{aligned} J(t) &= -2\int_{g_o}^{\infty} s(\eta)\frac{\partial}{\partial \eta}\left(G_o(t, g(t); 0, \eta)\right) d\eta \\ &+ \sqrt{-i\frac{k_o}{2\pi}} \int_0^t J(\xi)\frac{g(x)-g(\xi)}{(x-\xi)^{3/2}} \exp\left[ik_o \frac{(g(x)-g(\xi))^2}{2(x-\xi)}\right] d\xi, \end{aligned} \tag{5.12}$$

which is obtained by imposing vertical derivative of the total field in (5.7), and by tending the observation elevation $x \to g(t)$ [61].

The Dirichlet boundary condition on the PEC surface at the source range ($t = 0$) is approximately met by assuming $\frac{x_t - g_o}{\sigma_t} > 4$. Given the surface $g(t)$, source $s(x)$ and the observation range t_{obs}, one solves (5.12), (5.9) and (5.8) to obtain the total field observed at range t_{obs}. The mean total field is obtained by random sampling of $g(t)$ and performing the mean value integration along each RV that define $g(t)$.

The ultimate purpose in this section is to calculate expected propagation factor (PF) in the presence of uncertain $g(t)$, *viz.*, $E[PF(t_{obs}, x)]$, where PF is defined as the total observed field normalized by the free-space field:

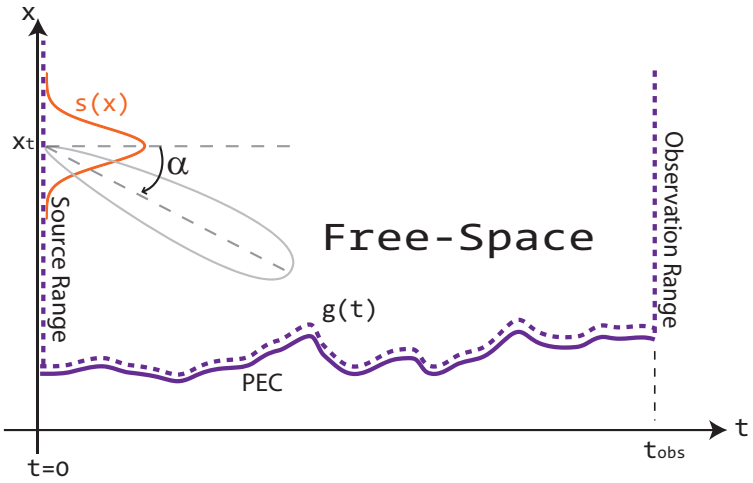

Figure 5.7: The computation domain for the scattering problem, denoted with the dashed lines.

$$PF = \left| \frac{\psi_{tot}(t_{obs}, x)}{\psi_{FS}(t_{obs}, x)} \right| . \tag{5.13}$$

We will consider independent uniform RVs to form several Gaussian shaped hills along range t. The range $[0, t_{obs}]$ is partitioned in B equal-length regions, and one random Gauss hill per region is appropriately generated:

$$g(t) = A_b \exp\left[-(t - \mu_b)^2 / 2\sigma_b^2\right], \tag{5.14}$$

$b = 1, 2, .., B$. Each Gaussian hill is randomized by 3 variables; μ_b controls center position, σ_b controls the width, and A_b controls the peak height of the bth hill. The center position and width of each hill is selected from uniform RV supports such that abrupt jumps at interfaces are prevented. The RVs for the bth hill are:

$$\begin{aligned} \mu_b &= U[\mu_b^{min}, \mu_b^{max}] \\ \sigma_b &= U[\sigma_b^{min}, \sigma_b^{max}] \\ A_b &= U[A_b^{min}, A_b^{max}]. \end{aligned} \tag{5.15}$$

Four realizations of a specific problem case is depicted in Figure 5.8. This is a scattering problem where the observation is at $t_{obs} = 420$ m, and $B = 7$. The parameters are chosen as $\mu_b = U[20b + 20]$ meters, $\sigma_b = U[5.5, 6.5]$ meters and $A_b = U[0.5, 1]$ meters, $b = 1, 2, .., 7$. Equal-length partitions along t are separated by dashed lines for sake of demonstration.

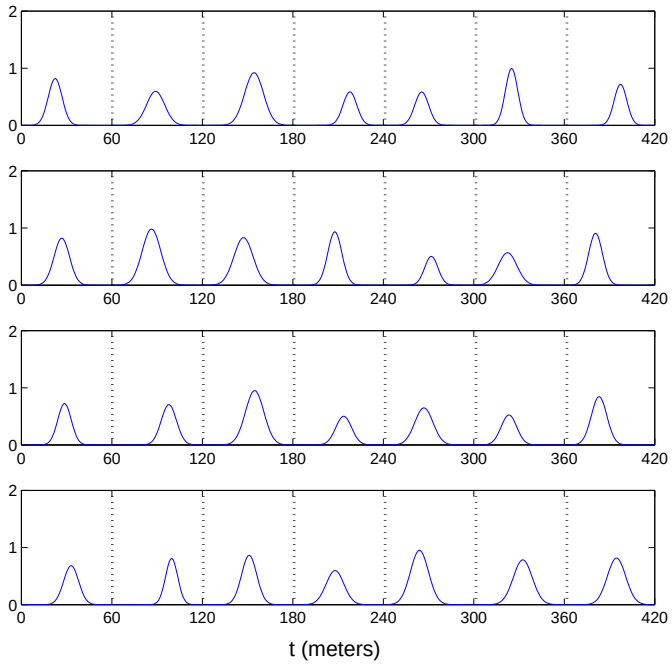

Figure 5.8: Four realizations of random profile g(t), $0 < t < t_{obs} = 420$ m, $B = 7$.

A concern about the applicability of (5.6) in radiowave propagation is about the angles of rays propagating with respect to the x axis in Figure 5.7, i.e. the maximum angle should not exceed 15^o with respect to t [46], also assumed in Chapters 2, 3.

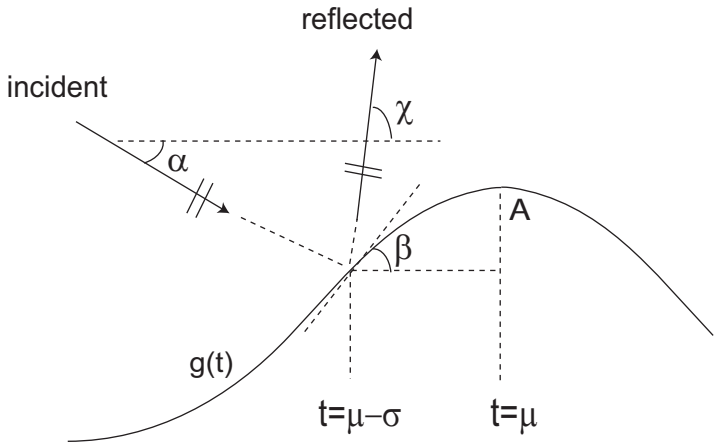

Figure 5.9: A ray incident on a Gaussian hill at its steepest point.

This implies that $\chi = \alpha + 2\beta < 15^o$ should be maintained (see Figure 5.9), where β is the slope of a Gaussian hill at its steepest location. It is trivial to see $\beta = \arctan(0.61A/\sigma)$. In order not to violate applicability of the numerical solver, we observe this restriction in the examples considered.

Once the independent RVs are realized, the total field $\psi_{tot}(t_{obs}, x)$ is calculated via the black-box deterministic solver of (5.12) [61]. Each realization of the $3B$ independent RVs is then used to determine the expected field. Since in this section we are concerned about a mean distribution along x, $E[PF(t_{obs}, x)]$, rather than a mean value as in Section 5.1, the first-norm error in this case is defined as a normalized integral:

$$Err_{L_1} = \frac{\int_0^{x_{max}} |h_{tar}(x) - h_{ref}(x)| \; dx}{\int_0^{x_{max}} |h_{ref}(x)| \; dx}, \tag{5.16}$$

where h_{tar} and h_{ref} are the computed target and the reference solutions, respectively. In other words, $h_{ref}(x)$ is the reference exact expectation $E[PF(t_{obs}, x)]$, and $h_{tar}(x)$

is the computed estimate to it. x_{max} is a maximum height that the computation domain is truncated at.

Example	B ($b = 1, .., B$)	N	t_{obs} (m)	α	μ_b(m)	σ_b(m)	A_b(m)
1	1	3	150	0^o	$U[50, 100]$	$U[10, 15]$	$U[0.5, 1]$
2	3	9	300	2.5^o	$100(b-1) + U[40, 60]$	$U[7, 8]$	$U[0.9, 1]$
3	7	21	420	5^o	$60(b-1) + U[25, 35]$	$U[7, 8]$	$U[0.9, 1]$

Table 5.3: Table of examples considered in Section 5.2.

In this section we will demonstrate three examples, which are tabulated in Table 5.3. In all examples the operating frequency is 1 GHz, the source height is $x_t = 3$ m, the source width is $\sigma_t = \lambda = 30$ cm, where λ is the free-space wavelength. Equi-distant nodes, along with local triangular basis functions from Equations (4.8) and (4.9) are used in all examples of this section. On the other hand, the reference distributions, $E[PF(t_{obs}, x)]$ were obtained from the MC sampling with 10^5 samples.

Example 1 is a single Gauss hill problem, thus it is $3-$dimensional. The reference solution is the expected PF observed at $t_{obs} = 150$m. The error convergence of the $h-$GSG and HDMR+ASGC are depicted in Figure 5.10a, and are compared to the convergence of the MC sampling. Note that the error attained with HDMR+ASGC with $Q = 339$ samples is lower than the MC sampling would attain with 10^4 samples. The $h-$GSG method renders smaller convergence rate than HDMR+ASGC, but is steeper than MC sampling. In Figure 5.10b, the PF is plotted in dB scale as a function of height. Note that both HDMR+ASGC estimate and the reference solution are indistinguishable. The estimate obtained with $Q = 300$ samples is also accurate, except that around 10 meters height it has approximately 2 dB discrepancy. In general, the examples in this section are subject to small dynamic range of errors in the $E[PF(t_{obs}, x)]$ estimates compared to the reference solution.

Example 2 is the case of three Gaussian hills randomly placed on the ground, making the problem $N = 9-$dimensional. Also a longer range of $t_{obs} = 300$m is chosen

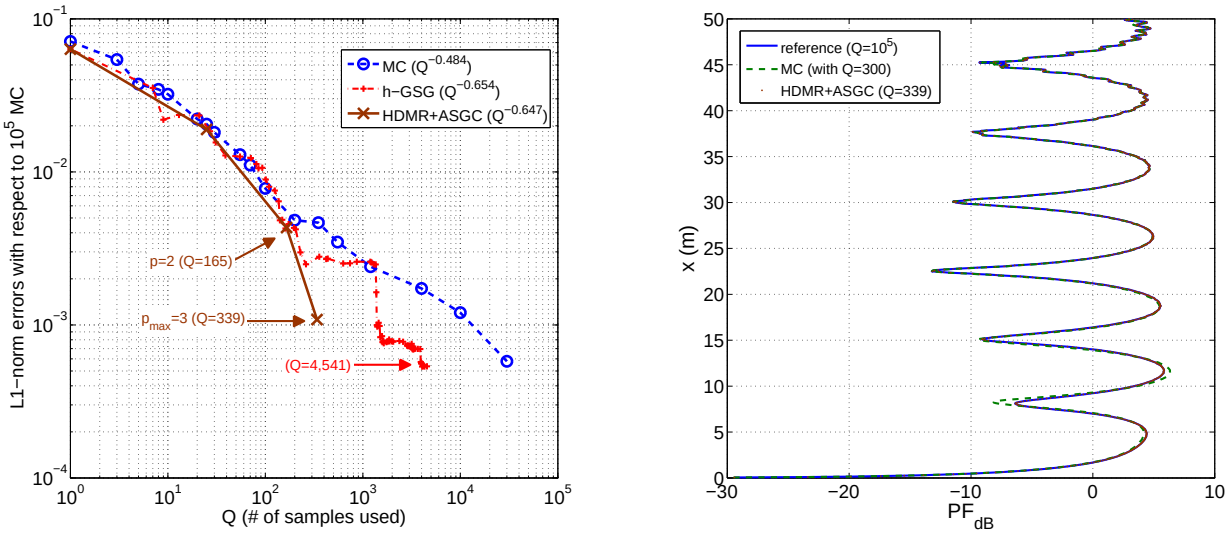

(a) (b)

Figure 5.10: (a) Error convergence for Example 1 ($N = 3$) of Section 5.2 for MC sampling, $h-$GSG and HDMR+ASGC. (b) Comparison of estimates for PF factor (in dB scale) with HDMR+ASGC and MC.

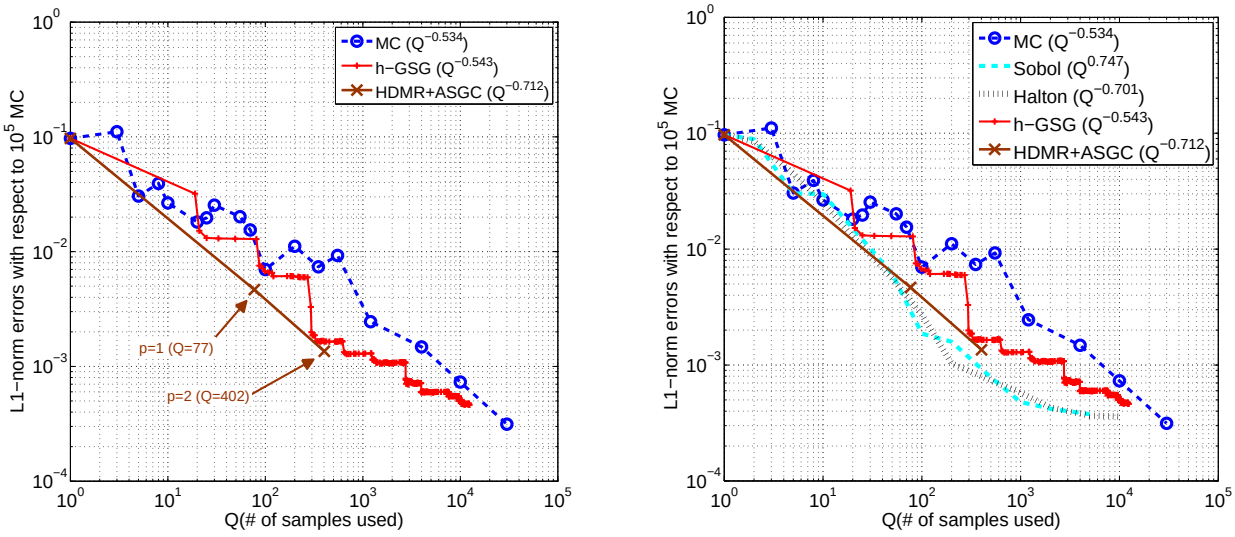

(a) (b)

Figure 5.11: (a) Error convergence for Example 2 ($N = 9$) of Section 5.2 for MC sampling, $h-$GSG and HDMR+ASGC. (b) QMC results with Sobol and Halton sequences superposed.

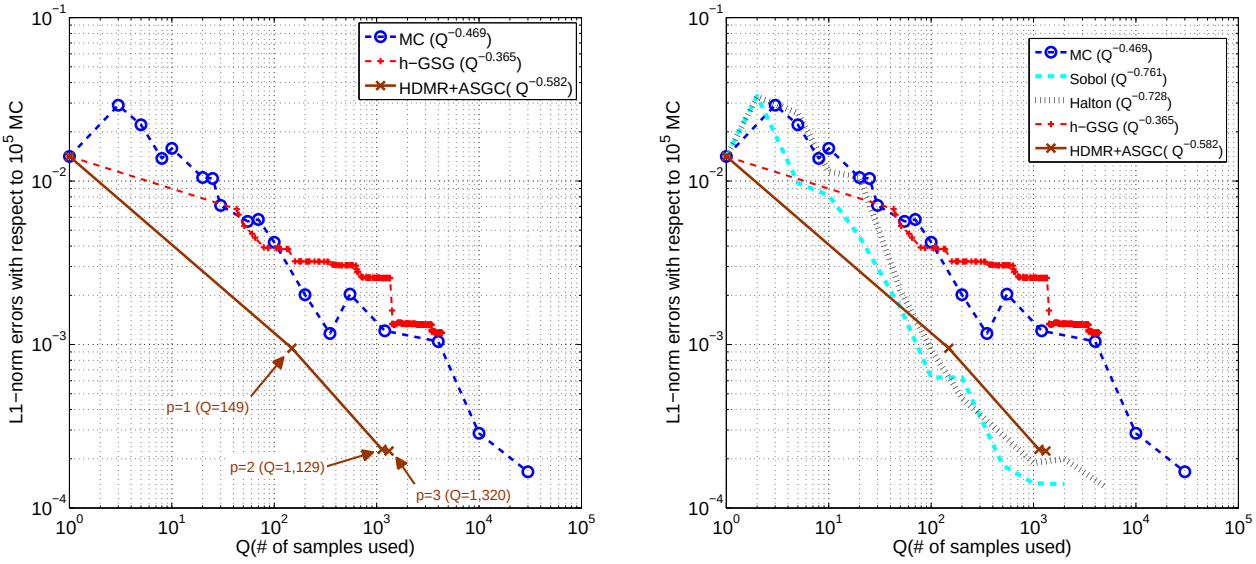

(a) (b)

Figure 5.12: (a) Error convergence for Example 3 ($N = 21$) of Section 5.2 for MC sampling, $h-$GSG and HDMR+ASGC. (b) QMC results with Sobol and Halton sequences superposed.

here, and the excitation is steered with $\alpha = 2.5^o$ with respect to t axis. Figure 5.11a depicts the convergence rates of the sparse grid methods. The HDMR+ASGC sparse grid construction terminated after $p = 2$ where it used $Q = 402$ samples, whereas the $h-$GSG algorithm with $\epsilon_{tol} = 10^{-8}$ terminated at $Q = 12,432$ samples. In Figure 5.11b the QMC methods based on Sobol and Halton sequences are superposed on to the existing sparse grid methods, and both have better convergence rates than MC sampling, $h-$GSG and HDMR+ASGC.

The last example is the case of seven hills randomly placed$-$a $N = 21-$dimensional problem, and observation at $t_{obs} = 420$m. As tabulated in Table 5.3, compared to Example 2, Example 3 has a mode restricted variation in each hill's mean position, μ_b. We aim to have a higher-dimensional case where some RVs are deliberately made more important than others. Also, the steer angle α is bigger, and the aim is to steer majority of the excited rays to interact with the first hill. This way, the other hills are less impinged by the rays, therefore RVs associated with those hills become less significant in the observed field. Figure 5.12a depicts the convergence performance of both sparse grid methods with respect to the reference solution. The HDMR+ASGC algorithm terminated after order $p = 3$ with $Q = 1,320$ samples, and has a steeper best-fit slope than the MC sampling. However, the $h-$GSG was not able to converge as fast, and resulted in more error than both MC sampling and HDMR+ASGC. This can only be explained by the fact that the randomness in the $21-$dimensional space (Γ) is not significant along individual axes of Γ, but is cast in local subspaces of Γ. In Figure 5.12b, the convergence of Sobol and Halton sequences are superposed, and they generally render as accurate as the HDMR+ASGC.

Finally, we depict the error convergence as a function of total time for Example 3. For this problem, the average time for the integral equation solver to evaluate each sample was monitored as 295 milliseconds. As expected and discussed in Section 5.1.1, comparison of Figure 5.12a with Figure 5.13 reveals that the total elapsed times are

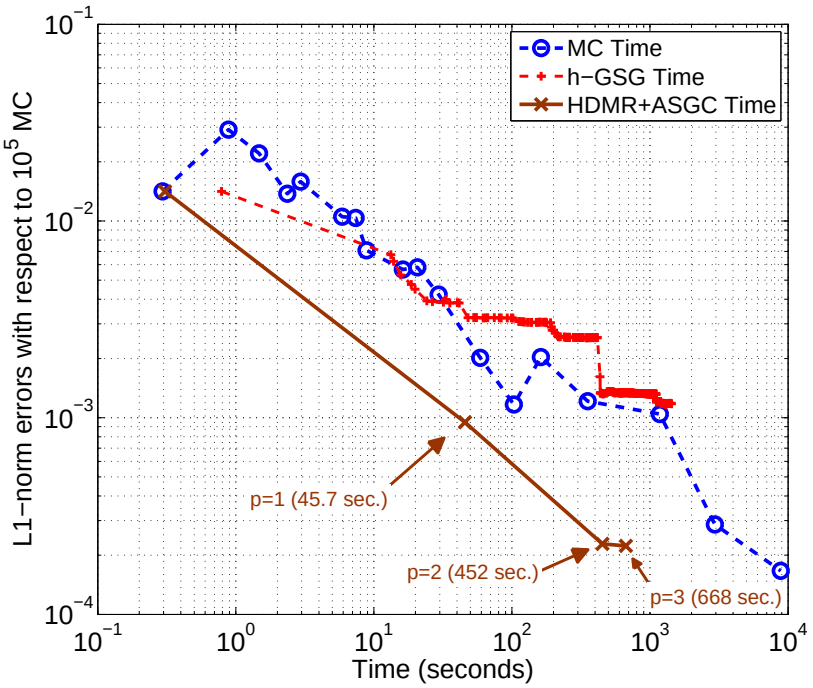

Figure 5.13: Error convergence for Example 3 ($N = 21$) of Section 5.2 for MC sampling, $h-$GSG and HDMR+ASGC as a function of total elapsed time in seconds.

dominated by the solver time rather than the negligible time taken by sparse grid algorithms.

5.2.1 Conclusions about the application

In this section, we have studied propagation over random surfaces artificially created as non-overlapping Gaussian hills along the propagation axis t. The results suggest that although the dimensionality N we consider is low-to-moderate, the randomness present in such scattering scenario is highly non-smooth, resulting in undesired performance with sparse grid methods. Accordingly, Figures 5.11b and 5.12b suggest that Sobol and Halton sequences are better candidates than both MC sampling and sparse grid methods we considered.

5.2.2 About the originally proposed rough surface scattering problem

The motivation for studying Section 5.2 was the more realistic problem of scattering from a rough surface with Gaussian statistics. However, the performance of the two adaptive sparse grid methods we considered are undesired in that case. One reason for that is the high$-N$ nature of the problem, where $N \gg 10$ RVs are used to numerically generate the surface as a random process [38]. More importantly, all RVs are equally significant in the statistical representation of a spatial surface point at range t, since this numerical surface generation uses combination of Discrete Fourier Transforms (DFTs) of normally distributed RVs [38, Appendix A]. Given the results in Section 5.2, and these facts about the originally proposed rough surface scattering problem, in the next section we consider another equally practical, smaller$-N$, and smoother-in-Γ propagation problem.

5.3 Application in Tropospheric Propagation: Field Estimation in Long-Range Uncertain Ducting Environments

The inverse problem of predicting refractive index profile from measured data has been an active research area, where popular prediction tools include evolutionary-type optimization algorithms and Markov-Chain-Monte-Carlo (MCMC) method [98, 99, 88]. Recently Grabner, et. al. have published their measured data that set a validated uncertainty model in terms of several random variables (RVs) [40, 88, 41], [102, Chapter 7]. Joint distribution of 5 RVs are validated and depicted in [102, Chapter 7], where it is assumed that each of these RVs is independent in moderate perturbations around locations of high probability in the probability distribution functions. Such an uncertainty in ducting model enables one to tackle field estimation problem, e.g. compute the mean-power available at desired receiver end. This estimation has conventionally been carried out for the propagation loss as a function of range using Monte Carlo (MC) sampling [27].

This section is reserved for the above $N = 5-$dimensional application which will demonstrate strength of sparse grid methods through a very realistic propagation scenario. The objective is to compute expected signal strength over flat Earth surface at ranges far from the transmitter location, where randomness is present due to uncertain refractive index of the atmosphere. The results that will be shown in this section are from [67].

The PE for inhomogeneous media in (2.3) governs the wave propagation, with the underlying assumptions made in previous chapters. Since this is a numerical problem to solve for long-range transmission the SSPE method from Section 2.3 is used as the deterministic solver here. Recall that the PE in atmosphere is:

$$\frac{\partial \psi}{\partial t} = \left[\frac{i}{2k_o} \frac{\partial^2}{\partial x^2} + ik_o \left(n(x) + \frac{x}{a_e} - 1 \right) \right] \psi. \tag{5.17}$$

The only difference of (5.17) from the PE given in (2.3) is that in this case the refractive index varies only as a function of elevation x, and assumed invariant along range t. As exemplified in Figure 2.1, such variation in ducting environments are accurately propagated with the SSPE solver.

5.3.1 Uncertain Refractivity Profile

Having an accurate predictor that can handle inhomogeneities along x as demonstrated in Section 2.3, we now consider the uncertain refractive index profile that we select for uncertainty quantification. The refractivity model from [102, Chapter 7] is:

$$N(x) = N_o + G_N x + \frac{dN}{2} \tanh \frac{2.96(x - h_o)}{dh}, \tag{5.18}$$

where N_o(N-units) is the nominal refractivity, G_N (N-units) is the gradient, dN(N-units) is the duct depth, h_o (meters) is the duct height, dh (meters) is the duct height and N-units is a measure of small changes in the true refractive index, $N =$

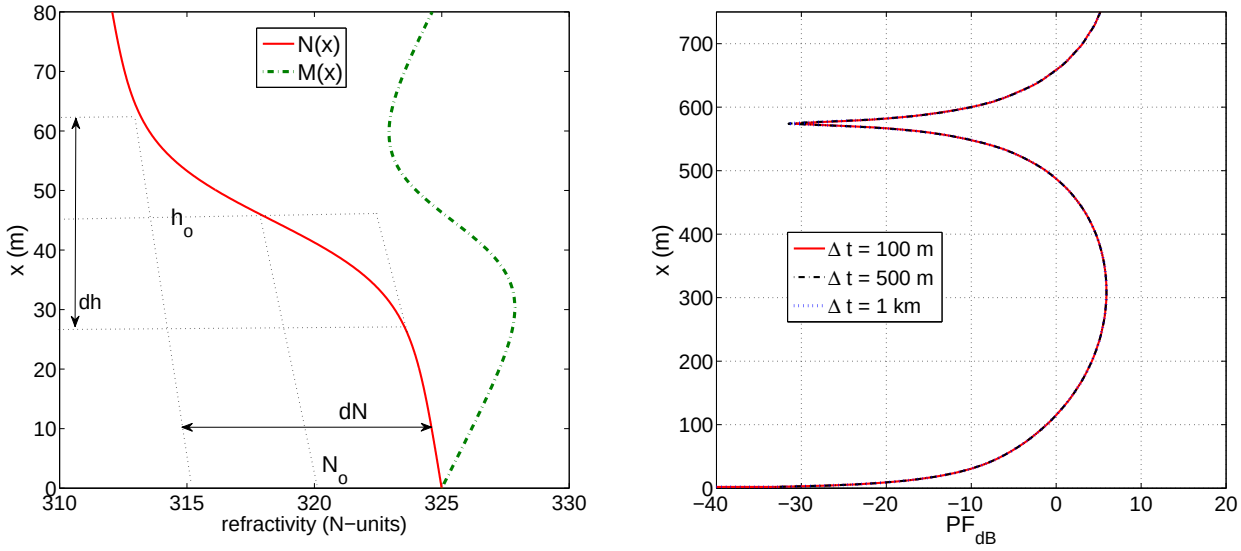

(a) (b)

Figure 5.14: (a) Refractive index profile according to (5.18), where $N_o = 320$ N-units, $G_N = -0.037$ N-units/m, $dN = -10$ N-units, $h_o = 45$ meters and $dh = 35$ meters. (b) Comparison of different range step sizes in computation of PF at 50 km, for the refractivity profile in (a).

$(n-1) \times 10^6$. The refractivity N is related to the often-used modified refractivity M through $N = M - 10^6 x/a_e$. To give a demonstration, a realization of N, M according to (5.18) is depicted in Figure 5.14a. The slopes of N at small and large heights are shown as dotted lines and are seen to be similar. From the joint cumulative distribution functions in [102, Chapter 7], we choose to assume supports of each of the 5 RVs to be independent and uniform. The nominal refractivity is a uniform RV $U[300, 340]$ N-units, G_N is $U[-0.057, -0.017]$ N-units/m, dN is $U[-7.5, 2.5]$ N-units, h_o is $U[20, 70]$ meters, and dh is $U[10, 60]$ meters. These supports were selected from where each probability distribution have their maxima in, out of the measured data in [102, Chapter 7], and where the cumulative distributions roughly increase linearly, so that uniform RV assumption makes sense and the assumed randomness constitutes the majority of the randomness present in the measured data.

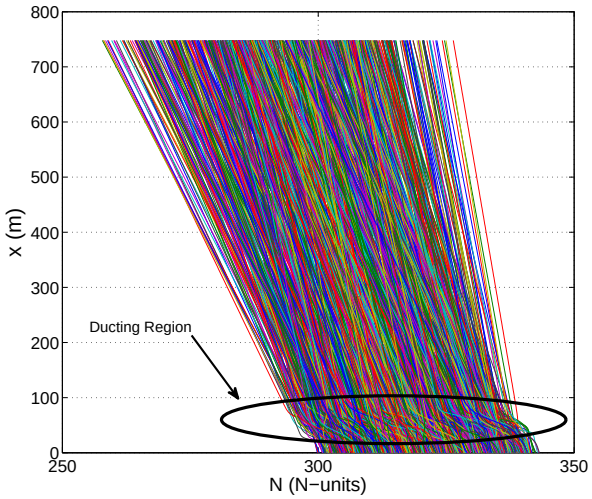

Figure 5.15: 2,000 realizations of the refractivity according to the uncertainties given in Section 5.3.1.

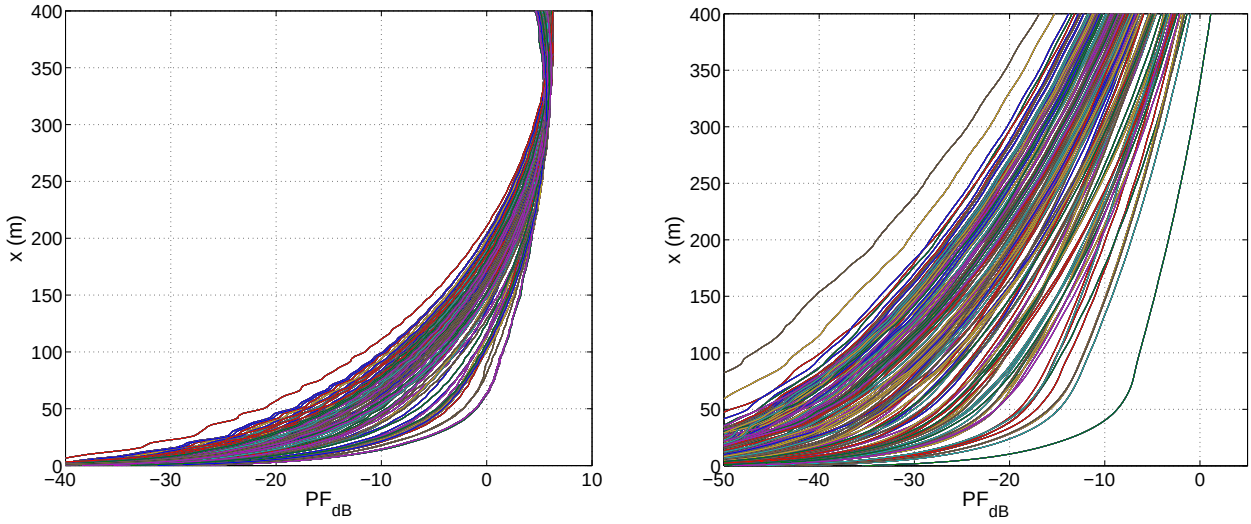

(a) (b)

Figure 5.16: PF_{dB} corresponding to the 2,000 relizations of N in Figure 5.15, (a) at $t_{obs} = 50$ km, (b) at $t_{obs} = 100$ km.

Since it is the purpose of this work to get expected propagation in an uncertain profile like above, for computational resources sake it is crucial to make the SSPE propagator as coarse as possible. For this purpose, in Figure 5.14b we depict the propagation factor (PF) for three different discretizations, for a sample refractivity profile as in Figure 5.14a, where the observation is at $t_{obs} = 50$ km, and the operating frequency is 300 MHz. It shows that the range step can be very coarse, and henceforth we fix $\Delta t = 1$ km for the model problems studied in this section.

To give an idea of the dynamic range of random refractivity variations, 2,000 independent realizations of the refractivity are shown in Figure 5.15, which corresponds to the uncertainty supports of the 5 RVs as given above. The PF variation at 50 km and 100 km observation ranges are shown in Figure 5.16a and Figure 5.16b, respectively. Note that the dynamic range of PF can vary over several orders of magnitude, unlike the case in Section 5.2.

5.3.2 Numerical Results

In this section we will demonstrate the strength of the HDMR+ASGC and $h-$GSG methods for the considered realistic propagation scenario. The source function, similar to (5.11), is excited at $t = 0$ as a Gaussian beam with height x_t and width σ_t:

$$\psi(0, x) =: s(x) = Ae^{-(x-x_t)^2/2\sigma_t^2}, \tag{5.19}$$

which leads to the following free-space propagated field received at (t, x), from (5.8) and [61]:

$$\psi_{FS}(t, x) = \frac{A\sigma_t}{\sqrt{\sigma_t^2 + it/k_o}} e^{-(x-x_t)^2/2\left(\sigma_t^2 + it/k_o\right)}. \tag{5.20}$$

We will demonstrate four case examples, where in all of them the operating frequency is 300 MHz, $x_t = 50$ meters, $\sigma_t = 2$ meters. This source width corresponds to around

7.5^o elevation beamwidth with respect to $t-$axis [37], which creates a fairly moderate spectral content span that is accurately propagated with the SSPE. In all examples the observation of field is between the Earth surface $x = 0$, and $x_{max} = 375$ meters. This height is safely above the elevations around which ducting phenomena occur. In the first two examples the observation range is $t_{obs} = 50$ km, and it is $t_{obs} = 100$ km in the last two examples. For Examples 1 and 2, the PF and the complex field are the targets at 50 km range, respectively. The same respective targets are analyzed at 100 km range in Examples 3 and 4. These examples are listed in Table 5.4.

Example	t_{obs} (km)	Target	SGC Nodes/Bases
1	50	$E[PF(50 \text{ km}, x; y)]$	Equi-Distant/Local Triangular
2	50	$E[\psi(50 \text{ km}, x; y)]$	Equi-Distant/Local Triangular
3	100	$E[PF(100 \text{ km}, x; y)]$	Chebyshev/Lagrange Poly.
4	100	$E[\psi(100 \text{ km}, x; y)]$	Equi-Distant/Local Triangular

Table 5.4: Table of examples considered in Section 5.3. Fixed parameters: $x_t = 50$ meters, $\sigma_t = 2$ meters, frequency= 300 MHz, $x_{max} = 375$ meters.

Figures 5.17a and 5.17b show the error convergence with respect to a reference solution, and the expected PF along height (x), respectively for Example 1. The reference solution for comparing each of the three depicted $E[PF(t_{obs}, x; y]$ estimates is obtained from MC simulation with $Q = 2 \times 10^6$ random samples, which is the case for all examples in this section. We feel that this sample size is large enough to accurately give the true expected power distribution.

The first norm error in the vertical axis of 5.17a (and in upcoming Figures 5.18a, 5.19a and 5.20a) was defined in (5.16). The sample sizes for MC sampling curve in Figure 5.17a, correspond to the error of each sample size case with respect to the reference. For the HDMR+ASGC method, note that with only $Q = 1,473$ samples the error attained is lower than the error MC sampling would attain with 5×10^5 samples. On the other hand, the $h-$GSG method attained less error than even with 10^6 MC samples, and used only 123 samples in the construction of the sparse grid.

Note that when the target function is the PF at 50 km range (Example 1), the dynamic range of output is not very large, hence in Figure 5.17b it is hard to visually conclude which method performed best. Indeed, at 100 m height, the discrepancy between $h-$GSG and MC with similar number of samples ($Q = 200$) is 0.45 dB.

Figures 5.18a and 5.18b are reserved for Example 2, where this time the target function is the complex received field, i.e. for estimation of $E[\psi(50\text{km}, x; y)]$. Both sparse grid methods outperformed the MC sampling, only with a few hundred samples each. In Figure 5.18b, the magnitude of several $E[\psi(t_{obs}, x; y)]$ estimates are depicted as a function of x. Different from the PF target case in Example 1, the discrepancies between sparse grid methods and MC sampling with comparable number of samples are quite severe. For instance, the expected received field estimated with $h-$GSG, which uses 397 samples is indistinguishable with the reference solution, whereas both 200 and 1,000 MC samples completely fail to give the right estimate, as shown in Figure 5.18a.

In order to further investigate the sparse grid performances, we consider in general more non-smooth target functions in Examples 3 and 4, where $t_{obs} = 100$ km. This is mainly due to interaction of the waves with uncertain duct for twice the range. For Example 3, the error convergence and converged estimates for PF are depicted in Figures 5.19a and 5.19b, respectively. Since a performance difference between selection of equi-distant nodes and Chebyshev nodes was observed only in Example 3, we are displaying here results with Chebyshev node sets (with Lagrange characteristic polynomial basis functions) for both $h-$GSG and ASGC, whereas in all other examples equi-distant nodes with local triangular basis functions were used. As can be seen from the dynamic ranges displayed in Figures 5.16a and 5.16b, Example 3 pertains to a more severely fluctuating case than Example 1. Therefore, the advantage of sparse grid estimates compared to MC sampling with similar Q is more evident in this example. For instance, at 50 m elevation this discrepancy is 2 dB, and at 200 m

elevation it is 0.9 dB, depicted in Figure 5.19b (whereas in Example 1 the discrepancy was 0.45 dB, depicted in Figure 5.17b). Note in Figure 5.19a that both $h-$GSG and HDMR+ASGC attains very small errors with less than 200 samples each, and the MC sampling attains similar error values with more than 10^5 samples.

Example 4 targets the complex field estimate at $t_{obs} = 100$ km $-E[\psi(100\text{km}, x; y)]$. The error convergence and field estimate magnitudes are depicted in Figures 5.20a and 5.20b, respectively. In this example, both sparse grid methods resulted in taking more samples compared to previous cases in general. This can be explained by the interaction with the uncertain duct for twice the range (100 km) than in Example 2. Nevertheless, the HDMR+ASGC is still much steeper in convergence compared to MC, and at $p = 3$ component order, using $Q = 728$ samples, attains less error than the MC sampling estimate of 10^6 samples. The $h-$GSG in this case however takes much more samples than in Example 2 for converging to the reference solution. From the statistical point of view this can be explained with the fact that as the important hyper-cubic regions of Γ are separated from the individual axes, dimension-adaptive methods like $h-$GSG render less accurate in such cases. This is where methods based on ASGC are favorable, as we witness in this problem. Although $h-$GSG uses orders of more samples than the HDMR+ASGC, it attains less error than the MC sampling estimate with 10^6 samples. In Figure 5.20b, it is clear that a MC estimate with $Q = 20,000$ samples is much more inaccurate than both sparse grid methods, whereas the best accuracy is attained with HDMR+ASGC with only 728 samples.

The QMC methods based on Sobol and Halton sequences are shown in Figure 5.21 for Examples 3 and 4. Note that although QMC methods offer faster convergence than MC sampling for Example 3, both sparse grid methods have significantly steeper convergence than QMC methods. For Example 4 on the other hand, which represented the worst convergence of sparse grids in this section, while HDMR+ASGC attains with 728 samples the same error level QMC methods would attain 10^4 sam-

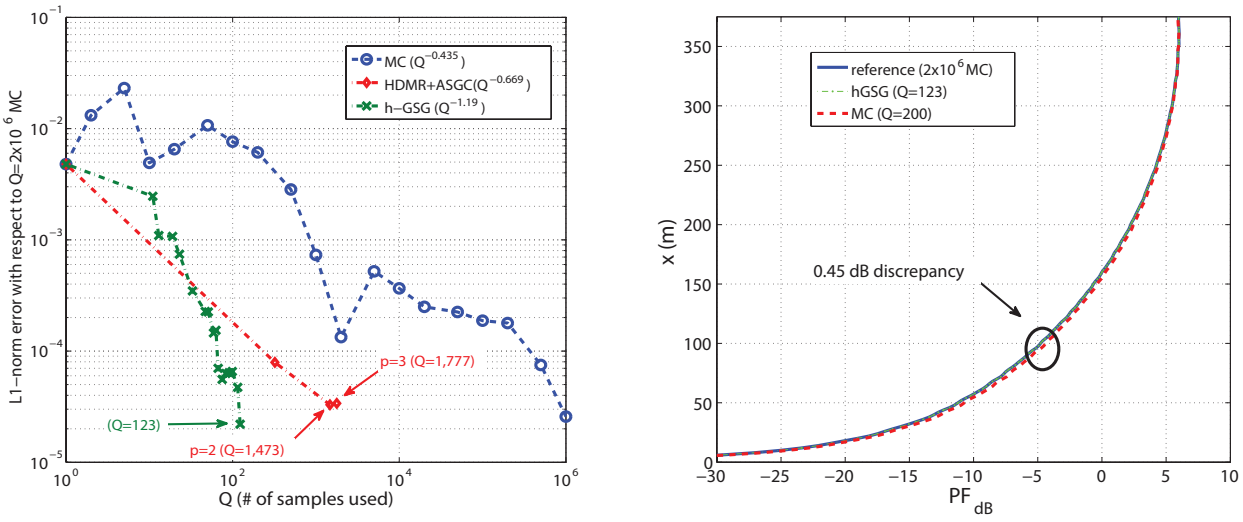

(a) (b)

Figure 5.17: (a) Error convergence for Example 1 of Section 5.3. (b) Expected field estimates for Example 1, $E[PF(50\text{km}, x; y)]$, corresponding to the convergence results in (a).

ples, $h-$GSG renders worse than QMC methods due to reasons explained in the discussion of Example 4.

Finally, the error convergence as a function of total elapsed time are depicted in Figures 5.22a and 5.22b for Example 3 and Example 4, respectively. The average computation time that SSPE solver takes to evaluate each sample was monitored as 54 milliseconds for both examples. In accordance with previous discussion on time, comparisons between Figures 5.19a and 5.22a, and between Figures 5.20a and 5.22b reveal that total computation time is dominated by the number of samples the SSPE solver evaluates. For instance, for the HDMR+ASGC curve in Figure 5.20a, the ratio of samples in levels $p = 3$ and $p = 2$ is $728/428 = 1.63$. Similar ratio of times in Figure 5.22b is $46.4/25.9 = 1.79$. Therefore, the computational cost other than that of evaluating the samples for this example is minor. As the deterministic solver gets more time consuming, the extra cost incurred in sparse grids will be less significant.

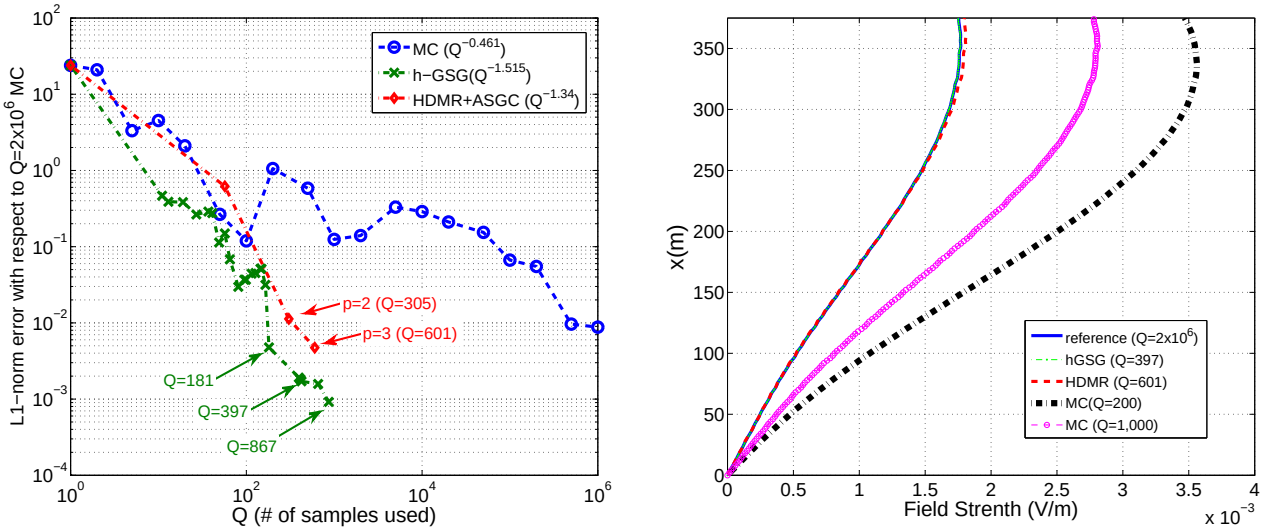

(a) (b)

Figure 5.18: (a) Error convergence for Example 2 of Section 5.3. (b) Expected field estimates Example 2, $|E[\psi(50\text{km}, x; y)]|$, corresponding to the convergence results in (a).

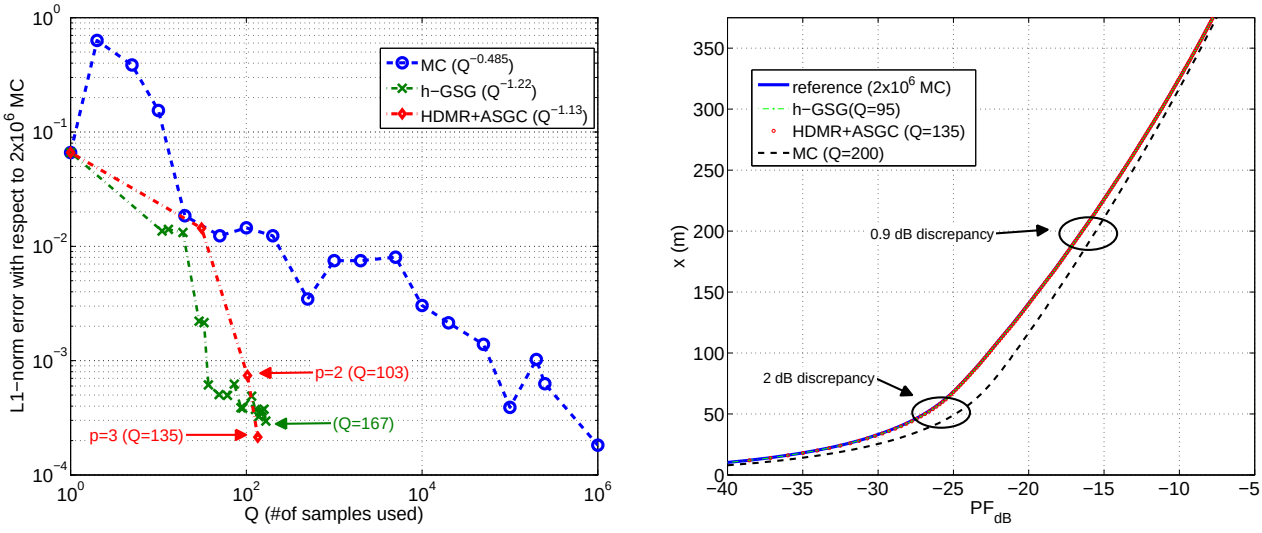

(a) (b)

Figure 5.19: (a) Error convergence for Example 3 of Section 5.3. (b) Expected PF estimates for Example 3, $|E[PF(100\text{km}, x; y)]|$, corresponding to the convergence results in (a).

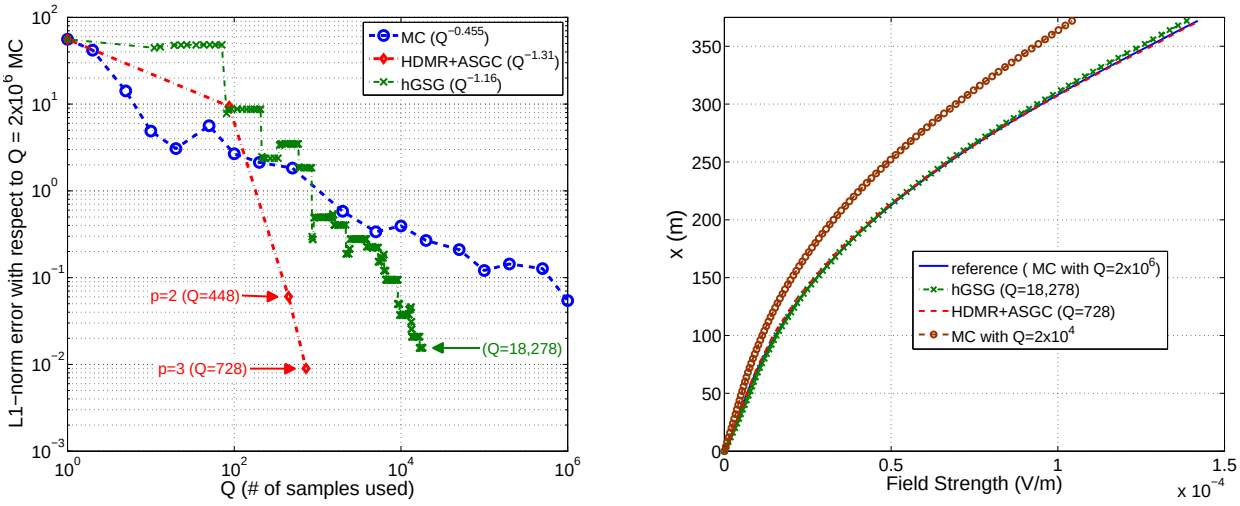

(a) (b)

Figure 5.20: (a) Error convergence for Example 4 of Section 5.3 (b) Expected field estimates for Example 4, $|E[\psi(100\text{km}, x; y)]|$, corresponding to the convergence results in (a).

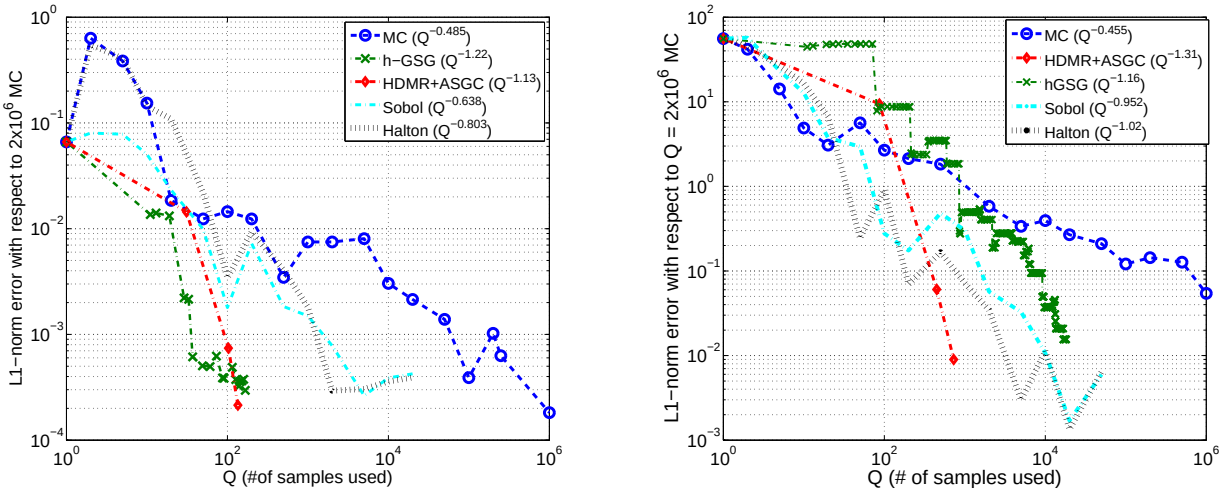

(a) (b)

Figure 5.21: QMC performances superposed on sparse grid performances for (a) Example 3 of Section 5.3, (b) Example 4 of Section 5.3.

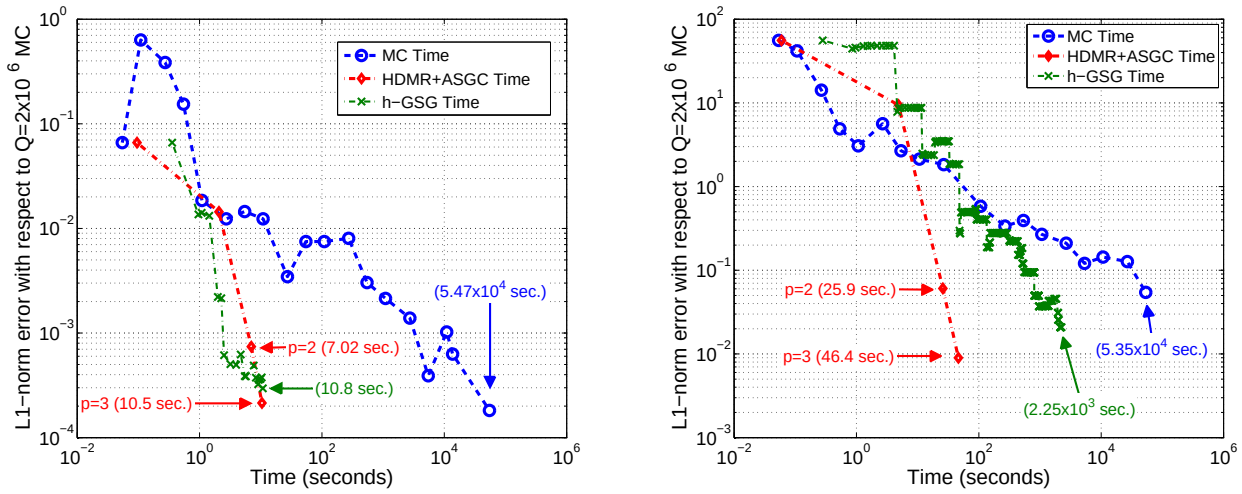

(a) (b)

Figure 5.22: Error convergence for MC sampling, $h-$GSG and HDMR+ASGC as a function of total elapsed time in seconds, for (a) Example 3 and (b) Example 4 of Section 5.3.

CHAPTER 6

SUMMARY AND CONCLUSIONS

We have studied techniques of increasing computational efficiency in electromagnetic propagation environments. We are interested in the propagation phenomena that utilizes the Parabolic Equation (PE) framework, and we have exploited both split-step Fourier methodology (SSPE) and finite-differences based methodology (FDPE) as the underlying numerical solvers.

The first aspect of this work is increased numerical efficiency in deterministic propagation environments. Through the formulations and results in Chapter 3, our contribution is in employment of fast approximate absorbing boundary conditions formulated for the half-open 2-D propagation environment that is solved with FDPE. Two approximations to the original DTBC, LDTBC and LDTBC_2, have given rise to a comparative study of different methods for domain truncation. Through a $3-$layer analysis in Section 3.3, we introduced a methodology for checking stability of a given LDTBC approximation, which is originally conditionally stable [2]. Although LDTBC is faster than DTBC, it also suffers exponential cost for boundary layer convolutions, and is highly prone to instabilities at long-ranges. On the other hand, the second approximation, LDTBC_2 has a linear cost as opposed to DTBC's exponential cost. Furthermore, we provided a stabilization strategy as re-located residues/poles, which ensured stability of LDTBC_2. At ranges far from the transmitter, PML and LDTBC_2 are the only choices for domain truncation. Since the low-grazing angle nature of the narrow-angle PE methods cause PML to deviate from the strong absorption it

provides for wider angles, for long-ranges we concluded that LDTBC_2 is a better alternative than PML.

The second aspect of the dissertation is the uncertainty quantification for propagation environments with uncertainty, where our effort is to use sampling based methods that converge faster than MC sampling. In Chapter 4 we have given review of sparse grid collocation (SGC) methods, while we adapted the notation from [94], [36] and [54]. For the interface of dimensionality reduction method (HDMR) with the adaptive SGC (ASGC), HDMR+ASGC, we have introduced and used *CompAdmit*, which has a less conservative "component admission" rule than the original rule given in [55]. For $h-$GSG method, we have followed [36].

The first application, reflection from $K-$Slabs is a 1-D scattering problem. Through this application we tested the SGC methods' performance with different node sets and interpolation bases. The $100-$dimensional example in Section 5.1 revealed strength of the $h-$GSG for problems where randomness is cast along certain axes of the random space.

As a simplified model to the scattering from rough surfaces problem, in Section 5.2 the random surface is formed from several Gaussian-shaped PEC hills along the propagation axis. Although we had more control of designing randomness compared to the case of rough surface scattering, this example is prone to the curse of dimensionality for moderate N. So is the rough surface scattering problem. For instance, the better convergence with QMC methods for a $N = 21$ case in Figure 5.12 revealed highly non-smooth nature of this problem, which prevented SGC methods from being a good alternative to MC sampling. Indeed, such a problem is an example of non-smooth function behavior that renders SGC methods less accurate, as witnessed by other works [87].

Lastly, we considered a quite realistic propagation problem with uncertainty, where randomness is represented in $N = 5$ RVs that constitute uncertain ducting

phenomena in the lower troposphere. The RVs are extracted from published measured data, and represents randomness observed during a season-long monitoring in Czech Republic [102]. We have showed that both HDMR+ASGC and $h-$GSG offered much steeper convergence than the MC sampling and QMC methods in this problem. The advantage of using sparse grids were more significant in cases where the target function is the complex field, than in PF (normalized power).

Through comparison of error convergence with respect to number of samples (Q) and with respect to total computation time, we conclude that as the deterministic solver becomes more time consuming, the cost incurred in sparse grid methods are insignificant. The same analogy is applicable to the memory usage.

As a future work, the dimension adaptive sparse grid methods, which is $h-$GSG in our case, need to be improved for better termination after convergence. In the current setting, in $h-$GSG it is not always assured that the sparse grid construction terminates after the optimum Q is reached. We needed to manually terminate the construction in some cases. Once this problem is solved, the HDMR+$h-$GSG interface then could be established.

Also, tackling of global optimization device design problems with high-dimensional parametric space is a promising field to apply sparse grids to. The authors in [100] have merged the HDMR with a genetic algorithm (GA) code for device optimization.

APPENDIX A

ANALYTICAL SOLUTION TO PROPAGATION ABOVE FLAT CONDUCTING SURFACE

The analytical solution to the one-way propagating wave in half-open free-space above perfectly conducting flat surface, for the PE in (3.1) is given in this section, and is adapted from [61]. This scenario is depicted in Figure A.1. We will utilize the free-space Green's function, given in (5.10):

$$G_o(t,x;\xi,\eta) = \sqrt{\frac{k_o}{2\pi i(t-\xi)}} e^{i\frac{k_o}{2(t-\xi)}(x-\eta)^2}, \tag{A.1}$$

for (t,x) are the observation coordinates and (ξ,η) are the source coordinates. For the scenario in Figure A.1, one can remove the PEC surface by the virtue of image theory, with assumption of a symmetric (with respect to t axis) second Gaussian excitation with opposite sign, we arrive at the field solution at an observation point $x>0$, $t>0$ as:

$$\psi(t,x) = \int_0^\infty \left(G(t,x;0,\eta) - G(t,x;0,-\eta)\right) s(\eta) d\eta. \tag{A.2}$$

In order to ensure that the excited source is confined in $x \in [0, x_h]$, where x_h is the elevation where the infinite domain is truncated at, in (3.42) we are interested in exciting a finite mode-sum approximate Gaussian source function:

$$s(x) = \begin{cases} A \sum_{m=1}^{K} \sin\left(\frac{m\pi x_t}{x_h}\right) \sin\left(\frac{m\pi x}{x_h}\right) e^{-m^2\pi^2\sigma_t^2/2x_h^2}, & 0 \le x \le x_h, \\ 0, & \text{elsewhere.} \end{cases} \tag{A.3}$$

Note that the modes in this source function satisfy the Dirichlet boundary conditions imposed by a parallel-plate waveguide with PEC walls at $x = 0$ and $x = x_h$, that are necessary in Chapter 3, *viz.*, $s(0) = 0,\ s(x_h) = 0$. Substituting (A.3) in (A.2), and combining the two terms in (A.2) into a single integration, we get:

$$\psi(t,x) = -A\sqrt{\frac{ik_o}{2\pi t}}e^{\frac{ik_o x^2}{2t}}\sum_{m=1}^{M}\left[\sin\left(\frac{m\pi x_t}{x_h}\right)e^{-\frac{m^2\pi^2\sigma_t^2}{2x_h^2}} \times \int_{-x_h}^{x_h} e^{i\frac{k_o\eta^2}{2t}}\sin\left(\frac{k_o x\eta}{t}\right)\sin\left(\frac{m\pi\eta}{x_h}\right)d\eta\right]. \tag{A.4}$$

Next, the integral in (A.4) can be manipulated as

$$\begin{aligned}&\int_{-x_h}^{x_h} e^{i\frac{k_o\eta^2}{2t}}\sin\left(\frac{k_o x\eta}{t}\right)\sin\left(\frac{m\pi\eta}{x_h}\right)d\eta \\ &= \int_{0}^{x_h} e^{i\frac{k_o\eta^2}{2t}}\left[\cos\left(\frac{k_o x\eta}{t}-\frac{m\pi\eta}{x_h}\right)-\cos\left(\frac{k_o x\eta}{t}+\frac{m\pi\eta}{x_h}\right)\right]d\eta.\end{aligned} \tag{A.5}$$

If one expands both $\cos(.)$ terms in (A.5) as exponentials, the following integral is essential for computing each exponential sub-term:

$$\begin{aligned}I_1 &:= \frac{1}{2}\int_0^{x_h} e^{i\left(\sqrt{\frac{k_0}{2t}}\eta\right)^2}e^{i\left(k_o\frac{x}{t}-m\frac{\pi}{x_h}\right)\eta}d\eta = \frac{1}{2}\int_0^{x_h} e^{i\left(\sqrt{\frac{k_o}{2t}}\eta\right)^2}e^{i\sqrt{\frac{k_o}{2t}}\eta\overbrace{\left(\sqrt{\frac{2k_o}{t}}x-\sqrt{\frac{2t}{k_o}}\frac{m\pi}{x_h}\right)}}d\eta \\ &= \frac{1}{2}\sqrt{\frac{\pi t}{k_o}}e^{-i\frac{\pi}{2}\beta_-^2}\int_{\beta_-}^{\beta_-+\sqrt{k_o x_h^2/\pi t}} e^{i\frac{\pi}{2}\gamma^2}d\gamma \\ &= \frac{1}{2}\sqrt{\frac{\pi t}{k_o}}e^{-i\frac{\pi}{2}\beta_-^2}\left[\mathcal{F}\left(\sqrt{k_o x_h^2/\pi t}+\beta_-\right)-\mathcal{F}\left(\beta_-\right)\right],\end{aligned} \tag{A.6}$$

where $\mathcal{F}(x) = \int_0^x e^{i\frac{\pi}{2}u^2}du$ is the Fresnel Integral and

$$\beta_\pm = \frac{1}{\sqrt{\pi}}\left(\sqrt{\frac{k_o x^2}{t}}\pm\sqrt{\frac{tm^2\pi^2}{k_o x_h^2}}\right). \tag{A.7}$$

The bracketed term in the exponent in (A.6) is set equal to $\sqrt{2\pi}\beta_-$, and the dummy variable used is $\gamma = \beta_- + \eta\sqrt{k_o/\pi t}$. Only with alternating signs, the rest of the exponential term integrals similar to (A.6), all of which appear in (A.5) become

$$\begin{aligned}
I_2 &:= \frac{1}{2}\int_0^{x_h} e^{i\left(\sqrt{\frac{k_0}{2t}}\eta\right)^2} e^{i\left(-k_o\frac{x}{t}+m\frac{\pi}{x_h}\right)\eta} d\eta \\
&= \frac{1}{2}\sqrt{\frac{\pi t}{k_o}} e^{-i\frac{\pi}{2}\beta_-^2}\left[\mathcal{F}\left(\sqrt{k_o x_h^2/\pi t} - \beta_-\right) - \mathcal{F}\left(-\beta_-\right)\right], \qquad \text{(A.8)} \\
I_3 &:= \frac{1}{2}\int_0^{x_h} e^{i\left(\sqrt{\frac{k_0}{2t}}\eta\right)^2} e^{i\left(k_o\frac{x}{t}+m\frac{\pi}{x_h}\right)\eta} d\eta \\
&= \frac{1}{2}\sqrt{\frac{\pi t}{k_o}} e^{-i\frac{\pi}{2}\beta_+^2}\left[\mathcal{F}\left(\sqrt{k_o x_h^2/\pi t} + \beta_+\right) - \mathcal{F}\left(\beta_+\right)\right], \qquad \text{(A.9)} \\
I_4 &:= \frac{1}{2}\int_0^{x_h} e^{i\left(\sqrt{\frac{k_0}{2t}}\eta\right)^2} e^{i\left(-k_o\frac{x}{t}-m\frac{\pi}{x_h}\right)\eta} d\eta \\
&= \frac{1}{2}\sqrt{\frac{\pi t}{k_o}} e^{-i\frac{\pi}{2}\beta_+^2}\left[\mathcal{F}\left(\sqrt{k_o x_h^2/\pi t} - \beta_+\right) - \mathcal{F}\left(-\beta_+\right)\right]. \qquad \text{(A.10)}
\end{aligned}$$

Finally, substituting Equations (A.6)–(A.10) in (A.5), (A.2) becomes

$$\begin{aligned}
\psi(t,x) &= -A\sqrt{\frac{i}{8}}\sum_{m=1}^{K}\sin\frac{m\pi x_t}{x_h} e^{-i\frac{m^2\pi^2 t}{2k_o x_h^2}} e^{-\frac{m^2\pi^2\sigma_t^2}{2x_h^2}} \\
&\times \left\{ e^{i\frac{m\pi x}{x_h}}\left[\mathcal{F}\left(\sqrt{\frac{k_o x_h^2}{\pi t}} + \beta_-\right) + \mathcal{F}\left(\sqrt{\frac{k_o x_h^2}{\pi t}} - \beta_-\right)\right]\right. \\
&- \left. e^{-i\frac{m\pi x}{x_h}}\left[\mathcal{F}\left(\sqrt{\frac{k_o x_h^2}{\pi t}} + \beta_+\right) + \mathcal{F}\left(\sqrt{\frac{k_o x_h^2}{\pi t}} - \beta_+\right)\right]\right\}. \qquad \text{(A.11)}
\end{aligned}$$

This completes the solution.

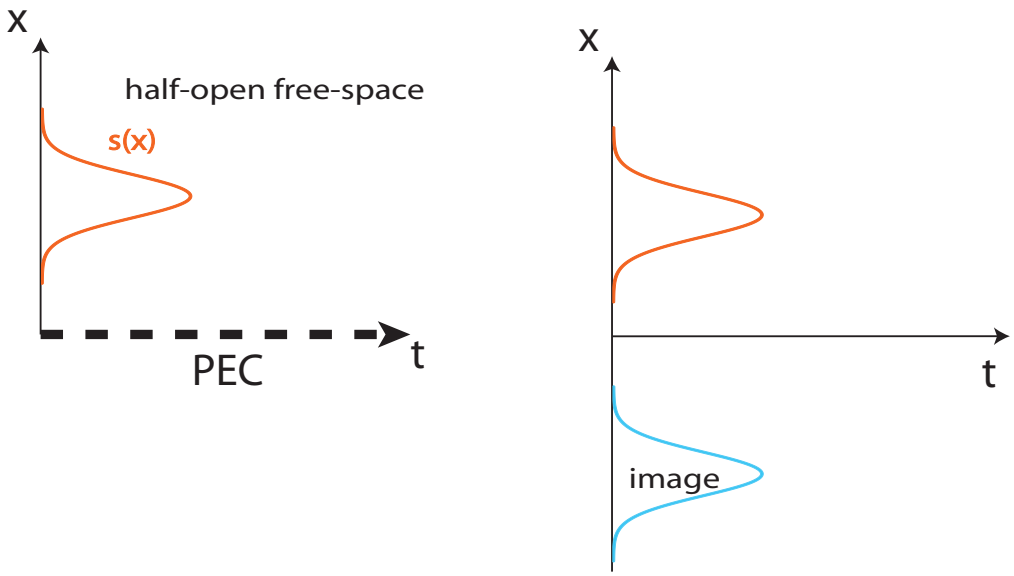

Figure A.1: The propagation environment, where x is the elevation axis and t is the range axis. $s(x)$ is the Gaussian source excited at $t = 0$, the right figure is equivalent of the left figure with PEC removed and an image source added in free-space.

APPENDIX B

BASIS FUNCTION INTEGRATIONS

In this section the basis function integrations performed in the construction of the sparse grids in Chapter 4 are given. We will use closed form expressions when applicable, and discuss how the numerical integrals are performed for other cases. To review, all combinations of the node sets, basis functions and RV distribution types are given in Table B.1.

Case	SGC Nodes/Bases	RV Distribution Type
1	Equi-Distant/Local Triangular	Uniform
2	Chebyshev/Lagrange	Uniform
3	Equi-Distant/Local Triangular	Gaussian
4	Chebyhsev/Lagrange	Gaussian

Table B.1: Combination of node sets, bases and distribution types used in the study.

Recall from Section 4.1 that $\mathcal{U}^i$ represents a uni-dimensional interpolation of order i, $\mathcal{H}^i$ represents the set of quadrature nodes used by $\mathcal{U}^i$, the cardinality of $\mathcal{H}^i$ is $q_i = 2^{i-1} + 1$, $i > 1$ and $q_1 = 1$.

In the construction of the SGC in (4.14) always tensor products of basis function integrals appear. We here consider only a uni-dimensional integral since all RVs are independent. The integral that we are concerned with in the most general sense is:

$$I_k^i = \int_a^b \zeta_k^i(Z)\rho(Y)dZ, \tag{B.1}$$

where $\zeta_k^i(Z)$ is the basis function used in the SGC method, which was given in Equations (4.9) and (4.12) for the local triangular basis functions and the Lagrange char-

acteristic polynomials in barycentric form, respectively for a variable in the unity interval: $Y \in [0,1]$. We here switch to a variable Z, which has a more general support: $Z \in [a,b]$. Recall from Section 4.1 that $k = 1,2,..,q_i$. Revisit Figure 4.1 for demonstration of nodes and basis functions for the case $i = 3$. Accordingly, below we repeat the nodes and basis functions that are defined in $[a,b]$, which originally were given in Section 4.1 for $[0,1]$. The equi-distant nodes that are used by $\mathcal{U}^i$ in interpolating a uni-dimensional function in $[a,b]$ are:

$$Z_k^i = \begin{cases} a + (b-a)\frac{k-1}{q_i-1} & ,k = 1,2,..,q_i \quad ,i > 1, \\ \frac{a+b}{2} & ,k = 1 \qquad ,i = 1, \end{cases} \tag{B.2}$$

and the corresponding local triangular basis functions are

$$\zeta_k^i(Z) = \begin{cases} 1 - \frac{q_i-1}{b-a}\left|Z - Z_k^i\right| & ,\text{if}\left|Z - Z_k^i\right| < \frac{b-a}{q_i-1}, \\ 0 & ,\text{otherwise.} \end{cases} \tag{B.3}$$

Similarly, the Chebyshev nodes are

$$Z_k^i = \begin{cases} \frac{a+b}{2} - \frac{b-a}{2}\cos\left(\frac{k-1}{q_i-1}\pi\right) & ,k = 1,2,..,q_i \quad ,i > 1, \\ \frac{a+b}{2} & ,k = 1 \qquad ,i = 1, \end{cases} \tag{B.4}$$

and the corresponding Lagrange basis functions in barycentric form are

$$\zeta_k^i(Z) = \begin{cases} \frac{\frac{\nu_k^i}{Z-Z_k^i}}{\sum_{l=1}^{q_i}\frac{\nu_l^i}{Z-Z_l^i}} & ,k = 1,2,..,q_i \quad ,i > 1, \\ 1 & ,k = 1 \qquad ,i = 1. \end{cases} \tag{B.5}$$

with $\zeta_k^i(Z_k^i) = 1$ and $\zeta_k^i(Z_l^i) = 0$ for $k \neq l$, and

$$\nu_k^i = (-1)^{q_i-k}\delta_k 2^{q_i-1} \quad , \; \delta_k = \begin{cases} 1/2 & ,k = 1 \text{ or } k = q_i, \\ 1 & ,\text{otherwise.} \end{cases} \tag{B.6}$$

The probability distribution function (pdf) in (B.1) has only appeared as for uniform RVs $U[.,.]$ and Gaussian RVs $N[.,.]$ in this study, therefore we here consider only these distributions.

Cases 1 and 2: Uniform Distribution

This section corresponds to a uniform RV assumed in (B.1), $Z = U[a, b]$, therefore

$$\rho(Z) = \frac{1}{b-a}. \tag{B.7}$$

Case 1 (Equi-distant nodes/Local triangular basis)

Note that this case corresponds to substitution of (B.7) and (B.3) in (B.1), which has a closed form solution:

$$I_k^i = \begin{cases} 1/2(q_i - 1), & k = 1 \text{ or } k = q_i, \quad i > 1, \\ 1/(q_i - 1), & k = 2, .., q_i - 1, \quad i > 1, \\ 1, & k = 1, \qquad i = 1. \end{cases} \tag{B.8}$$

Case 2 (Chebyshev nodes/Lagrangian basis)

The integral in this case can be formulated by substitution of (B.7) and (B.5) in (B.1). We are not able to solve this integration in a closed form, therefore we will perform numerical integration. The straightforward way is to discretize $[a, b]$ with several points, and apply a quadrature rule like trapezoidal rule, or Simpson's rule [3]. However, note that the integrand in this case is a $(q_i - 1)$th order polynomial. For instance, for the basis integration for the case of $i = 5$, the integrand is a 16th order polynomial in $[a, b]$. Proper discretization of such a function requires excessive number of quadrature points, thus results in slow computation. It should be re-stressed that uni-dimensional integrals of the form in (B.1) appear $N \times Q$ times in the coarse of the sparse grid construction in Section 4.1, where N is the dimensionality of the problem

and Q is the number of $N-$dimensional nodes used in the construction. Therefore, efficient computation of (B.1) is crucial.

For this purpose, we select not to discretize the real line for $Z \in [a, b]$, but compute the same integral on an alternative complex path by the virtue of Cauchy's integral theorem [12]. This is depicted in Figure B.1, where "Path 2" is the upper semi-circle that connects a to b, on which a complex variable is defined as:

$$V = \frac{a+b}{2} + \frac{b-a}{2} e^{j(\pi-\theta)}, \ 0 \leq \theta \leq \pi. \tag{B.9}$$

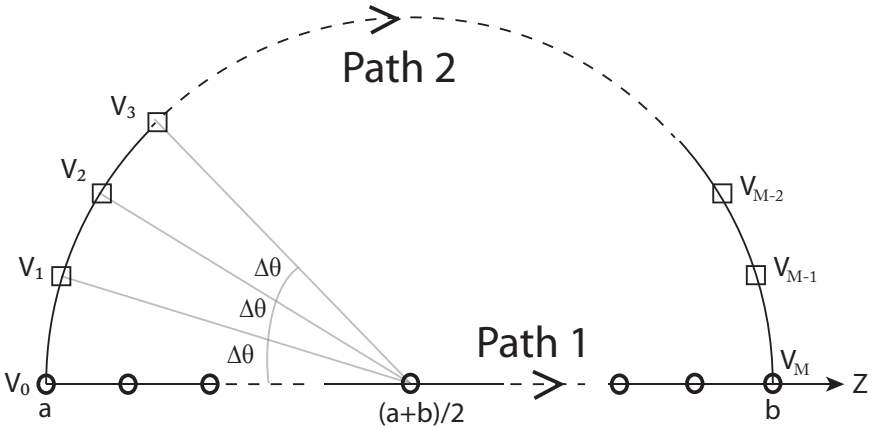

Figure B.1: The two integration paths connecting $Z = a$ to $Z = b$ used for integration of Lagrangian bases. "Path 1" discretizes $[a, b]$ on real axis, where "Path 2" discretizes the upper semi-circle in complex plane.

Note that unlike the rest of the dissertation, only here we use the complex $j = \sqrt{-1}$, not to confuse with the quadrature order i. $M+1$ points are selected on "Path 2", with equal angular increment $\Delta\theta = \pi/M$. Therefore, the points to be used for numerical integration are:

$$V_m = \tfrac{a+b}{2} + \tfrac{b-a}{2} e^{j\pi \frac{M-m}{M}}, \quad m = 0, 1, .., M, \tag{B.10}$$

and

$$\Delta V_m = V_{m+1} - V_m = \tfrac{b-a}{2} e^{j\pi \frac{M-m}{M}} \left(e^{-j\frac{\pi}{M}} - 1\right), \quad m = 0, 1, .., M-1. \tag{B.11}$$

Finally, we apply trapezoidal integration on "Path 2" while using V_m as the quadrature points, $m = 0, 1, .., M$. Substituting in (B.1) along with (B.7) results in:

$$I_k^i \approx \sum_{m=0}^{M-1} \Delta V_m \frac{\zeta_k^i(V_{m+1}) + \zeta_k^i(V_m)}{2(b-a)}, \tag{B.12}$$

where ζ_k^i are given in (B.5). Our investigation for an appropriate quadrature size M, given the Lagrange polynomial order q_i has revealed that $M \approx 20q_i$ computes the numerical integral with less than 1% relative error with respect to the exact value. Therefore, we keep the ratio of M/q_i as constant 20. Note that depending on this ratio (B.12) might have very small imaginary part, which we neglect.

Although we did not include it in this section, recall that the original form of the Lagrange characteristic polynomial was given in (4.11). For very small orders where the polynomial coefficients are not huge, $i \leq 3$, we indeed avoid using the barycentric form of (B.5), and use the original format in (4.11), thus perform an analytical integration of this low-order characteristic polynomial in (B.1).

Cases 3 and 4: Gaussian Distribution

This section corresponds to a Gaussian RV assumed in (B.1), $Z = N[\mu, \sigma]$, where μ is the mean and σ is the standard deviation. Since this distribution has infinite support, we inevitably truncate it at several σ away from μ. As a rule of thumb, given μ and σ, we assign support ends $a = \mu - 5\sigma$, $b = \mu + 5\sigma$, and truncate the

support of the RV at $[a, b]$. With such truncation, the basis function integral in (B.1) is also valid for this section. The pdf of the variable is

$$\rho(Z) = \frac{e^{-(Z-\mu)^2/2\sigma^2}}{\sqrt{2\pi}\sigma}. \tag{B.13}$$

Case 3 (Equi-distant nodes/Local triangular basis)

This case corresponds to substitution of (B.13) and (B.3) in (B.1), for which we will show the closed form solution. For brevity, we will separately consider two integrals, one integral for $k = 1$ and $k = q_i$, and one integral for $k = 2, 3, .., q_i - 1$. Since the equi-distant nodes are considered here, let the increment between successive nodes be $\Delta^i = (b - a)/(q_i - 1)$. For $k = 1$, the basis integral becomes:

$$I_1^i = \int_a^{a+\Delta^i} \left[1 - \frac{Z-a}{\Delta^i}\right] \frac{e^{-(Z-\mu)^2/2\sigma^2}}{\sqrt{2\pi}\sigma} dZ. \tag{B.14}$$

Now two integrals that will be beneficial in later steps are given below:

$$\begin{aligned} U_1 &:= \int_c^d \frac{e^{-(Z-\mu)^2/2\sigma^2}}{\sqrt{2\pi}\sigma} dZ = \frac{1}{2}\left[\text{erf}\left(\frac{\mu - c}{\sqrt{2}\sigma}\right) - \text{erf}\left(\frac{\mu - d}{\sqrt{2}\sigma}\right)\right], \\ U_2 &:= \int_c^d Z \frac{e^{-(Z-\mu)^2/2/\sigma^2}}{\sqrt{2\pi}\sigma} dZ = \frac{\sigma}{\sqrt{2\pi}}\left[e^{-(d-\mu)^2/2\sigma^2} - e^{-(c-\mu)^2/2\sigma^2}\right] + \mu U_1, \end{aligned} \tag{B.15}$$

where the error function is defined as $\text{erf}(x) = \frac{2}{\sqrt{\pi}} \int_0^x e^{-u^2} du$. Going back to the basis integration, substitution of (B.15) in (B.14) results in:

$$\begin{aligned} I_1^i &= \frac{1}{2}\left(1 + \frac{a-\mu}{\Delta^i}\right) . \left[\text{erf}\left(\frac{\mu - a}{\sqrt{2}\sigma}\right) - \text{erf}\left(\frac{\mu - a - \Delta^i}{\sqrt{2}\sigma}\right)\right] \\ &+ \frac{\sigma}{\Delta^i\sqrt{2\pi}}\left[e^{-(\mu-a-\Delta^i)^2/2\sigma^2} - e^{-(\mu-a)^2/2\sigma^2}\right]. \end{aligned} \tag{B.16}$$

Similarly, due to even symmetry both in the Gaussian pdf and in the triangular basis function, $k = q_i$ and $k = 1$ result in exactly the same basis integral in (B.1). Therefore, we readily have

$$I^i_{q_i} = I^i_1. \tag{B.17}$$

For the remaining indices, $k = 2, 3, .., q_i - 1$, the corresponding basis functions in (B.3) and the Gaussian pdf in (B.13) are substituted in (B.1), to get:

$$\begin{aligned} I^i_k &= \int_{Z^i_k - \Delta^i}^{Z^i_k} \left(\frac{Z - Z^i_k}{\Delta^i} - 1 \right) \frac{e^{-(Z-\mu)^2/2\sigma^2}}{\sqrt{2\pi}\sigma} dZ \\ &+ \int_{Z^i_k}^{Z^i_k + \Delta^i} \left(1 - \frac{Z - Z^i_k}{\Delta^i} \right) \frac{e^{-(Z-\mu)^2/2\sigma^2}}{\sqrt{2\pi}\sigma} dZ. \end{aligned} \tag{B.18}$$

Similar to previous case, the integrals U_1 and U_2 from (B.15) can be used to simplify above solution, which results in:

$$\begin{aligned} I^i_k &= \frac{\sigma}{\Delta^i\sqrt{2\pi}} \left[-2e^{-(\mu - Z^i_k)^2/2\sigma^2} + e^{-(\mu - Z^i_k + \Delta^i)^2/2\sigma^2} + e^{-(\mu - Z^i_k - \Delta^i)^2/2\sigma^2} \right] \\ &+ \frac{-\mu + Z^i_k}{\Delta^i} \text{erf}\left(\frac{\mu - Z^i_k}{\sqrt{2}\sigma} \right) \\ &+ \frac{1}{2} \left(1 + \frac{\mu - Z^i_k}{\Delta^i} \right) \text{erf}\left(\frac{\mu - Z^i_k + \Delta^i}{\sqrt{2}\sigma} \right) \\ &+ \frac{1}{2} \left(-1 + \frac{\mu - Z^i_k}{\Delta^i} \right) \text{erf}\left(\frac{\mu - Z^i_k - \Delta^i}{\sqrt{2}\sigma} \right), k = 2, 3, .., q_i - 1. \end{aligned} \tag{B.19}$$

Equations (B.19), (B.17) and (B.16) complete the solution for Case 3, Z^i_k are given in (B.2).

Case 4 (Chebyshev nodes/Lagrangian basis)

This case corresponds to substitution of (B.5) and (B.13) in (B.1), which does not have a closed form solution. On the other hand, the Cauchy-integral approach we

used in Case 2 cannot be used here on the full semi-circle, because of the exponential weight function of the Gaussian RV present in this case. In other words, when the Gaussian pdf of (B.13) is evaluated at an arbitrary complex point V on the semicircle in Figure B.1, $V = \mu + re^{j\theta}$, where $r = (b-a)/2$ and $\mu = (b+a)/2$, it will be in the form:

$$\rho(V) = \frac{e^{-r^2 e^{2j\theta}/2\sigma^2}}{\sqrt{2\pi}\sigma}. \tag{B.20}$$

Clearly the real part of the exponent will be positive for $\pi/4 < \theta < 3\pi/4$. Therefore, in Figure B.2 we depict the path on the complex plane that is bent to ensure negative real part in the exponent below. We select a small angle $\epsilon = \pi/180$ radians to ensure this. This path can be discretized in different ways, where we discretize with equi-distant angular spacing ($\Delta\theta$) for sections S1 and S4 (on the semi-circle), and equi-distant radial distant discretizations on sections S2 and S3 (on the radial lines). Having such discretization of V_{m_s}, $m_s = 0, 1, .., M_s$, where V_{m_s} are points along the $s-$th section, $s = 1, 2, 3, 4$. The trapezoidal rule similar to in Case 2 approximates the basis integration:

$$I_k^i \approx \sum_{s=1}^{s=4} \sum_{m_s=0}^{M_s-1} \Delta V_{m_s} \frac{\zeta_k^i(V_{m_s+1}) e^{-(V_{m_s+1}-\mu)^2/2\sigma^2} + \zeta_k^i(V_{m_s}) e^{-(V_{m_s}-\mu)^2/2\sigma^2}}{2\sigma\sqrt{2\pi}}, \tag{B.21}$$

where ζ_k^i are given in (B.5).

Unlike in Case 2, we did not see a significant advantage of using the above Cauchy-integration in place of trapezoidal integration on the real line that discretizes $Z \in [a, b]$. This is probably due to the bending we applied to the original semi-circle, and the Lagrange basis function fluctuates fast on sections S2 and S3 in Figure B.2, therefore requires quite fine discretization. Nevertheless, we use (B.21) when Chebyshev nodes/Lagrangian bases are used for interpolating functions of RVs with

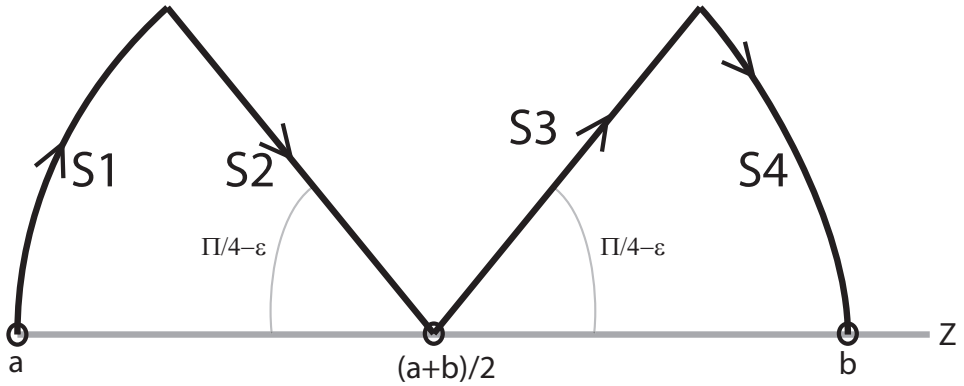

Figure B.2: The Cauchy-integral path that is bent for Case 4, for Gaussian weight function not to contain real exponent with positive sign.

Gaussian pdfs. As the constant ratio of number of trapezoidal integration points by q_i, we keep $(M_1 + M_2 + M_3 + M_4)/q_i = 500$.

BIBLIOGRAPHY

[1] Abramowitz, M., and Stegun, I. A. *Handbook of Mathematical Functions*. Dover, New York, NY, 1970.

[2] Arnold, A., Ehrhardt, M., and Sofronov, I. Discrete transparent boundary conditions for the Schrödinger equation: fast calculation, approximation, and stability. *Commun. Math. Sci. 1*, 3 (2003), 501–556.

[3] Atkinson, K.E. *An Introduction to Numerical Analysis*, II ed. John Wiley & Sons, 2008.

[4] Babin, S. M., Young, G. S., and Carton, J. A. A new model of the oceanic evaporation duct. *Journal of applied meteorology 36*, 3 (1997), 193–204.

[5] Baker, G. A. Jr., and Graves-Morris, P. *Padé Approximants*. Press Syndicate of University of Cambridge, New York, II Ed., 1996.

[6] Balanis, C.A. *Advanced Engineering Electromagnetics*. Wiley, New York, 1989.

[7] Baskakov, V. A., and Popov, A. V. Implementation of transparent boundaries for numerical solution of the Schrödinger equation. *Wave Motion 14*, 1 (January 1991), 123–128.

[8] Bean, B. R., and Thayer, G. D. Models of the atmospheric radio refractive index. *Proceedings of the IRE* (May 1959), 740–755.

[9] Beilenhoff, K., Heinrich, W., and Hartnagel, H.L. Improved finite-difference formulation in frequency domain for three-dimensional scattering problems. *J. Biomech. Eng. 40*, 3 (March 1992), 540–546.

[10] Berenger, J. P. A perfectly matched layer for the absorption of electromagnetic waves. *J. Comput. Phys. 114* (1994), 185–200.

[11] Berrut, J.P., and Trefethen, L.N. Barycentric Lagrange interpolation. *SIAM Review 46*, 3 (2004), 501–517.

[12] Brown, J.W., and Churchill, R.V. *Complex Variables and Applications*, VI ed. Mc Graw Hill, 1996.

[13] Clark, C.E. Importance sampling in Monte Carlo analyses. *Operations Research 9*, 5 (September-October 1961), 603–620.

[14] Clenshaw, C.W., and Curtis, A.R. A method for numerical integration on an automatic computer. *Numerische Mathematik 2* (1960), 197–205.

[15] Collino, F. Perfectly matched absorbing layers for the paraxial equation. *Journal of Computational Physics 131* (1997), 164–180.

[16] Correia, D., and Jin, J.-M. 3D-FDTD-PML analysis of left-handed metamaterials. *Microwave and Optical technology letters 40*, 3 (2004), 201–205.

[17] Dashen, R. Path integrals for waves in random media. *J. Math. Phys 20*, 894 (1979), 894–920.

[18] Dockery, G. D. Modeling electromagnetic wave propagation in the troposphere using the parabolic equation. *Antennas and Propagation, IEEE Transactions on 36*, 10 (1988), 1464–1470.

[19] Ehrhardt, M., and Arnold, A. Discrete transparent boundary conditions for the Schrödinger equation. *Riv. Mat. Univ. Parma 6* (2001), 57–108.

[20] Fishman, G.S. *Monte Carlo: Concepts, Algorithms and Applications*. Springer, New York, 1999.

[21] Foo, J., and Karniadakis, G.E. Multi-element probabilistic collocation method in high dimensions. *J. Comput. Phys 229* (2010), 1536–1557.

[22] Franceschetti, M. A random walk model of wave propagation. *IEEE Trans. on Antennas and Propagat. 49* (May 2004), 1304–1317.

[23] Gangnus, S.V., Matcher, S.J., and Meglinski, I.V. Monte Carlo modeling of polarized light propagation in biological tissues.

[24] Gedney, S. D. An anisotropic PML absorbing media for the FDTD simulation of fields in lossy and dispersive media. *Electromagnetics 16*, 4 (1996), 399–415.

[25] Gerstner, T., and Griebel, M. Numerical integration using sparse grids. *Numerical Algorithms 18* (1998), 209–232.

[26] Gerstner, T., and Griebel, M. Dimension–adaptive tensor–product quadrature. *Computing 71*, 1 (2003), 65–87.

[27] Gerstoft, P., Hodgkiss, W. S., Rogers, L. T., and Jablecki, M. Probability distribution of low-altitude propagation loss from radar sea clutter data. *Radio science 39*, 6 (2004).

[28] Gossard, E. E. Refractive index variance and its height distribution in different air masses. *Radio Science 12*, 1 (1977), 89–105.

[29] Griebel, M., and Holtz, M. Dimension-wise integration of high-dimensional functions with applications to finance. *J. Complexity 26* (2010), 455–489.

[30] Hadley, G. R. Wide-angle beam propagation using Padé approximant operators. *Optics Letters 17*, 20 (1992), 1426–1428.

[31] Halton, J.H., and Smith, G.B. Radical-inverse quasi-random point sequence. *Communications of the ACM 7*, 12 (Dec. 1964), 701–702.

[32] Higham, N.J. The numerical stability of barycentric Lagrange interpolation. *IMA J. of Numer. Anal. 24* (2004), 547–556.

[33] Ishimaru, A. *Wave Propagation and Scattering in Random Media*. IEEE Press, New York, 1999.

[34] J., Van R., Van der Donk, J., and Lagasse, P.E. Beam-propagation method: analysis and assessment. *JOSA 71*, 7 (1981), 803–810.

[35] Jacob, B., and Guennebaud, G. *Eigen : C++ template library for linear algebra. http://eigen.tuxfamily.org/*, 3.1.1 ed.

[36] Jakeman, J. D., and Roberts, S. G. Local and dimension adaptive stochastic collocation for uncertainty quantification. In *Sparse Grids and Applications*. Springer, 2013, pp. 181–203.

[37] Janaswamy, R. Radio wave propagation over a nonconstant immittance plane. *Radio Sci. 36*, 3 (May-June 2001), 387–405.

[38] Janaswamy, R. *Radiowave Propagation and Smart Antennas for Wireless Communications*, vol. 599. Springer, 2001.

[39] Janaswamy, R. Transitional probabilities for the 4-state random walk on a lattice. *J. Phys. A: Math. Theor. 41* (2008), 155306(11pp).

[40] Jicha, O., Pechac, P., Kvicera, V., and Grabner, M. On the uncertainty of refractivity height profile measurements. *Antennas and Wireless Propagation Letters, IEEE 10* (2011), 983–986.

[41] Jicha, Otakar, Pechac, Pavel, Kvicera, Vaclav, and Grabner, Martin. Estimation of the radio refractivity gradient from diffraction loss measurements.

[42] Keefe, L. Dispersive waves and PML performance for large-stencil differencing in the parabolic equation. *Antennas and Propagation, IEEE Transactions on 60*, 11 (2012), 5268–5277.

[43] Klimke, A., and Wohlmuth, B. Algorithm 847: SPINTERP: Piecewise multilinear hierarchical sparse grid interpolation in matlab. *ACM Trans. Math. Software 31*, 4 (December 2005), 561–579.

[44] Kuttler, J. R., and Dockery, G. D. Theoretical description of the parabolic approximation/Fourier split-step method of representing electromagnetic propagation in the troposphere. *Radio Science 26*, 2 (1991), 381–393.

[45] Lai, Z., and Janaswamy, R. Specular propagation over rough surfaces: numerical assessment of Uscinski and Staneks mean Greens function technique. *Waves in Random and Complex Media 16*, 2 (May 2006), 137–150.

[46] Levy, M. *Parabolic Equation Methods for Electromagnetic Wave Propagation.* IEE, London, 2000.

[47] Levy, M. F. Perfectly matched layer truncation for parabolic wave equation models. *Proc. R. Soc. Lond. A 457* (May 2001), 2609–2624.

[48] Li, P., Liu, F., Li, X., Pileggi, L.T., and Nassif, S.R. Modeling interconnect variability using efficient parametric model order reduction. vol. 2, Proc. of the Design, Automation and Test in Europe Conference and Exhibition (DATE05).

[49] Liang, F., Liu, C., and Carroll, R.J. *Advanced Markov Chain Monte Carlo Methods.* Wiley, Chichester, West Sussex, U.K., 2010.

[50] Liu, M., Gao, Z., and Hesthaven, J.S. Adaptive sparse grid algorithms with applications to electromagnetic scattering under uncertainty. *Appl. Numer. Math. 61* (2011), 24–37.

[51] Loeve, M.M. *Probability Theory.* Van Nostrand, New Jersey, 1963.

[52] Lorentz, G.G., Golitschek, M.V., and Makovoz, Y. *Constructive Approximation.* Springer, New York, 1996.

[53] Lv, Y.-G., Deng, Z.-S., and Liu, J. 3-d numerical study on the induced heating effects of embedded micro/nanoparticles on human body subject to external medical electromagnetic field. *NanoBioscience, IEEE Transactions on 4*, 4 (2005), 284–294.

[54] Ma, X., and Zabaras, N. An adaptive hierarchical sparse grid collocation algorithm for the solution of stochastic differential equations. *J. Comput. Phys*, 228 (2009), 3084–3113.

[55] Ma, X., and Zabaras, N. An adaptive high-dimensional stochastic model representation technique for the solution of stochastic partial differential equations. *J. Comput. Phys 229* (2010), 3884–3915.

[56] Martelly, R., and Janaswamy, R. An ADI-PE approach for modeling radio transmission loss in tunnels. *IEEE Trans. Antennas Propagat. 57*, 6 (June 2009), 1759–1770.

[57] Martelly, R., and Janaswamy, R. Modeling radio transmission loss in curved, branched and rough-walled tunnels with the ADI-PE method. *IEEE Trans. Antennas Propagat. 58*, 6 (June 2010), 2037–2045.

[58] McKay, M. D., Beckman, R.J., and Conover, W.J. A comparison of three methods for selecting values of input variables in the analysis of output from a computer code. *Technometrics 21*, 2 (May 1979), 239–245.

[59] Mittra, R, and Pekel, U. A new look at the Perfectly Matched Layer (PML) concept for the reflectionless absorption of electromagnetic waves. *Microwave and Guided Wave Letters, IEEE 5*, 3 (1995), 84–86.

[60] Morton, K. W., and Mayers, D. F. *Numerical Solution of Partial Differential Equations*, 2nd ed. Cambridge University Press, Cambridge, UK, 2008.

[61] Motta, M.J. Equivalent impedance of rough surface at low grazing angles. Master's thesis, Naval Potgraduate School, Monterey, CA, 1999.

[62] Niederreiter, H. *Random number generation and quasi-Monte Carlo methods*. Society for Industrial and Applied Mathematics, Philadelphia, 1992.

[63] Nobile, F., Tempone, R., and Webster, C.G. A sparse grid stochastic collocation method for partial differential equations with random input data. *SIAM J. Numer. Anal. 46*, 2309 (2008).

[64] Novak, E., and Ritter, K. High dimensional integration of smooth functions. *Numer. Math. 75* (1996), 79–97.

[65] Özbayat, S., and Janaswamy, R. A localized absorbing boundary condition for discretized parabolic equation. 2010 IEEE Symp. on Antennas and Propagat.

[66] Özbayat, S., and Janaswamy, R. Effective local absorbing boundary conditions for a finite difference implementation of the parabolic equation. *IEEE Trans. on Antennas and Propagat. 59*, 5 (May 2011), 1616–1625.

[67] Özbayat, S., and Janaswamy, R. Effectiveness of the sparse grid collocation methods for wave propagation problems. *under preparation for submission to IEEE Trans. Antennas and Propagat.* (2013).

[68] Özbayat, S., and Janaswamy, R. Quantification of high dimensional uncertainty in propagation over random terrain. IEEE Symp. on Antennas and Propagat. 2013.

[69] Patterson, T.N.L. The optimum addition of points to quadrature formulae. *Math. Comput. 22* (1968), 847–856.

[70] Rabitz, H., and Alış, Ö.F. General foundations of high-dimensional model representations. *J. Math. Chem. 25* (1999), 197–233.

[71] Rabitz, H., Alış, Ö.F., Shorter, J., and Shim, K. Efficient input-output model representations. *Computer Physics Communications 117* (1999), 11–20.

[72] Salzer, Herbert E. Lagrangian interpolation at the chebyshev points xn, $\nu \equiv$ cos ($\nu\pi$/n), $\nu = 0$ (1) n; some unnoted advantages. *The Computer Journal 15*, 2 (1972), 156–159.

[73] Sankaran, S., and Marsden, A.L. A stochastic collocation method for uncertainty quantification and propagation in cardiovascular simulations. *J. Biomech. Eng. 133*, 031001 (2011).

[74] Scarmozzino, R., Jr., Osgood, and M., Richard. Comparison of finite-difference and Fourier-transform solutions of the parabolic wave equation with emphasis on integrated-optics applications. *JOSA A 8*, 5 (1991), 724–731.

[75] Schürer, R. A comparison between (quasi-)Monte Carlo and cubature rule based methods for solving high-dimensional integration problems. *Mathematics and Computers in Simulation 62* (2003), 50–517.

[76] Senior, T.B.A., and Volakis, J.L. *Approximate Boundary Conditions in Electromagnetics*. IET, London, 1995.

[77] Slingsby, P. L. Modelling tropospheric ducting effects on VHF/UHF propagation. *Broadcasting, IEEE Transactions on 37*, 2 (1991), 25–34.

[78] Smith, G. D. *Numerical Solution of Partial Differential Equations: Finite Difference Methods*. Oxford University Press, 1985.

[79] Smolyak, S.A. Quadrature and interpolation formulas for tensor products of certain classes of functions. *Soviet Math. Dokl. 4* (1963), 240–243.

[80] Sobol, I.M. On the distribution of points in a cube and the approximate evaluation of integrals. *USSR Comput. Math. Math. Phys. 7* (1967), 86–112.

[81] Stein, M. Large sample properties of simulations using latin hypercube sampling. *Technometrics 29*, 2 (May 1987), 143–151.

[82] Sumant, P., Cangellaris, A., and Aluru, N. Reduced-order models of finite element approximations of electromagnetic devices exhibiting statistical variability. *IEEE Trans. Antennas Propagat. 60*, 1 (January 2012).

[83] Sumant, P.S., Wu, H., Cangellaris, A.C., and Aluru, N. A sparse grid based collocation method for model order reduction of finite element approximations of passive electromagnetic devices under uncertainty. IEEE Int. Microwave Symp. Digest, pp. 1652–1655, 2010.

[84] Thayer, Gordon D. An improved equation for the radio refractive index of air. *Radio Science 9*, 10 (1974), 803–807.

[85] Trefethen, L. N. *Is Gauss quadrature better than Clenshaw-Curtis?* Oxford Computing Laboratory, 2006.

[86] Tsuda, T, May, PT, Sato, T, Kato, S, and Fukao, S. Simultaneous observations of reflection echoes and refractive index gradient in the troposphere and lower stratosphere. *Radio science 23*, 4 (1988), 655–665.

[87] Tsuji, P., Xiu, D., and Ying, L. Fast method for high-frequency acoustic scattering from random scatterers. *International Journal for Uncertainty Quantification 1*, 2 (2011), 99–117.

[88] Valtr, P., Pechac, P., Kvicera, V., and Grabner, M. A terrestrial multiple-receiver radio link experiment at 10.7 GHz–comparisons of results with parabolic equation calculations. *Radioengineering 19*, 1 (2010), 117–121.

[89] Wagner, R.L., Song, J., and W.C., Chew. Monte Carlo simulation of electromagnetic scattering from two-dimensional random rough surfaces. *IEEE Trans. on Antennas and Propagat. 45*, 2 (February 1996), 235–245.

[90] Wasilkowski, G.W. Explicit cost bounds of algorithms for multivariate tensor product problems. *Journal of Complexity 11* (1995), 1–56.

[91] Webster, A. Raypath parameters in tropospheric multipath propagation. *Antennas and Propagation, IEEE Transactions on 30*, 4 (1982), 796–800.

[92] Wiener, N. The homogeneous chaos. *Amer. J. Math. 60* (1938), 897–936.

[93] Xiu, D. Fast numerical methods for stochastic computations: A review. *Commun. Comput. Phys. 5*, 2-4 (February 2009), 242–272.

[94] Xiu, D., and Hesthaven, J.S. High-order collocation methods for differential equations with random inputs. *SIAM J. Sci. Comput. 27*, 3 (2005), 1118–1139.

[95] Xiu, D., and Karniadakis, G.E. The Wiener-Askey polynomial chaos for stochastic differential equations. *SIAM J. Sci. Comput. 24*, 2 (2002), 619–644.

[96] Xu, J., and Janaswamy, R. Electromagnetic degrees of freedom in 2-d scattering environments. *IEEE Trans. on Antennas and Propagat. 54* (December 2006), 3882–3894.

[97] Yardim, C. *Statistical estimation and tracking of refractivity from radar clutter*. PhD thesis, University of California, San Diego, La Jolla, CA, 2007.

[98] Yardim, C., Gerstoft, P., and Hodgkiss, W. S. Estimation of radio refractivity from radar clutter using Bayesian Monte Carlo analysis. *Antennas and Propagation, IEEE Transactions on 54*, 4 (2006), 1318–1327.

[99] Yardim, C., Gerstoft, P., and Hodgkiss, W. S. Statistical maritime radar duct estimation using hybrid genetic algorithm–Markov chain Monte Carlo method. *Radio Science 42*, 3 (2007).

[100] Yucel, A. C., and Michielssen, E. Efficient GA-based electromagnetic optimization using HDMR-generated surrogate models. In *Antennas and Propagation Society International Symposium (APSURSI)* (2012), IEEE, pp. 1–2.

[101] Yücel, A.C., Bağcı, H., and Michielssen, E. Efficient stochastic EMC/EMI analysis using HDMR-generated surrogate models. URSI General Assembly, 2011.

[102] Zhurbenko, V., Ed. *Electromagnetic Waves*. InTech, Shanghai, 2011.